Title
Multi-functional Carbon Nanotube Assemblies with Dimension Controllable Gold Nanocrystals

Permalink
https://escholarship.org/uc/item/2dh276k9

Author
Xin, Wenbo

Publication Date
2016

Peer reviewed|Thesis/dissertation

UNIVERISTY OF CALIFORNIA

Los Angeles

Multi-functional Carbon Nanotube Assemblies with Dimension Controllable Gold Nanocrystals

A dissertation submitted in partial satisfaction of the
requirements for the degree Doctor of Philosophy
in Materials Science and Engineering

by

Wenbo Xin

2016

ABSTRACT OF THE DISSERTATION

Multi-functional Carbon Nanotube Assemblies with Dimension Controllable Gold Nanocrystals

by

Wenbo Xin

Doctor of Philosophy in Materials Science and Engineering

University of California, Los Angeles, 2016

Professor Jenn-Ming Yang, Chair

Carbon nanotube (CNT) and graphene as representative carbon allotropes have attracted considerable attention due to their exceptional properties in mechanical, electrical and thermal aspects. The assemblied CNT such as CNT yarns and sheets are particularly interesting regarding their promising applications in macro-scaled form. This work aims to develop multi-functional CNT assemblies coupling with gold nanocrystals with controllable dimensions. A novel strategy of growing two-dimensional gold nanoplates (2-D AuNPLs) on graphene template is first introduced, through which a comprehensive understanding of controllable growth of 2-D AuNPLs on carbon materials surface is established. Accordingly, large-scale AuNPLs can be homogeneously synthesized on CNT sheets substrate using a one-pot route. A detailed analysis of the crystalline structure of AuNPLs is carried out, which shows a preferential {111} orientation. It further presents hybrid CNT sheet-AuNPLs substrate can serve as a novel flexible surface-enhanced Raman scattering (SERS) substrate with ultrahigh sensitivity.

It is of particular interest to fill foreign materials into hollow cores of carbon nanotube (CNT) due to the feasibility of creating novel structures with innovative properties. Hence, this work introduces a new route to encapsulate one dimensional ultrathin gold nanowires (1-D AuNWs) inside CNTs from their assemblied forms. It utilizes oxygen plasma treatment to open CNT shells together with a wet chemistry method to fill gold atoms. The novelty originates from rapidly opening CNTs and efficiently diffusing gold atoms into the cavity. CNT shells function as protecting layers making ultrathin nanowires highly stable with electron irradiation. Thus, atomic structures of AuNWs are well resolved and systematically investigated under high resolution transmission electron microscope (HRTEM). It further illustrates twins can be created in ultrathin AuNWs with the bombardment of energetic electrons, which is effectively enhance their resistance to high-energy beam irradiation.

The dissertation of Wenbo Xin is approved.

Suneel Kodambaka

Xiangfeng Duan

Jenn-Ming Yang, Committee Chair

University of California, Los Angeles

2016

To my family, teachers and friends

TABLE OF CONTENTS

LIST OF FIGURES

ACKNOWLEDGEMENTS

I would like to deliver my sincere gratitude to my supervisor Professor Jenn-Ming Yang, who has offered me invaluable guidance in my Ph.D study. I also want to acknowledge my committee members Professor Suneel Kodambaka, Professor Dwight Streit and Professor Xiangfeng Duan, who have inspired me to construct scientific sense and motivated me to be an independent scientist. I also want to thank Professor Robert Hicks for his constructive suggestions on my research. My special thank goes to Larry Carlson, who has served as my research principle investigator and financially supported me throughout my Ph.D program.

I would also like to thank my former and current lab members and colleagues. I have benefited a lot from the collaboration with Dr. Igor de Rosa, Dr. Joseph V Severino, Dr. Hang Yu, Dr. Abbas Ebnonnasir, Dr. Yuan-Wei (Edward) Chang, Dian Yu, Peiyi Ye, Han Chueh Dr. Wei Yuan, Dr. PoChing Yeh, Dr. Jonathan Quan, Jose Gaviriaje, Tait McLouth. I would also like to thank Professor Jeng-Gong Duh and Ms. Su-Yueh Tsai from Taiwan, for their encouragement and continuous support over many years.

Finally, I wish to thank my family. My special thank goes to my wife, Yang Cao, who has been accompanying me throughout all the years of my Ph.D study. My parents, Huaizhu Xin and Qianhong Li, my brother Dianbo Xin and sister-in-law, Shuhui Zhang have been always supportive.

VITA

2004-2008	Bachelor of Science in Materials Science and Engineering, Shandong University, China
2008-2010	Masters of Science in Materials Science and Engineering Washington State University, USA
2010-2015	Graduate Student Researcher Department of Materials Science and Engineering, University of California, Los Angeles, USA
2011-2013	Teaching Assistant Master of Science in Engineering Online Program University of California, Los Angeles, USA

Chapter 1 Introduction to Carbon Nanotube, Carbon Nanotube Assemblies and Gold Nanocrystals

Abstract

Carbon nanotube (CNT) and graphene have attracted great attention due to their exceptional properties and potential applications in emerging fields. When decorated with gold nanocrystals, CNT and the assemblies present novel structures and multi-functional performance. This chapter reviews structures of CNT/graphene and CNT assemblies as well as dimension tunable Au nanocrystals. A few representative examples of CNT/graphene-Au nanocrystals are discussed. Meanwhile, current challenges in the development of multi-functional CNT assemblies with Au nanocrystals is presented. Finally, the motivations of the entire research are demonstrated.

1.1 Individual carbon nanotubes and carbon nanotube assemblies

Carbon, one of most abundant materials on earth, is a very promising material which meets the requirements for new materials nowadays, namely cost-effective, safe, environmentally friendly and so forth. As representative carbon allotropes, carbon nanotube (CNT) and graphene, since their discoveries in 1991 and 2004 respectively [1,2] have immediately raised hopes that they could initiate a technological revolution and boost the development of next-generation materials. Such hopes lead to CNT/graphene related commercial activity growing significantly during the past decade. In particular, worldwide CNT production capacity has enhanced at least 10-fold since 2006 [3] and the number of graphene-related patents has increased from less than 200 in 2006 to almost 4,000 in 2012.[4]

Structures of CNT and graphene have been well investigated. In general, CNTs are cylinders when single or multiple layers of graphene are seamlessly rolled up, denoted single-walled CNT (SWNT) and multi-walled CNT (MWNT) which are schematically shown in Fig. 1.1(a). Diameters of SWNT usually vary from 0.8 to 2 nm whereas MWNT typically shows a larger spectrum of diameters from 2 nm to more than 100 nm. Lengths of CNT can be tuned from sub-100 nm scale to centimeter scale, indicative of a high flexibility of aspect ratio (length over diameter). Fig. 1.1(b) illustrates a schematic diagram of a monolayer graphene, which is a typical two dimensional layered material (2DLM). Unlike CNT, graphene presents fixed thickness, that is atomically thin as well as tunable surface size from tens of nanometers to meter-scale.[5]

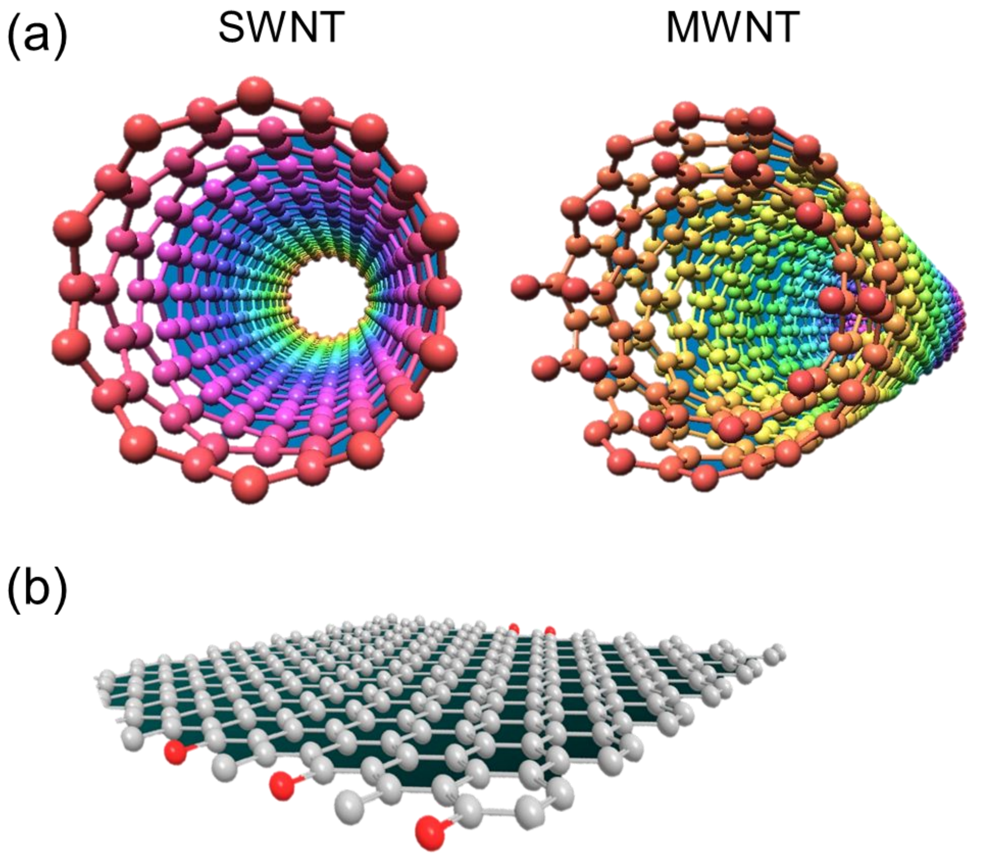

Figure 1.1 Schematic diagram of carbon nanotube (a) and graphene (b)

Owing to their remarkable properties, CNT and graphene have attracted enormously growing interest.The measured tensile fracture strength and elastic modulus of individual MWNT are up to 100 GPa and 1TPa, respectively[6]. This tensile strength is over one order of magnitude higher than any known industrial fiber. Moreover, the calculated electrical conductivity of SWNT at room temperature can be as high as 10^8 S/m,[7] which exceeds conventional conductive metals. On the other hand, it has been suggested graphene, as an alternative carbon material, could be even superior to CNT in terms of a variety of properties. For instance, theoretical simulations predict graphene has a thermal conductivity as high as 10, 000 W m K^{-1} better than that of CNT with a theoretical limit at 7, 000 W m K^{-1}.[9]

Thanks to the great advances in CNT growth recently, scaled-up fabrication of CNT assemblies with macro-form such as CNT yarns and sheets becomes practical. Generally, the production of CNT assemblies can be classified as wet and dry spinning. A representative example of wet spinning process is the strategy first proposed by Ericson et al. in which CNT fibers were spun from a superacid liquid crystalline phase.[10] Post annealing process is usually required to remove the residual impurities from as made CNT assemblies. On the other hand, dry spinning is a process in which CNT assemblies are drawn directly from chemical vapor deposition (CVD) reactor. For example, products from Nanocomp Technologies Inc. (Merrimack, NH) are typically fabricated with dry spinning process. In particular, CNT grown with

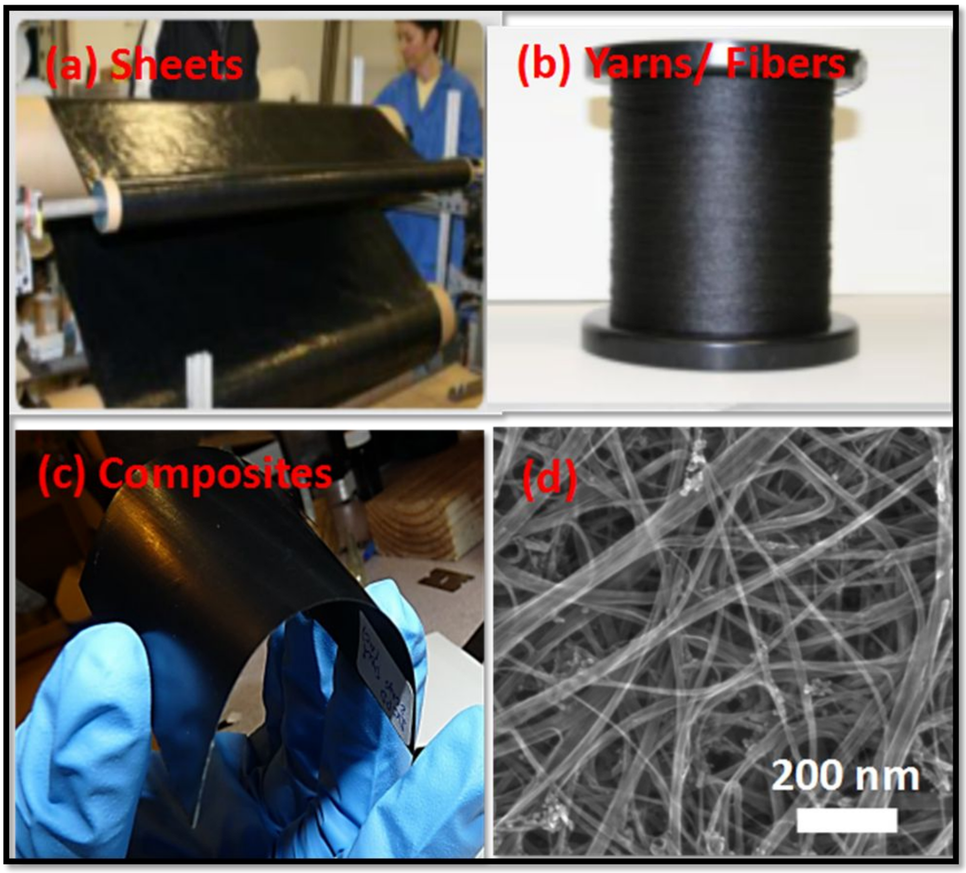

Figure 1.2 Representative Nanocomp products from dry spinning process. (a) CNT sheets (b) CNT yarns (c) Composites made from post treatment of CNT sheets and (d) microstructure of CNT sheets. (Images (a) and (b) adapted from Nanocomp website.[11])

iron catalysts in a CVD furnace is gradually drawn out and subsequently collected onto a drum with a rotating velocity of ~15m/min to impart alignment in the drawing direction. Shown in Fig. 1.2 are the pictures of as made CNT sheets and yarns from Nanocomp Technologies Inc.[11] Detailed reviews on the synthesis of CNT assemblies can be obtained from other reports.[7,12]

Despite individual CNT shows exceptional properties as discussed above, currently realized mechanical and electrical properties of CNT assemblies remain much lower than those of individual CNTs. For example, as made SWNT fiber showed a tensile strength approximately 160 MPa,[13] far lower than that of individual CNT. Hence, great efforts have been made in order to improve mechanical and electrical properties of CNT assemblies by means of synthesis and post treatment. Subsequently, significant enhancement regarding the strength has been achieved. Maximum strength of macrostructural CNT films to date reaches to 10.8 GPa which is well above those for any known industrial fibers and films.[14] On other hand, however, the improvement of electrical conductivity of CNT assemblies is rather limited in the past few years. The highest electrical conductivity of CNT fibers with a diameter of 5 μm has been reported to be approximately 6.7×10^6 S/m, which are fabricated with purified double walled CNT (DWNT) doped with iodine.[15] Due to a much lower density, their specific electrical conductivity (conductivity/weight) is higher than copper and aluminum, however, the resistivity is still one order of magnitude higher than that of copper and individual CNT. Fig. 1.3 summaries the road-map of efforts made on improving conductivity of as made CNT assemblies

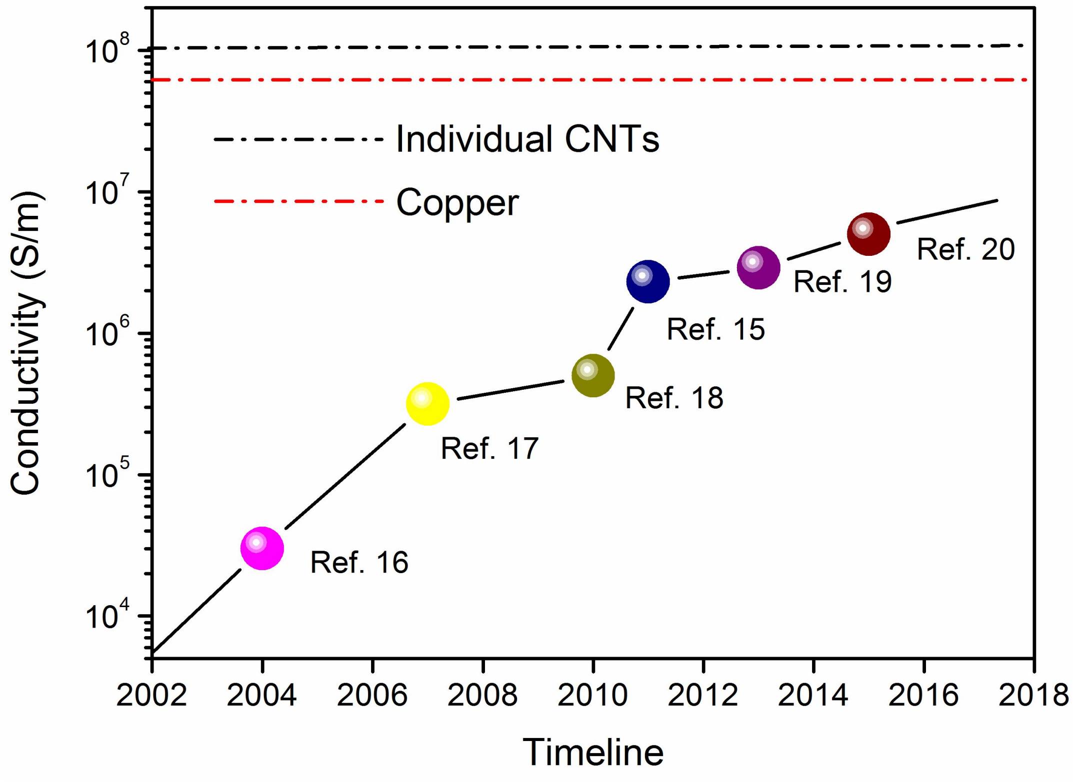

Figure 1.3 Road map of the enhancement of electrical conductivity of as made CNT assemblies[15-20]

along with time. Although the conductivity has been enhanced from less than 10^4 S/m to close to 10^7 S/m, there still exists a large gap between the CNT assemblies and copper which, therefore, requires further efforts to make them competitive with copper.

1.2 Gold nanocrystals

It is well established that metals indispensably associates with CNT/graphene almost everywhere from initial growth to final application. For example, a number of metal nanoparticles (Ni, Fe, Co and even Au)[21] could catalyze the growth of CNT under desirable conditions. Moreover, the measurement of electron transport in CNT typically requires CNT directly contact with metal probes at certain points.[8] In particular, when CNT is employed as the ultrathin channel of field-effect transistor (FET), metal-CNT contacts significantly determine the performance of CNT-FET.[22] It is therefore, of fundamental importance to investigate the interface and understand the interaction of CNT/graphene and metals in order to link such hybrids to environment and prosper the development of novel nanotechnologies.

Among a variety of metal crystals, it is noteworthy to study gold nanocrystals integrated with carbon nanomaterials. In contrast to CNT/graphene which have been discovered no more than three decades, gold posses a long history among the first “old” materials that being used by mankind. Due to its highly stable nature against chemical oxidization, bulk gold has been broadly used in precious jewelry and coinage for thousands of years. The significant advances in nanoscience and nanotechnologies since last century have identified gold nanocrystals play even more precious roles in the emerging applications in human life. Owing to its highly biocompatible and nontoxic characteristics, it is not surprising to notice that a new "Golden Age" relying on gold nanocrystals-enabled technologies has truly come to human life.[23,24]

Unlike the unvivid CNT/graphene, gold nanocrystals exhibit a much more colorful world where their colors largely depend on the size, shapes and dimensions. It has been well known that colors of metal nanoparticles originate from the collective oscillation of the electrons in conduction band, namely the surface plasmon oscillation.[25] The dimension/size/shapes of gold nanocrystals determine their surface plasmon resonance (SPR) absorption and hence dimension and shape controllable synthesis of gold nanocrystals is highly desirable for emerging applications. As a matter of fact, a large number of publications have reported the comprehensive strategies to fabricate free-standing gold nanocrystals with controllable shapes and dimensions including colloid gold nanorods,[26] platelike gold nanosheets,[27] well-defined gold bipyramid,[28] ultrathin gold nanowires,[29] gold nanoribbons[30] and so forth. A few representative gold nanocrystals with various dimensions and shapes are listed in Fig. 1.4 (note the images were colored artificially which would not represent the real colors of gold nanocrystals).

It is particularly interesting to mention Au nanoplates and ultrathin Au nanowires among a wide range of gold nanocrystals because they show anisotropic structures and unique properties. In contrast to Au nanoparticles and nanorods whose SPR absorption usually locate at visible wavelength region, Au nanoplates could present

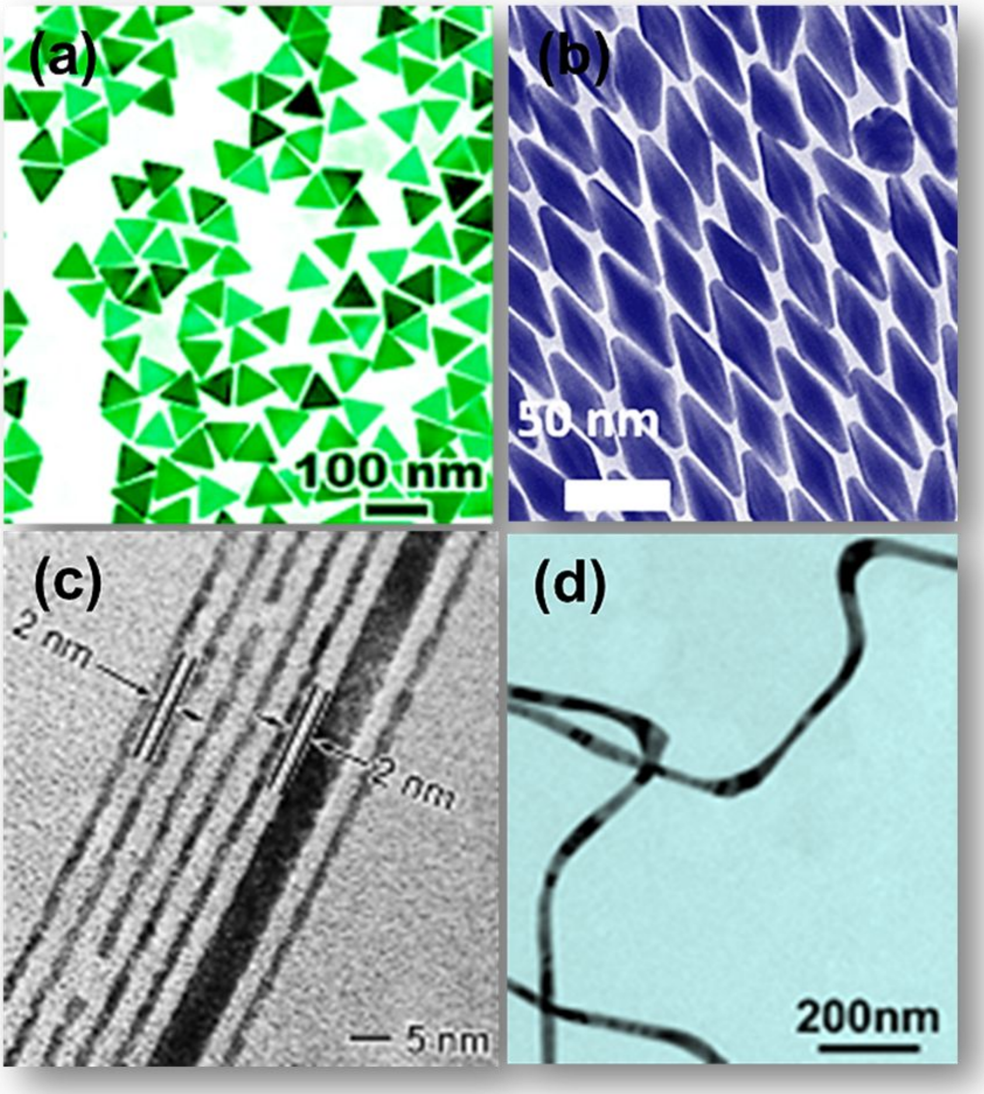

Figure 1.4 Representative gold nanocrystals with various dimensions and shapes (Images adapted from references 27-30)

strong SPR peaks at near-infrared (NIR) region. This region is of fundamental importance in biological fields since the energy from NIR is significantly lower than those from visible and ultraviolet regions, which are potentially detrimental to biological tissues and cells.[31] Moreover, the monodispered Au nanoplates with triangular shapes exhibit promising performance as surface-enhanced Raman scattering (SERS) substrates which are capable of recognizing various analytes at the concentrations as low as 10^{-8} M.[32] On the other hand, ultrathin Au nanowires (AuNWs) display extremely high aspect ratio (length/diameter) which could be larger than 10,000[33] and their electron transport behavior relies on the diameters. Unlike bulk gold, ultrathin AuNWs display distinct properties in many aspects. For instance, AuNWs with diameters from 3 nm to 10 nm could be perfectly welded in a relative cold environment by means of mechanical contact.[34] In addition, the tensile strength of ultrathin AuNWs with ultrahigh twin density (UTD) is measured to be 3.12 GPa almost reaching the ultimate strength limit.[35] Strong, conductive and flexible characteristics lead to ultrathin AuNWs very useful in modern nanotechnologies such as being used as a wearable and highly flexible pressure sensor.[33]

1.3 CNT/graphene-Au nanocrystal hybrids

When integrating dimension controllable Au nanocrystals with CNT/graphene, not only reinforced properties but also novel nanostructures with attractive performance could be created. It has been reported that electrical conductivity of CNT fibers can be effectively enhanced with gold doping. For instance, conductivity increased from 59, 520 S/m to 115, 270 S/m with sparsely doped gold nanoparticles in

CNT fibers.[36] In addition, MWNT coupling with ultrathin Au nanowires can function as a sensor which is highly efficient and selective to probe alpha-fetoprotein (AFP) antigen, an important biomarker of a typical liver cancer.[37] Meanwhile, the hybrid of graphene and Au nanocrystals has brought in a wide range of novel nanocomposites as well as innovative functions. For instance, triangular Au nanoplates decorated graphene showed high catalytic efficiency for the reduction of 4-nitrophenol by $NaBH_4$.[38] More interestingly, hexagonal close-packed (HCP) Au nanosheets have been synthesized on graphene oxide which is unusual regarding the conventional face-centered cubic (FCC) structure of gold.[39]

Despite incorporation of Au nanocrystals into CNT/graphene scaffolds has given rise to a number of interesting hybrid structures and desired applications, a series of challenges and obstacles still remain. Conventional synthesis of two dimensional Au nanoplates anchoring on graphene normally requires the addition of surfactants and the obtained Au nanoplates own limited size.[38] Moreover, although a highly sensitive surface-enhanced Raman scattering (SERS) substrate can be fabricated with uniformly impregnating Au nanoparticles into CNT film, an extremely dense Au nanoparticles have to be loaded on CNT film to maintain the sensitivity which can lead to certain issues with regard to the cost.[40] In addition, it is widely reported that ultrathin AuNWs are so fragile to electron irradiation that their structures degrade rapidly under transmission electron mircoscope (TEM), which result in difficulties in the detailed investigation of their crystalline structures.[29] Hence, it is expected that ultrathin AuNWs can be protected with graphitic shells from bombardment of electrons when AuNWs are encapsulated inside CNT (AuNWs@CNT). Such protection could make ultrathin AuNWs more resistant to electron attack. However, surprisingly rare work has been reported to grow ultrathin AuNWs inside CNT especially those with high aspect ratio. Moreover, the conventional way to fill metal nanowires in CNT is rather complicated and time-consuming.[41] Last but not least, in spite of enhanced electrical conductivity of CNT assemblies with gold doping, the enhancement gradually reaches to a plateau along with treatment time[42] which greatly restricts the development of highly conductive CNT assemblies in virtue of gold doping.

In order to overcome the aforementioned obstacles, this work introduces novel synthesis methods of dimension controllable Au nanocrystals on graphene and CNT assemblies. Meanwhile, this work presents multi-functional performance of CNT assemblies with various Au nanocrystals (i.e. well-defined Au nanoplates and ultrathin AuNWs) including flexible SERS substrate, protection layers of ultrathin AuNWs and highly conductive and strong CNT fibers.

This dissertation contains six chapters. In Chapter 1, an introduction of CNT assemblies associating with a number of Au nanocrytals is presented. The motivation of this work is discussed. As of Chapter 2, it demonstrates a novel method for synthesizing well-defined Au nanoplates with tunable size on multi-layer graphene. A comprehensive investigation on structures and morphologies of graphene-Au nanoplates is provided. It also suggests a growth mechanism demonstrating that Br^- plays a critical role. Accordingly, CNT sheets with uniformly synthesized Au nanoplates can be used as a novel flexible SERS substrate, which is presented in Chapter 3. CNT sheets-Au nanoplates serving as SERS substrate shows higher sensitivity to probe low concentration analyte compared to the substrate made from CNT sheets-Au nanoparticles.

Chapter 4 describes a novel synthesis method to grow ultrathin AuNWs inside individual CNT from CNT yarns. With oxygen plasma treatment, CNT structures are efficiently opened in a superior short time, i.e. 40 s. Gold nanowires grow inside CNT at a moderately low temperature (~80-90 ^{o}C). A detailed study of ultrathin AuNWs structures with high resolution TEM is presented. It evidently shows that ultrathin AuNWs with multiple twins are more resistant to electron irradiation compared to the wires free of twins, which opens up a new route to investigate ultrathin wires. Finally, Chapter 6 concludes the remarks accomplished in this work and a series of future work are proposed based on the present findings.

1.4 References

1. S. Iijima, *Nature*, 1991, **354**, 56-58

2. K. S. Novoselov, A. K. Geim, S. Morozov, D. Jiang, Y. Zhang, S. Dubonos, I. Grigorieva and A. Firsov, *Science*, 2004, **306**, 666 – 669

3. M. F. L. De Volder, S. H. Tawfick, R. H. Baughman and A. J. Hart, *Science*, 2013, **339**, 535–539

4. A. C. Ferrari, F. Bonaccorso, V. Fal'ko, K. S. Novoselov, S. Roche, P. Boggild, S. Borini, F. H. L. Koppens, V. Palermo, N. Pugno, J. A. Garrido, R. Sordan, A. Bianco, L. Ballerini, M. Prato, E. Lidorikis, J. Kivioja, C. Marinelli, T. Ryhanen, A. Morpurgo, J. N. Coleman, V. Nicolosi, L. Colombo, A. Fert, M. Garcia-Hernandez, A. Bachtold, G. F. Schneider, F. Guinea, C. Dekker, M. Barbone, Z. Sun, C. Galiotis, A. N. Grigorenko, G. Konstantatos, A. Kis, M. Katsnelson, L. Vandersypen, A. Loiseau, V. Morandi, D. Neumaier, E. Treossi, V. Pellegrini, M. Polini, A. Tredicucci, G. M. Williams, B. Hee Hong, J.-H. Ahn, J. Min Kim, H. Zirath, B. J. van Wees, H. van der Zant, L. Occhipinti, A. Di Matteo, I. A. Kinloch, T. Seyller, E. Quesnel, X. Feng, K. Teo, N. Rupesinghe, P. Hakonen, S. R. T. Neil, Q. Tannock, T. Lofwander and J. Kinaret, *Nanoscale*, 2015, **7**, 4598–4810

5. S. Bae, H. Kim, Y. Lee, X. Xu, J. S. Park, Y. Zheng, J. Balakrishnan, T. Lei, H. Ri Kim, Y. I. Song, Y. J. Kim, K. S. Kim, B. Özyilmaz, J. H. Ahn, B. H. Hong and S. Iijima, *Nat. Nanotechnol.*, 2010, **5**, 574–578

6. B. Peng, M. Locascio, P. Zapol, S. Y. Li, S. L. Mielke, G. C. Schatz and H. D. Espinosa, *Nat. Nanotechnol.*, 2008, **3**, 626–631

7. A. Lekawa-Raus, J. Patmore, L. Kurzepa, J. Bulmer and K. Koziol, *Adv. Funct. Mater.*, 2014, **24**, 3661–3682

8. M. S. Purewal, B. H. Hong, A. Ravi, B. Chandra, J. Hone and P. Kim, *Phys. Rev. Lett.*, 2007, **98**, 186808

9. A. A. Balandin, *Nat. Mater.*, 2011, **10**, 569–581

10. L. M. Ericson, H. Fan, H. Q. Peng, V. A. Davis, W. Zhou, J. Sulpizio, Y. H. Wang, R. Booker, J. Vavro, C. Guthy, A. N. G. Parra-Vasquez, M. J. Kim, S. Ramesh, R. K. Saini, C. Kittrell, G. Lavin, H. Schmidt, W. W. Adams, W. E. Billups, M. Pasquali, W. F. Hwang, R. H. Hauge, J. E. Fischer and R. E. Smalley, *Science*, 2004, **305**, 1447–1450

11. Pictures of CNT sheets and yarns were obtained from Nanocomp website: http://www.nanocomptech.com/formats

12. Z. Li, Z. Liu, H. Sun and C. Gao, *Chem. Rev.*, 2015, **115**, 7046

13. B. Vigolo, A. Penicaud, C. Coulon, C. Sauder, R. Pailler, C. Journet, P. Bernier and P. Poulin, *Science*, 2000, **290**, 1331

14. W. Xu, Y. Chen, H. Zhan and J. N. Wang, *Nano Lett.*, 2016, **16**, 946-952

15. Y. Zhao, J. Q. Wei, R. Vajtai, P. Ajayan and E. Barrera, *Sci. Rep.*, 2011, **1**, 83

16. M. Zhang, K. R. Atkinson and R. H. Baughman, *Science*, 2004, **306**, 1358–1361

17. K. Koziol, J. Vilatela, A. Moisala, M. Motta, P. Cunniff, M. Sennett and A. Windle, *Science*, 2007, **318**, 1892–1895

18. X.-H. Zhong, Y.-L. Li, Y.-K. Liu, X.-H. Qiao, Y. Feng, J. Liang, J. Jin, L. Zhu, F. Hou and J.-Y. Li, *Adv. Mater.*, 2010, **22**, 692–696

19. N. Behabtu, C. C. Young, D. E. Tsentalovich, O. Kleinerman, X. Wang, A. W. Ma, E. A. Bengio, R. T. Waarbeek, J. J. Jong, R. E. Hoogerwerf, S. B. Fairchild, J. B. Ferguson, B. Maruyama, J. Kono, Y. Talmon, Y. Cohen, M. J. Otto and M. Pasquali, *Science*, 2013, **339**, 182-186

20. A. R. Bucossi, C. D. Cress, C. M. Schauerman, J. E. Rossi, I. Puchades and B. J. Landi, *ACS Appl. Mater. Interfaces*, 2015, **7**, 27299–27305

21. S. Bhaviripudi, E. Mile, S. A. Steiner, A. T. Zare, M. S. Dresselhaus, A. M. Belcher and J. Kong, *J. Am. Chem. Soc.*, 2007, **129**, 1516–1517

22. A. D. Franklin, M. Luisier, S.-J. Han, G. Tulevski, C. M. Breslin, L. Gignac, M. S. Lundstrom and W. Haensch, *Nano Lett.*, 2012, **12**, 758–762

23. E. C. Dreaden, A. M. Alkilany, X. Huang, C. J. Murphy and M. A. El-Sayed, *Chem. Soc. Rev.*, 2012, **41**, 2740-2779

24. X. Yang, M. Yang, B. Pang, M. Vara and Y. Xia, *Chem. Rev.*, 2015, **115**, 10410-10488

25. M. Grzelczak, J. Pérez-Juste, P. Mulvaney and L. M. Liz-Marzán, *Chem. Soc. Rev.*, 2008, **37**, 1783–1791

26. N. R. Jana, L. Gearheart and C. J. Murphy, *J. Phys. Chem. B*, 2001, **105**, 4065-4067

27. L. Chen, F. Ji, Y. Xu, L. He, Y. Mi, F. Bao, B. Sun, X. Zhang and Q. Zhang, *Nano Lett.*, 2014, **14**, 7201–7206

28. Q. Shi, K. J. Si, D. Sikdar, L. W. Yap, M. Premaratne and W. Cheng, *ACS Nano,* 2016, **10**, 967-976

29. X. Lu, M. S. Yavuz, H.-Y. Tuan, B. A. Korgel and Y. Xia, *J. Am. Chem. Soc.*, 2008, **130**, 8900–8901

30. Y. Xu, X. Wang, L. Chen, Y. Zhao, L. He, P. Yang, H. Wu, F. Bao and Q. Zhang, *J. Mater. Chem. C*, 2015, **3**, 1447–1451

31. Y. Huang, A. R. Ferhan, Y. Gao, A. Dandapat and D.-H. Kim, *Nanoscale*, 2014, **6**, 6496–6500

32. L. Scarabelli, M. C. Puchau, J. J. Giner-Casares, J. Langer and L. M. Liz-Marzan, *ACS Nano*, 2014, **8**, 5833-5842

33. S. Gong, W. Schwalb, Y. Wang, Y. Chen, Y. Tang, J. Si, B. Shirinzadeh and W. Cheng, *Nat. Commun.*, 2014, **5**, 3132

34. Y. Lu, J. Y. Huang, C. Wang, S. Sun and J. Lou, *Nat. Nanotechnol.*, 2010, **5**, 218–224

35. J. W. Wang, F. Sansoz, J. Y. Huang, Y. Liu, S. H. Sun, Z. Zhang and S. X. Mao, *Nat. Commun.*, 2013, **4**, 1742

36. Q. W. Li, Y. Li, X. F. Zhang, S. B. Chikkannanavar, Y. H. Zhao, A. M. Dangelewicz, L. X. Zheng, S. K. Doorn, Q. X. Jia, D. E. Peterson, P. N. Arendt and Y. T. Zhu, *Adv. Mater.*, 2007, **19**, 3358–3363

37. H. Cui, C. Hong, A. Ying, X. Yang and S. Ren, *ACS Nano*, 2013, **7**, 7805–7811

38. W. Wang, J. Gu, W. Hua, X. Jia and K. Xi, *Chem. Commun.*, 2014, **50**, 8889-8891

39. X. Huang, S. Z. Li, Y. Z. Huang, S. X. Wu, X. Z. Zhou, S. Z. Li, C. L. Gan, F. Boey, C. A. Mirkin and H. Zhang, *Nat. Commun.*, 2011, **2**, 292

40. K. Zhang, J. Ji, X. Fang, L. Yan and B. Liu, *Analyst*, 2015, **140**, 134–139

41. A. Govindaraj, B. C. Satishkumar, M. Nath and C. N. R. Rao, *Chem. Mater.*, 2000, **12**, 202

42. P. Jarosz, C. Schauerman, J. Alvarenga, B. Moses, T. Mastrangelo, R. Raffaelle, R. Ridgley and B. Landi, Nanoscale, 2011, 3, 4542-4553

Chapter 2 One-step Synthesis of Gold Nanoplates with Tunable Size and Thickness on Multi-layer Graphene Sheets

Abstract

Graphene decorated with Au nanocrystals with controllable dimension, size and geometry is highly desirable as a novel nanocomposite for emerging applications in nanotechnology. Here, we demonstrate one-step, surfactant-free, synthesis method for two dimensional Au nanoplates (AuNPLs) on multi-layer graphene sheets. We have revealed, for the first time, $KAuBr_4$ serving as the gold precursor plays a key role in growing AuNPLs on graphene sheets. Characterization shows that the synthesized AuNPLs with well-defined shapes are single-crystalline FCC structure with highly preferential {111} orientation. The geometry and size of AuNPLs are tunable by varying treatment time and accordingly we propose a three-step growth mechanism, showing liberated Br^- ions from gold precursor function as capping agent as well as etchant during the process. The recorded Raman signals of graphene-AuNPLs hybrid are enhanced due to charge-transfer complex (chemical mechanism) where the enhancement factor depends on the geometry and size of AuNPLs.

2.1 Introduction

Over the past decade, graphene has attracted intensive attention due to its exceptional intrinsic properties including high optical transparency,[1] excellent mechanical properties[2] and superior thermal conductivity.[3] Owing to its two-dimensional structure, large specific surface area (~2630 m^2/g)[4] and chemical stability, graphene is an ideal platform for building nanostructured composites with metal nanocrystals. Processes for integrating graphene and graphene oxide with metal nanocrystals have been widely reported such as Ag,[5] Pd,[6] Pt,[7] Ni,[8, 9] Ti,[9] and Au.[9-15] Of particular interest is nanostructured Au with controllable size and shapes decorating on graphene substrate, which has demonstrated application as ultra-fast photodectors,[10-11] highly efficient catalysts,[12] and Raman signal enhancers.[13-16] For instance, coupling ultrafine Au nanoparticles with atomically thin graphene lead to a significant enhancement of photocurrent and external quantum efficiency by up to 1500%.[10] In addition, Au nanorods decorated graphene surface showed a dramatic Raman signals increase at the rods tip by 34-fold.[14]

Great efforts have been made to integrate Au nanocrystals on graphene sheets with controllable structures and dimensions, since the geometry and size of Au nanocrystals determine the performance of such graphene-based nanocomposites. In particular, various nanostructures including nanoparticles,[9] nanoflowers,[13] nanorods,[14, 15] nanostars,[17] and nanobipyramids[18] were deposited on graphene or graphene oxide support. However, there is relatively little attention paid to the controllable growth of two dimensional (2-D) Au nanocystals. In contrast to nanoparticles and nanorods whose surface plasmon resonances (SPR) wavelengths normally locate at the visible wavelength region, Au nanoplates (AuNPLs) display SPR peaks at near-infrared region due to their unique 2-D structural characteristic.[19] It has been also reported that AuNPLs showed high sensitivity in surface-enhanced Raman scattering (SERS) [20] and strong enhancement of electric fields.[21] Despite researchers attempt to decorate 2-D AuNPLs on graphene sheets, various challenges still remain. For example, Huang and co-workers synthesized square nanosheets with hexagonal close-packed (hcp) crystallinity on graphene oxide surfaces, but they expressed both dimensional and structural transformation with electron irradiation.[22] Wang and co-workers developed a facile and environment-friendly method to deposit the AuNPLs on graphene sheets, however, the size of AuNPLs was limited to sub-10 nanometers.[12] Even though researchers were capable of growing 2-D AuNPLs on reduced graphene oxide surfaces via a template-free strategy, the obtained AuNPLs owned irregular shapes with low concentration.[23] Therefore, thoroughly understanding how to synthesize high-yield and well-defined AuNPLs with tunable size on graphene support is crucial in order to integrate such novel nanostructures into various technologies.

Previous research has shown that bromide (Br^-) plays a key role in inducing anisotropic growth of Au nanocrystals.[24-27] Although the mechanism involved in the formation of anisotropic Au nanocrystals is elusive, it is widespreadly speculated that Br^- serves as shape-directing agent which selectively binds to specific faces of Au clusters. This stabilizes certain surfaces and facilitates the formation of anisotropic structures like nanorods and nanoplates.[27] Furthermore, it has been shown that

$[AuBr_2]^-$ retards the reaction of Au^{3+} to Au^0 by the reduction agent compared to $[AuCl_2]^-$. [27] This favors the anisotropic growth of gold nanocrystals controlled by a kinetic process[25,28]. Therefore, potassium tetrabromoaurate ($KAuBr_4$) is hypothesized to be an ideal gold precursor for surfactant-free synthesis of anisotropic gold nanocrystals. Indeed, there is one report showing that longer dendritic gold nanorods were synthesized by using $KAuBr_4$ rather than the more common $HAuCl_4$ precursor.[29]

Herein, we demonstrate a novel one-step, high-yield and surfactant-free synthesis of well-defined AuNPLs via thermal reduction of $KAuBr_4$ on multi-layer graphene sheets. To our best knowledge, this is the first report that obtains large-scale production of size-tunable AuNPLs on graphene sheets by employing $KAuBr_4$ as the gold precursor. Our characterizations demonstrate that AuNPLs are single-crystalline with face-centered cubic (FCC) structure. We are also capable of controlling the size and thickness of AuNPLs simply with the adjustment of treatment time. In general, the edge length of synthesized AuNPLs are from a few micrometers to hundred nanometers, depending on thermal reduction time. In the end, we also present the correlation of the Raman scattering enhancement of graphene sheets with various AuNPLs sizes and geometries.

2.2 Experimental

2.2.1 Chemicals and Materials

Potassium tetrabromoaurate hydrate ($KAuBr_4 \cdot xH_2O$, 99.9%) and gold chloride hydrate ($HAuCl_4 \cdot xH_2O$, 99.999%) were purchased from Sigma-Aldrich, USA. Multi-layer Graphene sheets (AO-2) were purchased from Graphene Supermarket

(Calverton, New York). Average thickness of the AO-2 is 13 nm with 52 layers (values obtained from manufacturer).[30] This multi-layer graphene was selected for this work for two reasons. First, it is commercially available graphene product, which is readily accessible for large-scale reproducible synthesis of graphene based nanocomposites. Second, it has rather pure surfaces with low-concentration defects, which was confirmed by Raman spectroscopy in the supplementary information Fig. S 2.1. I_D/I_G is around 0.24, indicating pure surfaces with relatively low-concentration defects. Detailed analysis will be discussed in Results and Discussion session.

2.2.2 Preparation of Graphene Nanosheets (AO-2) Suspension

30 mg AO-2 graphene powder was dispersed in 20 ml deionized water. In order to obtain homogenous dispersion of graphene powder in water, probe ultrasonication of the suspension was employed. The ultrasonication procedure was performed on vibra-cell VCX-130 with VC-50 mircotip (Sonics & Materials, Inc.) at 25% amplification for 5 minutes with the frequency of 1 second on and 2 seconds off. The obtained AO-2 sheets were analyzed with scanning electron microscopy (SEM) and the image was shown in Fig. S 2.2.

2.2.3 Synthesis of GS-AuNPLs with $KAuBr_4$

0.25 ml as-prepared AO-2 suspension (1.5 mg/ml) was injected in 4 ml deionized water. 240 mg 1 mM $KAuBr_4$ solution was added into the above solution with gently shaking. Then, the mixture was stored in a capped glass vial and kept at 80 °C for thermal reduction for various hours. The final product was collected by centrifuge and washed with water for further analysis.

2.2.4 Synthesis of GS-Au nanostructures with $HAuCl_4$

For comparison, Au nanocrystals were synthesized on AO-2 substrate using $HAuCl_4$ as the gold precursor. All the reaction conditions were unchanged except for replacing $KAuBr_4$ with $HAuCl_4$. That is, 0.25 ml as-prepared AO-2 suspension (1.5mg/ml) was injected in 4ml DI water. 240mg 1mM $HAuCl_4$ solution was then added to the above solution. Then, the mixture was stored in a capped glass vial and maintained at 80 °C.

2.2.5 Characterizations

Electron microscopy studies and X-ray diffraction (XRD) analysis were carried out in order to understand the structures and morphologies of AuNPLs-GS hybrid. To prepare SEM samples, the obtained mixture was deposited on a clean silicon substrate with a pipette and dried at 80 °C for 2 hours. Scanning electron microscopy coupled with energy dispersive X-ray (SEM/EDX) analysis was obtained with an FEI Nova NanoSEM 230. Transmission electron microscopy (TEM) images were captured with an FEI T12 Quick CryoEM with the accelerating voltage at 120 keV. High resolution TEM (HRTEM) images were obtained with an FEI Titan S/TEM system with the accelerating voltage at 80 keV. The X-ray diffraction (XRD) analysis was performed on a Bede D1 diffractometer using Cu $K\alpha 1$ radiation from a laboratory tube source. The thickness of AuNPLs was characterized with atomic force microscopy (AFM) in Bruker Dimension Icon Scanning Probe Microscope systems. Raman spectral analysis was obtained with a Renishaw In-Via Raman system with the laser length of 785nm.

2.3 Result and Discussion

The synthesis procedures of AuNPLs-GS nanocomposite are schematically shown in Scheme 2.1. A certain amount of multi-layer graphene sheets (AO-2) after ultrasonication with water was soaked with $KAuB_4$ aqueous solution and the obtained mixture was hydrothermally maintained at 80°C for different hours to tune the size and thickness of AuNPLs. This process is an electroless metal deposition due to the spontaneous redox reaction between carbon and gold precursor[31], which is a simple and surfactant-free procedure without additives. After centrifuge, the obtained hybrid was collected and transferred to specific substrates for further characterizations. Figure 2.1 shows representative SEM images of AuNPLs synthesized on GS substrate at 5 hours. High-yield AuNPLs with well-defined geometry, mainly hexagonal and triangular shapes were synthesized on graphene sheets shown in Fig. 2.1(a) where the concentration of Au nanoparticles was low. AuNPLs synthesized at 5 hours presented micrometers-scale edge length. A higher magnification image in Fig. 2.1(b) showed a few AuNPLs aggregated on GS surfaces. It is interesting to note those AuNPLs showed highly transparent characteristic because of their ultrathin thickness, which was consistent with the previous report of transparency of ultrathin Au sheets.[32] We found those AuNPLs formed either isolated single-layer plate in Fig. 2.1(c) or aggregated to multi-layer plates in Fig. 2.1(d) on top of graphene sheets. Of particular interest is a single-layer AuNPL found in Fig. 2.1(c) displaying wrinkled surface where the arrow is pointing. This was probably due to the bending from graphene edges because it was so thin that it could be easily deformed by the rough edges from graphene. More details of thickness characterization will be discussed in the following paragraphs.

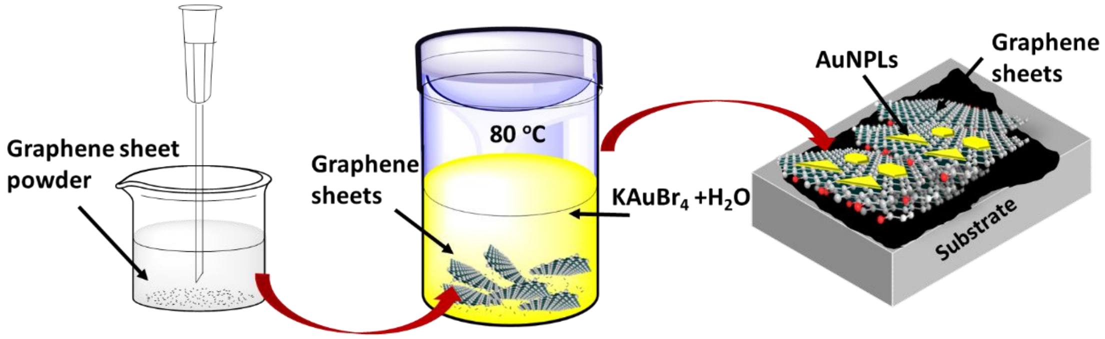

Scheme 2.1 Schematic illustration of synthesis of AuNPLs on graphene sheets

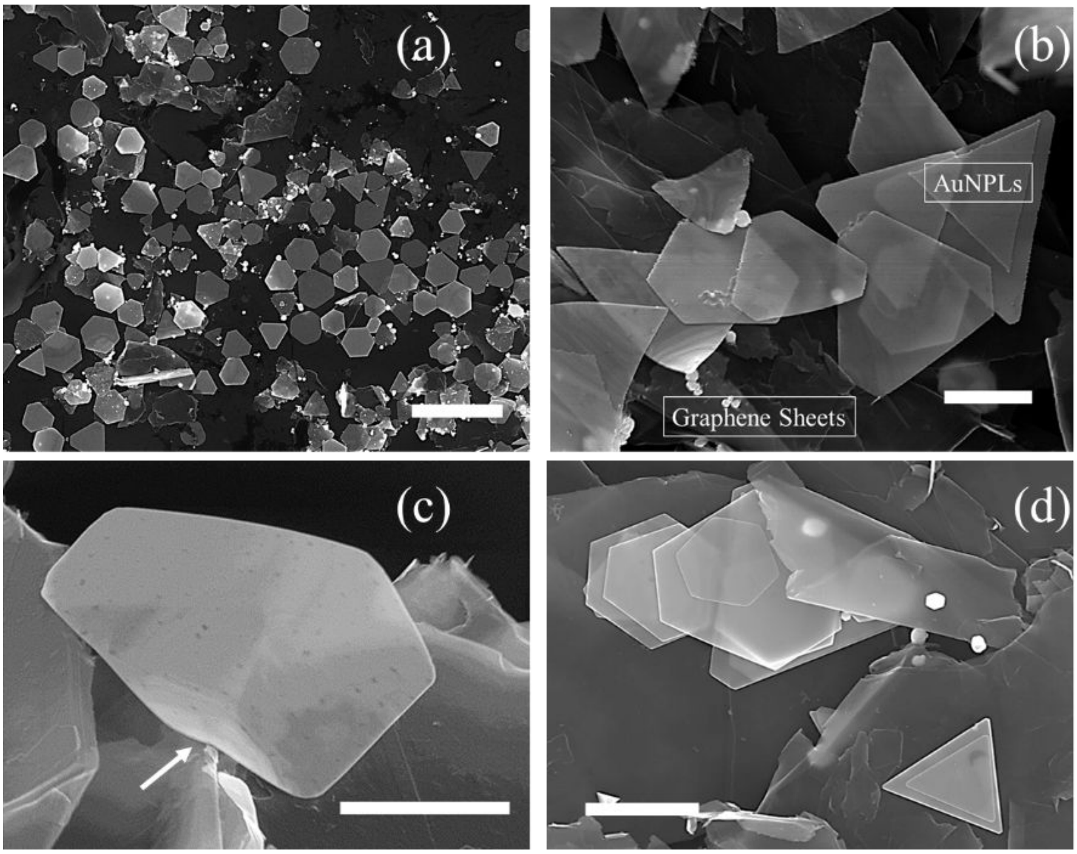

Figure 2.1 SEM images of (a) high-yield AuNPLs synthesized on graphene sheets (GS) (b) representative image of ultra-thin AuNPLs lying on graphene substrate (c) an isolated hexagonal AuNPLs wrinkled by graphene sheet edge (arrow pointed) and (d) AuNPLs aggregation on GS. Scale bar in (a) 5 μm and in (b), (c) and (d) 1 μm.

In order to determine the compositional information of synthesized AuNPLs, we carried out elemental analysis with energy dispersive X-ray spectroscopy (EDX). Figure 2.2 shows the elemental mapping of AuNPLs-GS hybrid. The gold element homogenously distributed in the triangular area corresponding to the AuNPL's shape indicative of a smooth and flat Au sheet lying on the substrate. From the comparison of spot 1 with spots 2 and 3 (Fig. 2.2(a)), there is a sharp increase of the Au peak intensity with a suppression of C peak. This confirms the uniformity of the AuNPL. According to the spots shooting, a weak intensity of bromine was detected at all three spots. It is reported that Br^- ions from $[AuBr_4]^-$ were able to get liberated from thermal reduction $[AuBr_4]^- + 3e$ - $Au^0 + 4Br^-$.[29] We speculate that such liberated Br^- ions selectively absorb to Au (111) faces as the capping agent.[26] This stabilizes Au {111} facets, and subsequently lead to a slower growth along <111> direction. The same functions of Br^- ions serving as capping agent to facilitate anisotropic growth of different metal nanostructures have been experimentally observed and theoretically simulated.[32,33] The final product was, therefore, two-dimensional AuNPLs bounded with {111} facets on top and bottom. We further investigated the importance of $[AuBr_4]^-$ complex in the formation of AuNPLs on GS. By using $HAuCl_4$ as the gold precursor while keeping the other synthesis conditions unchanged, synthesized nanocomposites via $HAuCl_4$ are shown in Fig. S 2.3(b). Compared to Fig. S 2.3(a), the absence of bromine led to completely different gold nanostructures rather than AuNPLs showing the advantage of $KAuBr_4$ as the gold precursor for synthesizing AuNPLs-GS hybrid. The investigation of concentration of Br- ions influence on size

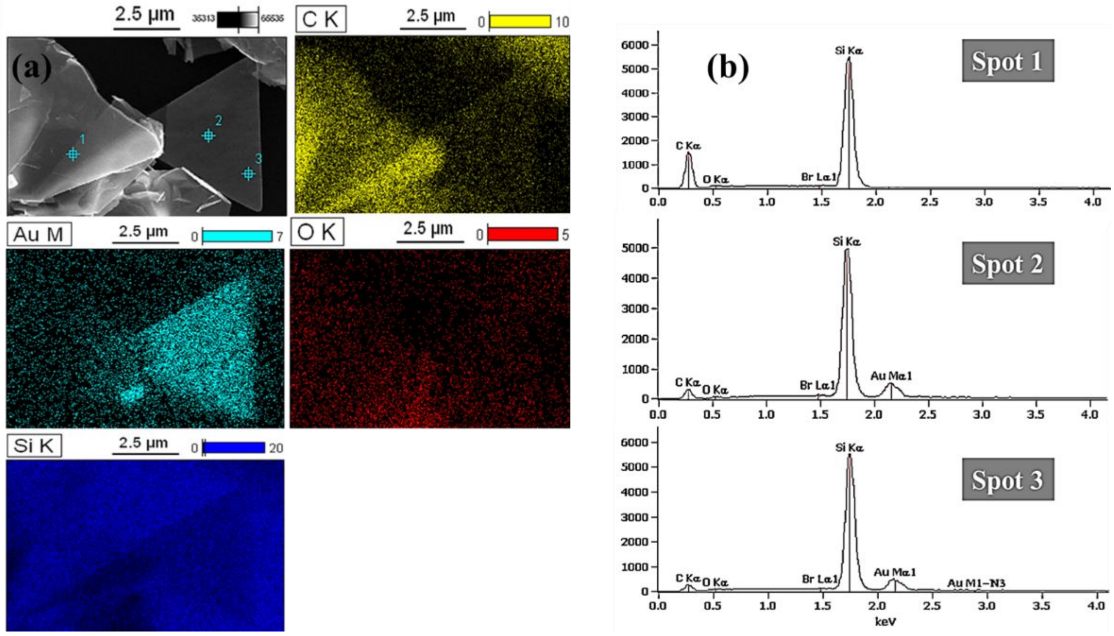

Figure 2.2 (a) EDX mapping of a AuNPL synthesized on GS substrate and (b) elemental analysis on spots 1-3

and geometry of AuNPLs is currently underway. Structures of AuNPLs were investigated by the combination of transmission electron microscopy (TEM) and X-ray diffraction (XRD). Fig. 2.3(a) shows a typical TEM image of a single-layer AuNPL lying on graphene surface. Stress patterns as well as surface wrinkles were observed due to the bending of the thin crystals. The corresponding selected area electron diffraction pattern (SAED) of in Fig. 2.3(b) revealed single-crystalline characteristic of AuNPLs. The diffraction spots were indexed to (220) and 1/3(422) Bragg reflections with a hexagonal spot pattern indicative of preferentially (111)-orientated crystalline structure. The presence of the forbidden 1/3(422) diffraction was due to atomically thin surface of prepared AuNPLs.[34,35] Detailed characterization of AuNPLs thickness later on confirmed the ultrathin characteristic of the AuNPLs. Fig. 2.3(c) shows a high resolution TEM image taken from the edge of the AuNPLs that confirmed the single-crystalline structure of AuNPLs with fringes spacing of 0.250 nm, which precisely corresponded to spacing of 1/3(422) planes. The crystalline structure of the product was further studied by XRD shown in Fig. 2.3(d). All diffraction peaks were assigned to G (002) {26.4°} (insert figure) from layered graphene structure and Au (111) {38.2°}, Au (200) {44.5°}, Au (311) {77.8°} and Au (222) {82.1°} planes from face-centered cubic (FCC) gold crystal. It is noteworthy that strikingly strong intensity of (111) peak as well as its secondary (222) diffraction peak were detected, in contrast to other very weak diffraction peaks of (200) and (311) planes and the missing (220) diffraction peak. Relative diffraction intensity of (200)/(111) was 0.06, which is much lower than Au bulk value at 0.52 from

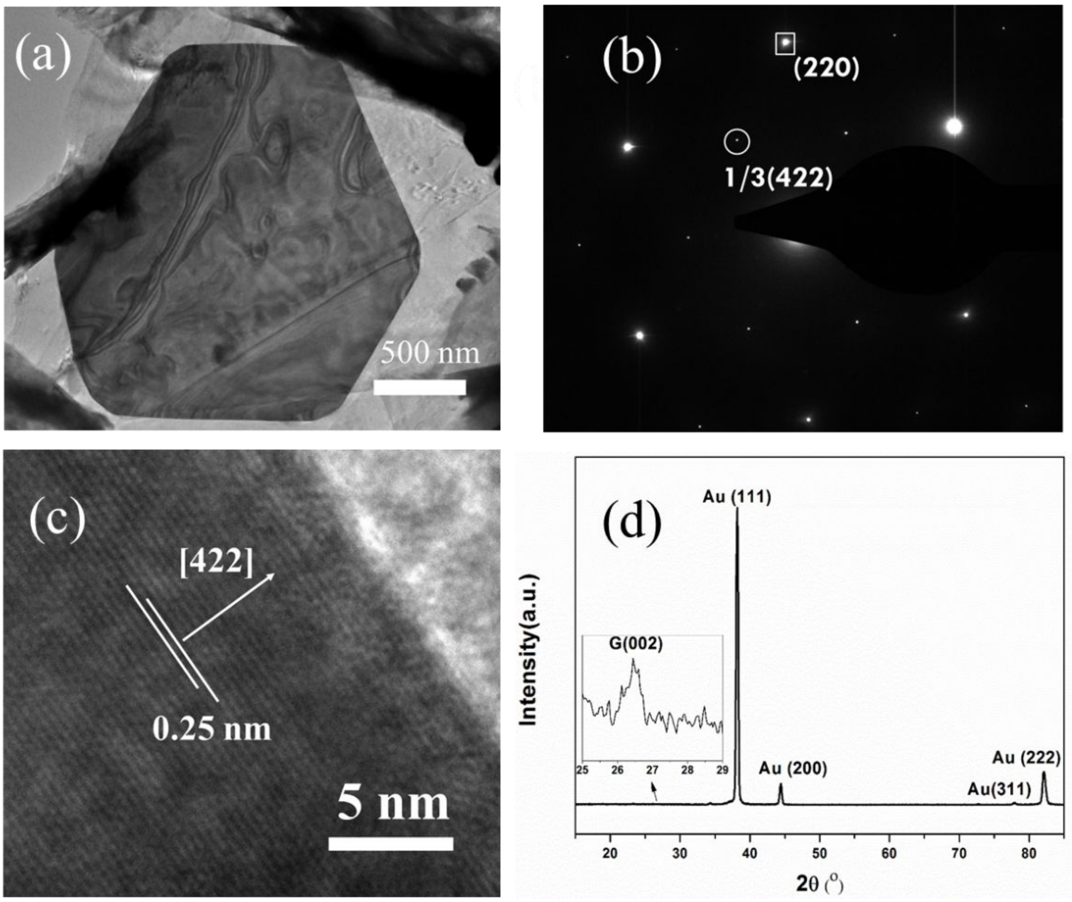

Figure 2.3 Structure characterization of AuNPLs synthesized on GS surfaces at 5hrs (a) TEM image of a representative AuNPL and (b) its corresponding SAED pattern. (c) HRTEM of Au nanoplate and (d) XRD analysis of synthesized AuNPLs-GS hybrid. Insert figure shows graphene sheets (002) diffraction peak.

JCPDS #04-0784, indicating the synthesized AuNPLs were highly (111) oriented. The disappearance of (220) diffraction peak was attributed to atomically thin Au sheets lying flat on GS substrate with strongly preferential (111) orientation. This is similar to a previous report from XRD patterns of gold nanowires and gold nanoplates on reduced graphene oxide.[23] Taking into consideration that scanning area of XRD was at million-meter scale which was larger than SEM, we concluded that high-yield production of AuNPLs with very low percentage of by-products were obtained Randomly distributed by-products, such as Au nanoparticles, would contribute to (220) intensity.

To determine the thickness of as-synthesized AuNPLs, both atomic force microscopy (AFM) and SEM were employed. Fig. 2.4(a) presents representative AFM images of a hexagonal AuNPL synthesized at 5 hours. It elegantly confirmed that the thickness of the chosen AuNPL was approximately 15.0 nm with the edge length at micrometers scale. Fluctuation of the surface line reveals that its surface was not perfectly flat, which was consistent with the SEM and TEM results due to the internal stress within the structure. Furthermore, by means of tilting the sample stage to a certain angle, the thickness of AuNPLs could also be readily identified with SEM shown as Fig. 2.4(b). The thickness of selected Au sheet at 5 hours in Fig. 2.4(b) was 16.2 nm, consistent with the value determined from AFM. We found the average thickness of AuNPLs at 5 hours was 15.5 nm. Thus, the combination of AFM and SEM showed that the AuNPLs synthesized at 5 hours were ultrathin two dimensional gold sheets with the thickness normally less than 20 nm which lead to the

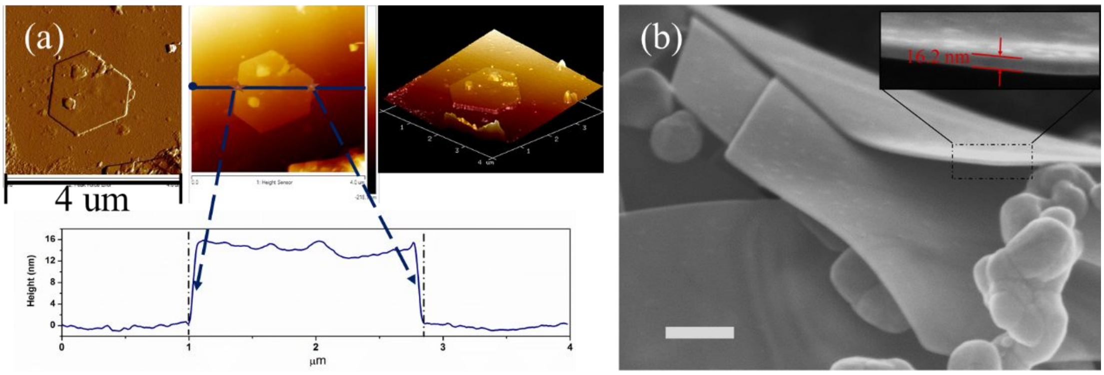

Figure 2.4 (a) AFM measurement shows an isolated ultrathin AuNPLs on substrate at the synthesis time of 5 hours. (b) To confirm the thickness, SEM is also used to investigate the thickness of AuNPLs at different tilt angles. Scale bar 200nm.

Corresponding TEM and XRD results discussed above.

As discussed previously, the performance of Au nanocrystals is strongly dependent on their geometry, to grow AuNPLs with tunable edge length and thickness is therefore of crucial importance. Figure 2.5 illustrates the size and thickness of AuNPLs were treatment time dependent. SEM images of AuNPLs synthesized on GS support at 5 hrs, 24 hrs and 72 hrs were shown in Fig. 2.5(a), (b) and (c), respectively. The most sensitive parameter in the AuNPLs was their edge length. After 5 hours hydrothermal reaction, AuNPLs were observed with the edge length of 1.58 μm on average as shown in Fig. 2.5(a). The average value was evaluated by analyzing 50 randomly chosen AuNPLs. The same method was employed for the following analysis at 24 hours and 72 hours. With the treatment time increasing to 24 hours, their average edge length decreased to sub-micrometer scale, which was about 0.88 μm as shown in Fig. 2.5(b). When the reaction eventually lasted to 72 hours, the average edge length reduced to 0.48 μm as shown in Fig. 2.5(c). Meanwhile, the insert images in Fig. 2.5(a), (b) and (c) showed the variety of thickness along with time. On average, their thickness was 15.5 nm, 42.1 nm and 60.5 nm at 5 hrs, 24 hrs and 72 hrs, respectively. The relationship of edge length and thickness dependent on treatment time was summarized and schematically shown in Fig. 2.5(d).

Besides the edge length and thickness, the geometry of AuNPLs also gradually varied with time. AuNPLs at 5 hrs and 24 hrs showed typical hexagonal and triangular shapes while at 72 hrs, the Au sheets displayed irregular shapes with blunt vertices

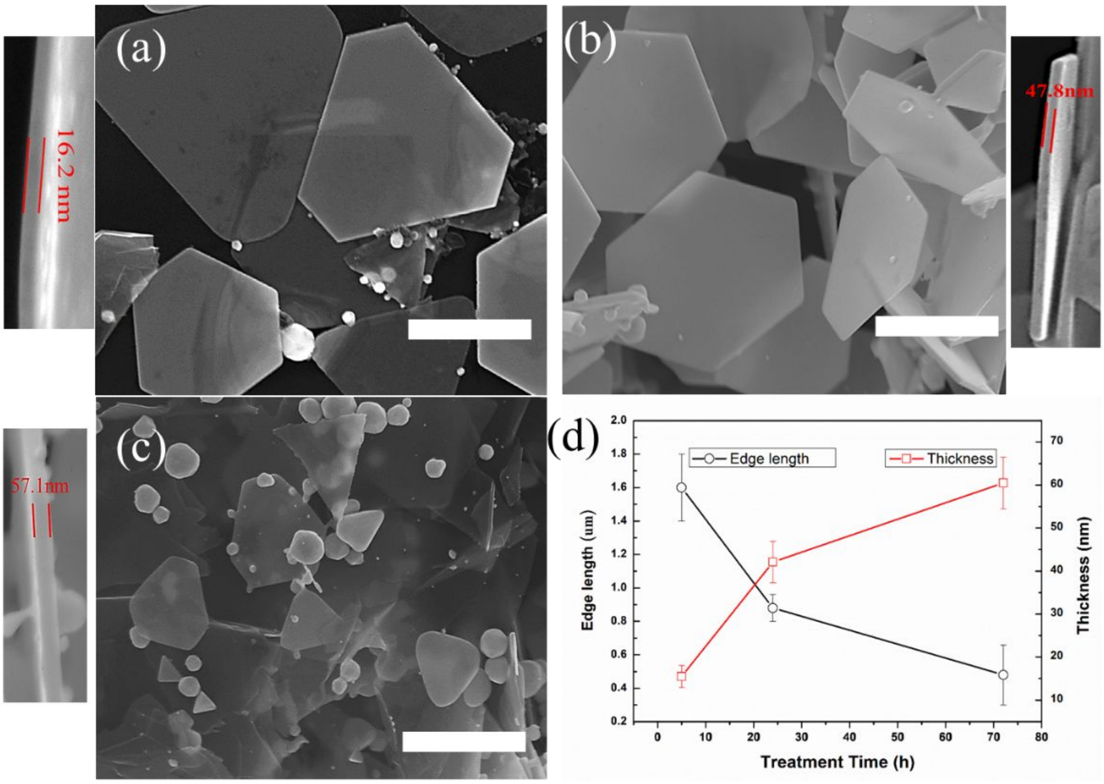

Figure 2.5 SEM images of synthesized AuNPLs on GS at different time (a) 5 hours, (b) 24 hours and (c) 72 hours. (d) relation of average edge length and thickness of AuNPLs with time.

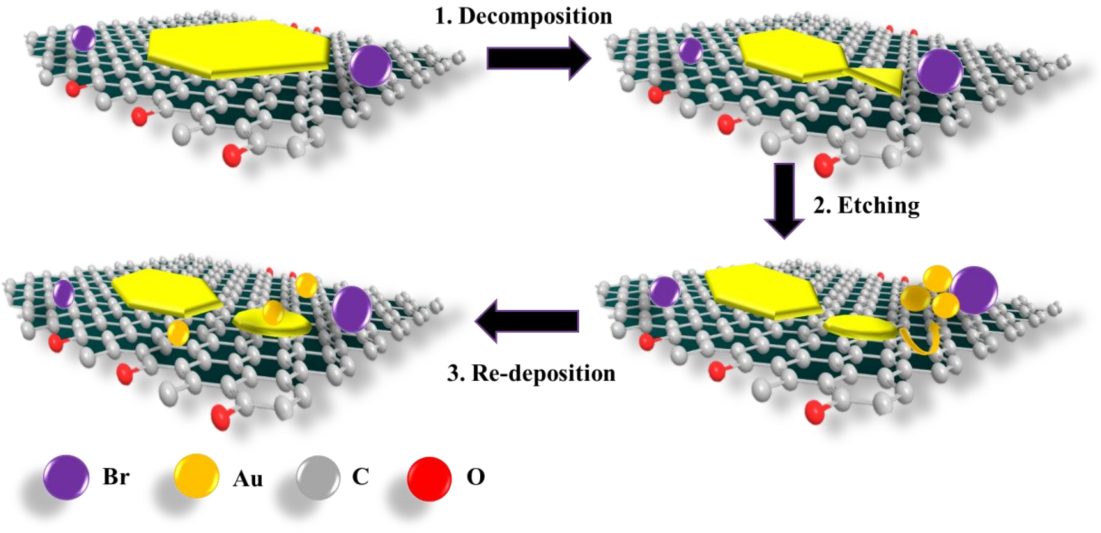

Figure 2.6 Schematic illustration of geometry evolution of AuNPLs on graphene sheets along with time via three-step mechanism.

as shown in Fig. 2.5(c), some of which even “shrunk” into sphere-like nanoparticles. Accordingly, we have proposed a three-step growth mechanism for size and geometry tunable AuNPLs on GS. The mechanism is schematically shown in Fig. 2.6. First, ultrathin AuNPLs experienced thermal decomposition along with time due to their thermal instability in solution. It has been shown that anisotropic Au nanostructure such as gold nanorods were unstable in micelles solution under heat treatment and their aspect ratio decreased with increasing temperature.[36] Such thermal instability induced decomposition resulted in larger amount of Au nanosheets with smaller size as shown in Fig. 2.5(b) and (c). Second, decomposed AuNPLs were etched by liberated Br^- ions in the solution. Halide ions such as I^- and Br^- have been widely reported to show etching effects on metal crystals.[26,37,38] It is evidently believed that Br^- ions got liberated from the transformation of Au^{3+} to Au^0 since EDX detected weak bromine peak over the selected spots (Fig. 2.2(b)). Liberated Br^- ions preferentially etched Au atoms at the higher energetic sites especially at the vertices bounded by (100) and (110) facets[38] which led to the formation of blunter vertexes as illustrated in Fig. 2.6 in etching step. Third, unstable complex was reduced and ripened to form irregular Au sheets and nanoparticles. The complex of etched Au atoms with halide ions ($AuBr_x$) was not stable in the solution and was reduced to Au^0, which re-deposited to surfaces of existing AuNPLs[37]. This re-deposition process eventually led to the thickening of Au sheets as well as increasing amount of Au nanoparticles, which was confirmed by SEM images shown in Fig. 2.5.

Raman spectroscopy is massively employed as an efficient powerful technique for characterizations of structure, disorder and doping level of graphene[39,40] and graphene-based hybrid materials.[5,14] Thus, in order to study the interactions particularly the charge transfer between AuNPLs and graphene sheets surface, Raman spectrum was measured on AuNPLs-GS hybrid platform at different treatment periods. The principle of Raman scattering on prepared samples is schematically presented in Fig. 2.7(a). Under the irradiation with ~1.58 eV laser beam (wavelength 785nm), GS platform showed greatly enhanced Raman signals due to AuNPLs decoration as revealed in Fig. 2.7(b). Here are two noticeable aspects from Fig. 72.(b) that are necessary to be discussed in detail. First, three pronounced peaks of graphene, which were assigned to D (1307–1315 cm^{-1}), G (1572–1580 cm^{-1}) and 2D (2642 – 2647 cm^{-1}) bands presented in all four samples but the intensity of each band was very distinct. The relative intensity of I_D/I_G is usually used to characterize disorder of graphene while I_{2D}/I_G is an important parameter to identify the doping density of graphene[39]. Second, AuNPLs decorating graphene sheets eventually contributed to stronger Raman signals along with time, in other words, along with their size and geometry. The relative intensity of D-band of AuNPLs-GS over D-band of pristine GS could be noted as Raman signals enhancement factor.[14] Thus, three important parameters of Raman scattering on graphene, i.e. I_D/I_G, I_{2D}/I_G and enhancement factor (EF) are summarized in Table 2.1.

From Table 2.1, we observe increasing values of I_D/I_G with time, from 0.24 as of pristine GS to 1.03 as of AuNPLs-GS at 72 hours, indicating that graphene surfaces became more disordered, that is to say, more surface defects were created. This result

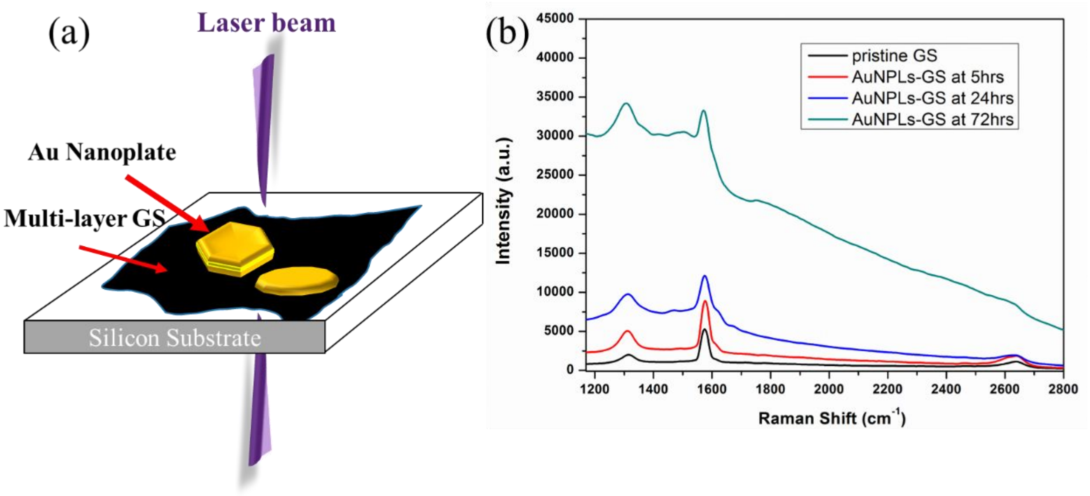

Figure 2.7 (a) Schematic illustration of Raman scattering on AuNPLs-GS platform (b) Raman spectrum of pristine GS, AuNPLs-GS at 5 hours, 24 hours and 72 hours.

was understandable with regard to the fact that the redox reaction incessantly occurred within 72 hours wherein graphene served as the reductant. We suggest that the reaction had not been stopping for 72 hours according to re-deposition mechanism illustrated in Fig. 2.6 where small unstable Au-Br complex was repeatedly reduced to Au clusters by graphene, leading to more disordered graphene. On the other hand, I_{2D}/I_G was suppressed and eventually reduced from 0.18 to 0.05, showing a gradual increase of doping intensity. The suppression of I_{2D}/I_G has been detected in both p-type and n-type doping of graphene while the position shift of 2D-band identifies the doping type.[39,40]

In this report, 2D-band exhibited a clear redshift to longer wavelength positions along with time (Fig. S 2.4), which demonstrated n-type doping of graphene sheets from AuNPLs decoration. In this case, electrons were supposed to transfer from AuNPLs as the electron donors to graphene sheets as the electron acceptors, which subsequently caused chemical enhancement of Raman scattering.[13] By means of chemical enhancement involving charge transfer interaction, Raman signals enhancement factor for graphene usually varies from less than 10 to 100, which is a few orders of magnitude lower than that of electromagnetic enhancement involving physical interaction.[41] Accordingly, we detected enhancement factors at 5 hours and 24 hours were 2.53 and 4.87, which were mainly attributed to the chemical enhancement. Overall, larger EFs were probed along with increasing doping intensities (I_{2D}/I_G). Nevertheless, the correlation of enhancement factor and I_{2D}/I_G was non-linear (Fig. S 2.5), particularly there showed a sharp increase of enhancement factor up to 17.07 at 72 hours. This suggests the electromagnetic enhancement may occur at 72 hours due to the appearance of more dense Au nanoparticles (Fig. 2.5(c)) which serve as efficient "hot spots" with localized electromagnetic field[42] for Raman scattering enhancement.

Table 2.1 Important parameters of pristine GS (p-GS) and AuNPLs-GS from Raman spectrum

	p-GS	5 h	24 h	72 h
I_D/I_G[a]	0.24	0.57	0.80	1.03
I_{2D}/I_G[a]	0.18	0.16	0.09	0.05
EF[b]	1	2.53	4.87	17.07

a. Values obtained from Raman scattering spectrum normalizing to G intensity.
b. Values obtained by normalizing intensity of D-band to that of pristine-GS.

2.4 Conclusion

In conclusion, we have synthesized high-yield single-crystalline AuNPLs on multi-layer graphene sheets with one-step strategy. We showed that $KAuBr_4$ is a proper gold precursor for decorating anisotropic Au sheets/plates on graphene support. By means of controlling synthesis time, we were able to obtain AuNPLs with tunable size and geometry. According to their size and geometry evolution, we proposed a growth mechanism via three-step process including thermal decomposition, Br^- etching and re-deposition. Furthermore, we correlated the Raman signals enhancement of graphene to the size and geometry of AuNPLs. It showed the geometry of Au nanocrystals may lead to significant differences on Raman enhancement magnitude of graphene surfaces, which is potentially useful for future fabrication of graphene based surface enhancement Raman scattering (SERS) substrate.

2.5 References

1. R. R. Nair, P. Blake, A. N. Grigorenko, K. S. Novoselov, T. J. Booth, T. Stauber, N. M. R. Peres and A. K. Geim, *Science*, 2008, **320**, 1308

2. C. Lee, X. D. Wei, J. W. Kysar and J. Hone, *Science*, 2008, **321**, 385

3. A. A. Balandin, S. Ghosh, W. Bao, I. Calizo, D. Teweldebrhan, F. Miao and C. N. Lau, *Nano Lett.,* 2008, **8**, 902

4. M. D. Stoller, S. Park, Y. Zhu, J. An and R. S. Ruoff, *Nano Lett.*, 2008, **8**, 3498

5. W. Fan, Y. H. Lee, S. Pedireddy, Q. Zhang, T. Liu and X. Y. Ling, *Nanoscale*, 2014, **6**, 4843–4851

6. X. M. Chen, G. H. Wu, J. M. Chen, X. Chen, Z. X. Xie and X. R. Wang, *J. Am. Chem. Soc.*, 2011, **133**, 3693–3695

7. E. J. Yoo, T. Okata, T. Akita, M. Kohyama, J. Nakamura and I. Honma, *Nano Lett.*, 2009, **9**(6), 2255–2259

8. X. Xiao, J. R. Michael, T. Beechem, A. McDonald, M. Rodriguez, M. T. Brumbach, T. N. Lambert, C. M. Washburn, J. Wang, S. M. Brozik, D. R. Wheeler, D. B. Burckel and R. Polsky, *J. Mater. Chem.*, 2012, **22**, 23749–23754

9. R. Zan, U. Bangert, Q. M. Ramasse and K. S. Novoselov, *J. Phys. Chem. Lett.*, 2012, **3**, 953–958

10. Y. Liu, R. Cheng, L. Liao, H. Zhou, J. Bai, G. Liu, L. Liu, Y. Huang and X. Duan, *Nat. Commun.*, 2011, **2**, 579.

11. J. Zhu, Q. H. Liu and T. Lin, *Nanoscale*, 2013, **5**, 7785–7789.

12. W. Wang, J. Gu, W. Hua, X. Jia and K. Xi, *Chem. Commun.*, 2014, **50**, 8889

13. K. Jasuja and V. Berry, *ACS Nano*, 2009, 3, 2358

14. Y. K. Kim, H. K. Na, Y. W. Lee, H. Jang, S. W. Han and D. H. Min, *Chem. Commun.*, 2010**, 46**, 3185–3187.

15. A. N. Sidorov , G. W. Slawinski , A. H. Jayatissa , F. P. Zamborini , G. U. Sumanasekera , *Carbon*, 2012, **50**, 699 – 705

16. F. Schedin, E. Lidorikis, A. Lombardo, V. G. Kravets, A. K. Geim, A. N. Grigorenko, K. S. Novoselov and A. C. Ferrari, *ACS Nano*, 2010, **4**, 5617–5626

17. S. Z. Nergiz, N. Gandra, S. Tadepalli and S. Singamaneni, *ACS Appl. Mater. Interfaces*, 2014, **6**, 16395–16402

18. S. Lee, P. Kumar, Y. Hu, G. J. Cheng and J. Irudayaraj, *Chem. Commun.*, 2015, **51**, 15494–15497

19. Z. Li, Y. Yu, Z. Chen, T. Liu, Z.-K. Zhou, J.-B. Han, J. Li, C. Jin and X. Wang, *J. Phys. Chem. C*, 2013, **117**, 20127–20132

20. L. Scarabelli, M. Coronado-Puchau, J. J. Giner-Casares, J. Langer and L. M. Liz-Marzán, *ACS Nano*, 2014, **8**, 5833–5842

21. S. S. Shankar, A. Rai, B. Ankamwar, A. Singh, A. Ahmad and M. Sastry, *Nat. Mater.*, 2004, **3**, 482–488.

22. X. Huang, S. Z. Li, Y. Z. Huang, S. X. Wu, X. Z. Zhou, S. Z. Li, C. L. Gan, F. Boey, C. A. Mirkin and H. Zhang, *Nat. Commun.*, 2011, **2**, 292

23. J. Wang, X. C. Dong, R. Xu, S. Z. Li, P. Chen and M. B. Chan-Park, *Nanoscale*, 2012, **4**, 3055–3059

24. T. H. Ha, H.-J. Koo and B. H. Chung, *J. Phys. Chem. C*, 2007,**111**, 1123-1130

25. D. V. R. Kumar, A. A. Kulkarni and B. L. V. Prasad, *Colloids Surf., A*, 2013, **422**, 181–190

26. N. Garg, C. Scholl, A. Mohanty and R. Jin, *Langmuir*, 2010, **26**, 10271–10276

27. M. R. Langille, M. L. Personick, J. Zhang and C. A. Mirkin, *J. Am. Chem. Soc.*, 2012, **134**, 14542–14554.

28. Y. Xia, Y. J. Xiong, B. Lim and S. E. Skrabalak, *Angew. Chem., Int. Ed.*, 2008, **48**, 60

29. B. J. Plowman, A. P. O'Mullane, P. R. Selvakannan and S. K. Bhargava, *Chem. Commun.*, 2010, **46**, 9182–9184

30. A. Marinkas, F. Arena, J. Mitzel, G. M. Prinz, A. Heinzel, V. Peinecke and H. Natter, *Carbon*, 2013, **58**, 139–150

31. H. C. Choi, M. Shim, S. Bangsaruntip and H. Dai, *J. Am. Chem. Soc.*, 2002, **124**, 9058-9059

32. Y. Xia, X. Xia and H.-C. Peng, *J. Am. Chem. Soc.*, 2015, **137**, 7947–7966

33. G. J. Leong, A. Ebnonnasir, M. C. Schulze, M. B. Strand, C. Ngo, D. Maloney, S. L. Frisco, H. N. Dinh, B. Pivovar, G. H. Gilmer, S. Kodambaka, C. V. Ciobanu and R. M. Richards, *Nanoscale*, 2014, **6**, 11364-11371

34. H. L. Qin, D. Wang, Z. L. Huang, D. M. Wu, Z. C. Zeng, B. Ren, K. Xu and J. Jin, *J. Am. Chem. Soc.*, 2013, **135**, 12544–12547

35. C. C. Li, W. P. Cai, B. Q. Cao, F. Q. Sun, Y. Li, C. X. Kan and L. D. Zhang, *Adv. Funct. Mater.*, 2006, **16**, 83-90

36. M. B. Mohamed, K. Z. Ismail, S. Link and M. A. El-Sayed, *J. Phys. Chem. B*, 1998, **102**, 9370–9374

37. L. Chen, F. Ji, Y. Xu, L. He, Y. Mi, F. Bao, B. Sun, X. Zhang and Q. Zhang, *Nano Lett.*, 2014, **14**, 7201-7206

38. M. Kim, Y. W. Lee, D. Kim, S. Lee, S. R. Ryoo, D. H. Min, S. B. Lee and S. W. Han, *ACS Appl. Mater. Interfaces*, 2012, **4**, 5038-5043

39. A. Das, S. Pisana, B. Chakraborty, S. Piscanec, S. K. Saha, U. V. Waghmare, K. S. Novoselov, H. R. Krishnamurthy, A. K. Geim, A. C. Ferrari and A. K. Sood, *Nat. Nanotechnol.*, 2008, **3**, 210-215

40. S. Huh, J. Park, Y. S. Kim, K. S. Kim, B. H. Hong and J. M. Nam, *ACS Nano*, 2011, **5**, 9799-9806

41. Huang, X. Ling, L. Liang, Y. Song, W. Fang, J. Zhang, J. Kong, V. Meunier and M. S. Dresselhaus, *Nano Lett.*, 2015, **15**, 2892

42. C. E. Talley, J. B. Jackson, C. Oubre, N. K. Grady, C. W. Hollars, S. M. Lane, T. R. Huser, P. Nordlander and N. J. Halas, *Nano Lett.*, 2005, **5**, 1569–1574

2.6 Supplementary Information

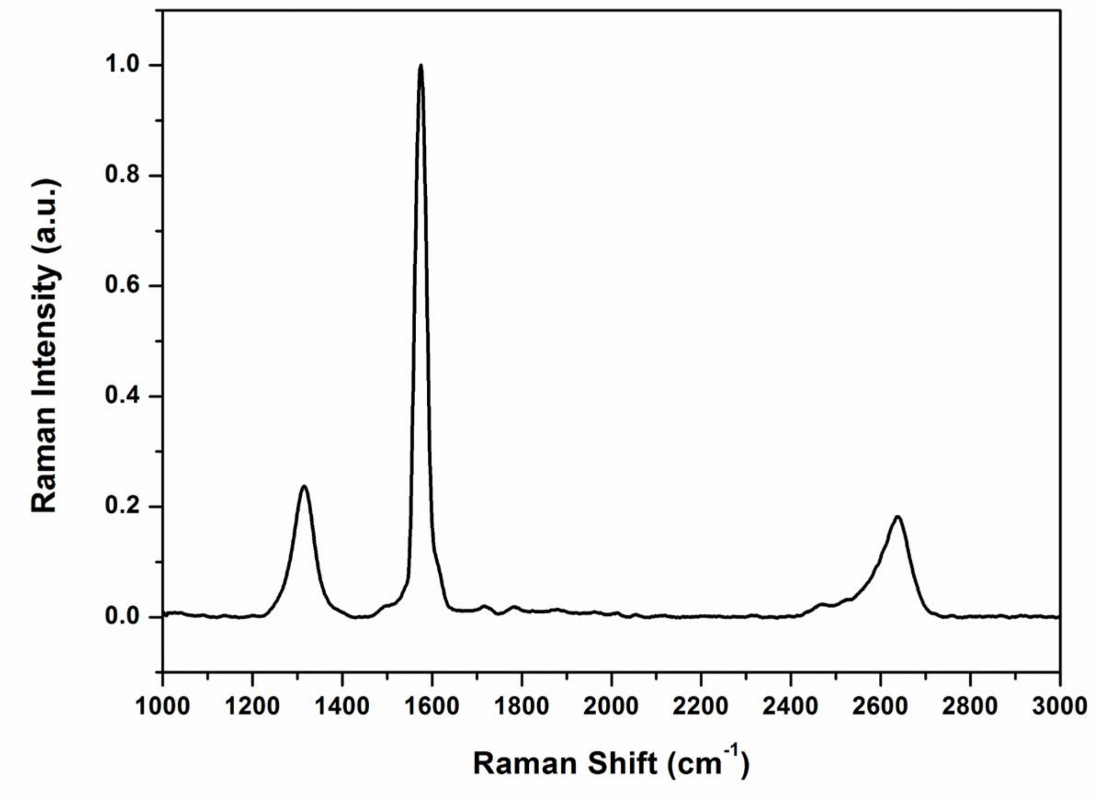

Figure S 2.1 Raman spectrum of as-received AO-2. All intensity was normalized to G peak intensity. In this measurement, I_D/I_G is around 0.24.

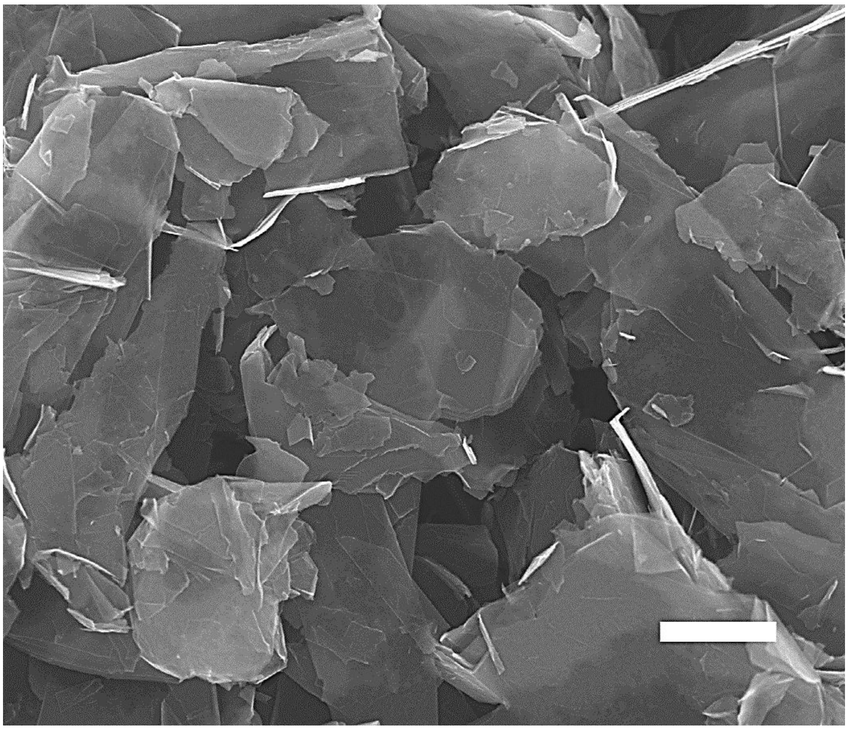

Figure S 2.2 SEM image of as-received multi-layer graphene sheets (AO2) after ultrasonication. Scale bar: 2 µm

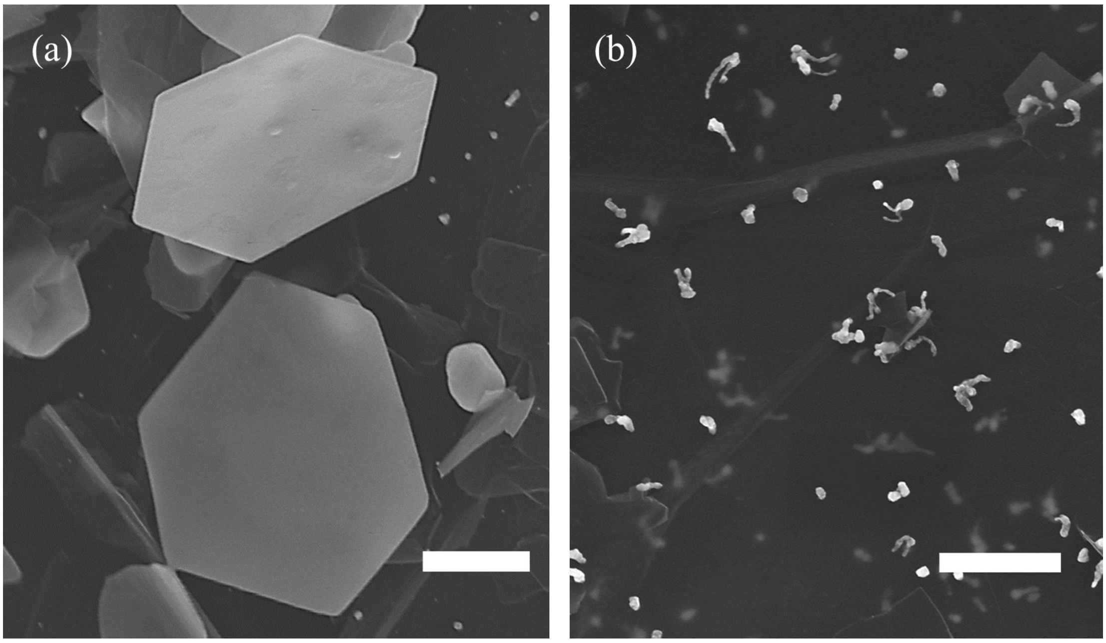

Figure S 2.3 SEM images of (a) AuNPLs-GS hybrid obtained with $KAuBr_4$ as gold precursor and (b) irregular Au nanostructures on GS with $HAuCl_4$ as gold precursor. Scale bar: 500 nm

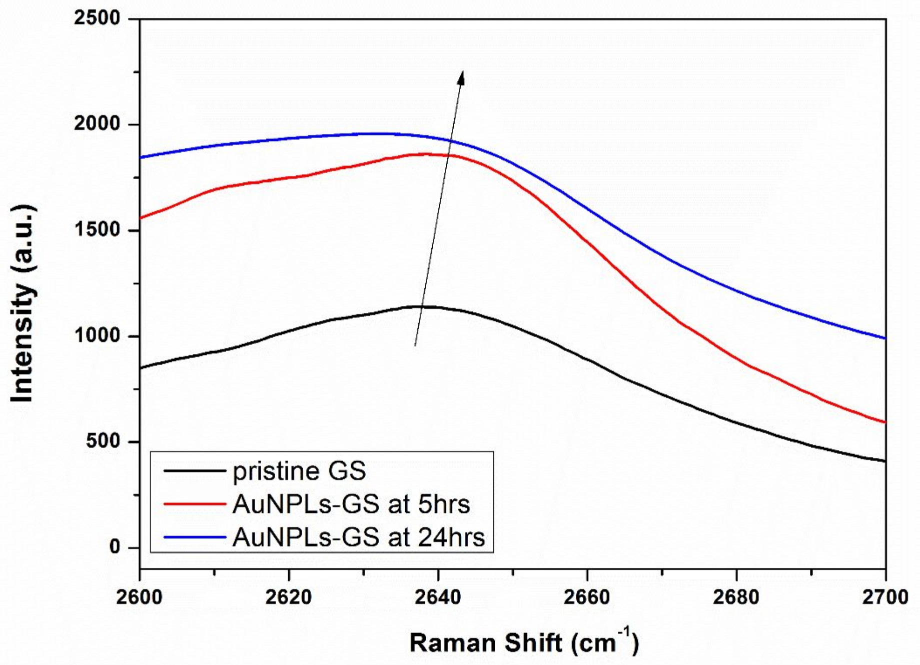

Figure S 2.4 Raman spectrum of 2D band positions of pristine graphene sheets (GS) AuNPLs-GS at 5 hours and AuNPLs-GS at 24 hours. 2D band position of AuNPLs-GS at 72 hours is not displayed here due to much higher intensity.

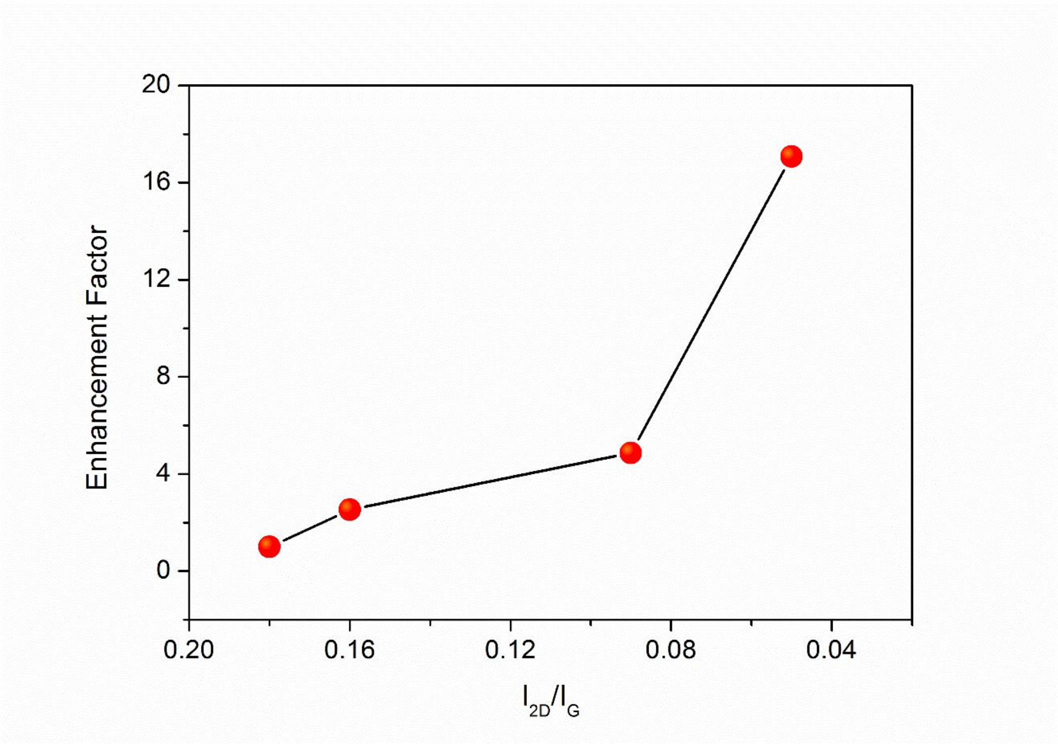

Figure S 2.5 Correlation of I_{2D}/I_G with Raman enhancement factor.

Chapter 3 A Novel Flexible Substrate for Surface Enhanced Raman Scattering (SERS) based on Carbon Nanotube Sheet-Gold Nanoplates Hybrid

Abstract

In this report, we have demonstrated a simple route for in-situ synthesis of two dimensional (2-D) Au nanoplates (AuNPLs) on carbon nanotube (CNT) sheet. Morphology and structure investigations by means of SEM, TEM and XRD confirm that AuNPLs normally with the size at micrometer-scale are single-crystalline with face-centered cubic (FCC) structure that are highly (111)-oriented. We have explored the role of Br^- ions in inducing the formation of AuNPLs and suggested Br^- ions can preferentially bind to the specific Au facets, stabilize the corresponding planes and promote the anisotropic growth of plate-like Au sheets. The CNT sheets-AuNPLs hybrid has been further exploited as a novel flexible surface enhanced Raman scattering (SERS) substrate, which reveals the capability of probing the analyte Rhodamine 6G (Rh6G) at extremely low concentration ($\sim 10^{-7}$ M). AuNPLs decorated CNT sheets present much higher SERS sensitivity compared to that of CNT sheets anchored with Au nanoparticles mainly due to rather larger surface areas of AuNPLs.

3.1 Introduction

Surface enhanced Raman scattering (SERS) has been intensively investigated in the past few decades as an efficient technique for label-free, real time sensing and monitoring of chemical and biological analyte at extremely low concentrations.[1,2] Raman signals from analyte molecules that absorb to a rough surface of noble metals can be amplified by several orders of magnitude due to the localized electromagnetic field and the charge-transfer complexes, the combination of which can contribute to an enhancement factor as high as $\sim 10^{10}$-10^{11}.[3,4] Despite great improvement of SERS substrates on sensitivity, reproducibility, cost and so forth have been achieved recently, many challenges still remain. In particular, conventional SERS substrates such as glass, quartz and silicon are usually brittle and inflexible with limited surface areas which hinders their further applications. For example, the analyzing means associated with such inflexible substrates are invasive, which could be harmful for the ancient art objects when probing the dyes.[5] Moreover, flexible SERS substrates can be employed in packaging, which will benefit their use in specially desired positions such as wrapping around the non-planar substrates during testing.[6,7]

Owing to the great advantages discussed above, a growing interest has been raised to develop flexible SERS substrates, substantially by integrating plasmonic nanoparticles like Au and Ag with flexible matrices, such as paper,[8] polymethyl methacrylate (PMMA) template,[9] and poly(vinyl alcohol) (PVA) nanofiber film.[10] However, such materials are vulnerable when exposed to external forces and harsh environment. Alternatively, researchers have discovered that graphene substrates normally flexible would also create enhanced Raman signals for low concentration of organic solvents, known as G-SERS substrate.[11,12] Nevertheless, the enhancement from graphene sheet mainly arises from chemical mechanism (CM) instead of electromagnetic mechanism (EM), which led to rather low sensitivity.[13] On the other hand, despite impregnating plasmonic nanoparticles on graphene surfaces would contribute to a significant enhancement of Raman signals, large-scale fabrication of such hybrid substrate is tedious and complicated. Therefore, it is highly desirable to develop novel flexible SERS platforms that possess excellent sensitivity, mechanical stability a scale-up feasibility through simple routes.

Carbon nanotube (CNT) is extensively considered as one of the next-generation materials because it is light, ultra-strong and highly conductive.[14,15] As an example, the measured tensile strength and elastic modulus of individual multi-walled carbon nanotubes (MWNTs) are up to 100 GPa and 1TPa, respectively.[16] Not less important is the assemblies made of CNT network presenting high flexibility so that they have been widely exploited as a key part to fabricate flexible devices such as light-emitting diodes, solar cells and supercapacitors.[17-19] Thanks to the great advances in CNT growth and synthesis in recent years, scale-up production of CNT assemblies in macrostructures such as yarns and sheets eventually becomes practical.[20,21] Despite the superior properties of individual CNTs can be hardly preserved in their macro-structural assemblies due to structural defects and poor bundles alignment,[21] CNT yarns and sheets still perform attractive characteristics compared to conventional materials. For instance, the macro-structural sheets of CNT exhibit maximum mechanical strength measured as 10.8 GPa which is higher than any industrial fibers.[22] Meanwhile CNT fiber exhibits much higher chemical stability than that of traditional metal wires when subjected to harsh conditions such as HCl solution.[23] Thus, hybrid platforms made of CNT yarns/sheets coupling with Au or Ag nanocrystals are ideal candidates for flexible SERS substrates. Accordingly, Zhang et. al fabricated flexible SERS substrate by means of uniformly incorporating Au nanoparticles into CNT film, which showed high sensitivity and reproducibility.[24] However, very dense loads of plasmonic nanoparticles, namely short inter-particle gaps[25,26] are indispensable in order to maintain excellent sensitivity which can compromise the light-weight merit of such SERS substrate and cause a number of issues with regard to the cost.

Herein, we have devised a novel flexible SERS substrate based on the decoration of Au nanoplates (AuNPLs) on CNT sheet. As an alternative, Au nanoplates also perform ultra-sensitive detection of the chemical analyte due to the enhancement of localized electrical field replying on their localized surface plasmon resonance (LSPR).[27] The highlights of this work are the following (1) we reveal, for the first time, a facile and simple strategy for one-pot synthesis of CNT sheet-AuNPLs hybrid. (2) when the hybrid utilized as SERS substrate, it is capable of identifying Rhodamine 6G (Rh6G), a highly fluorescent dye at the concentration as low as ~10^{-7} M, indicative of an ultrasensitive flexible SERS platform. (3) We evidently show CNT sheet-AuNPLs platform display a higher sensitivity compared to the substrate made of CNT sheet coupling with Au nanoparticles, confirming the advantageous function of

AuNPLs for SERS applications and (4) the selected CNT sheet is commercially available which potentially enables its further scale-up fabrication.

3.2 Experimental

3.2.1 Chemicals and Materials

CNT sheets were received from Nanocomp Technologies Inc. (Merrimack, NH), which was fabricated by a continues chemical vapor deposition (CVD) process classified as dry spinning process. Nanotubes grown with iron catalysts in the CVD furnace was subsequently collected onto a drum with a rotating velocity of ~15m/min to impart alignment in the drawing direction. Thus, CNT sheets used in this work are virtually scale-up production. Gold chloride hydrate ($HAuCl_4 \cdot xH_2O$, 99.999%) and potassium bromide (KBr, ACS reagent, >99.0%) was purchased from Sigma-Aldrich, USA. L-ascorbic acid (>99.0%) and Rhodamine 6G (99%) were obtained from Fisher scientific, USA.

3.2.2 Preparation of CNT sheet-Au nanocrystal hybrids

6 cm×2 cm CNT sheet stripe was cut from the supplied CNT sheet and kept in a glass vial that contained 18ml DI H_2O. 35 mg $HAuCl_4$ (28.5 mM) and a certain amount of KBr in DI water were added to the vial. After the mixture was homogeneous dispersed with gently shaking, 0.4 mL ascorbic acid (400 μM) was then mixed with the solution. The mixture was maintained at 90 ^{o}C for 8 hours for complete redox reaction. Subsequently, CNT sheet was taken out from the solution and washed with DI water. CNT sheet-AuNPLs hybrid was finally dried in the vacuum oven at 100 ^{o}C overnight.

3.2.3 Characterizations

Electron microscopy studies and X-ray diffraction (XRD) analysis were carried out in order to understand the morphologies and structures of CNT sheet-AuNPLs hybrid. SEM coupled with energy dispersive X-ray (SEM/EDX) analysis was obtained with FEI Nova NanoSEM 230. To prepare samples for scanning electron microscopy (SEM), the CNT sheet-AuNPL stripe was cut into small pieces with the size matching to SEM holder and then taped to conductive carbon tape on SEM holder. Transmission electron microscopy (TEM) images were captured with a FEI T12 Quick CryoEM with the accelerating voltage at 120 keV. The X-ray diffraction (XRD) measurements were performed on a Bede D1 diffractometer using Cu Kα1 radiation from a laboratory tube source. They were under double axis diffraction conditions. The step size of the $2\theta - \omega$ scans was 0.04 degrees and the count time was 3 seconds.

3.2.4 SERS performance

Raman spectral analysis was obtained with a Renishaw In-Via Raman system with the laser length of 785 nm and expose time of 10 s. To prepare the samples for Raman measurement, the obtained CNT sheet stripe impregnated with gold nanocrystals was immersed into appropriate volume of Rh6G solutions with various concentrations for a certain period, ensuring the analyte molecules sufficiently absorb on the substrate surface. The sample was then transferred to Raman equipment to make sure the substrate was not fully dried and corresponding Raman signals were recorded and analyzed.

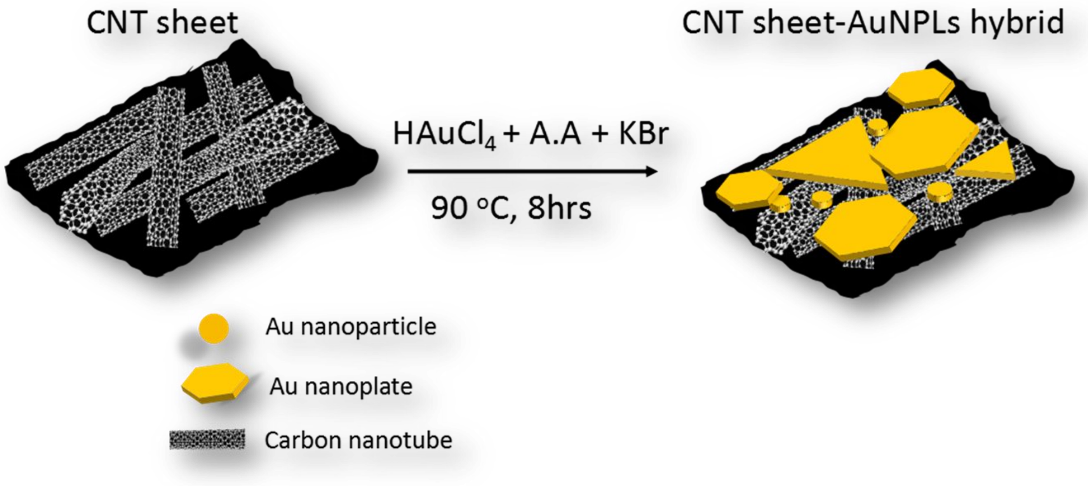

Scheme 3.1 Schematic illustration of one pot synthesis of AuNPLs on CNT sheet

3.3 Result and Discussion

Scheme 3.1 depicts one-pot process for the fabrication of CNT sheet anchored with AuNPLs. In particular, $HAuCl_4$ serving as the gold precursor was reduced to Au clusters with ascorbic acid (A.A) and the Au clusters would be immobilized on graphitic surfaces where the anchoring sites for gold nuclei were abundant. Anisotropic growth of AuNPLs occured due to the addition of KBr from which Br^- ions got liberated in the solution and played as capping agent. The roles of Br^- ions in guiding AuNPLs growth would be stressed in details in the following discussion. After sufficient nucleation and growth time, AuNPLs were uniformly dispersed on CNT sheet substrate.

Detailed morphology study of synthesized AuNPLs on CNT sheet with sufficient capping agent (80mg 25 mM KBr, the as-produced AuNPLs were representative with this concentration for all the following characterizations except for otherwise clarification) were carried out with SEM. Fig. 3.1 shows the typical SEM images of AuNPLs synthesized on CNT sheet at 8 hours. For comparison, pristine CNT sheet was also studied and the corresponding image was listed in Fig. 3.1(a). Carbon nanotube bundles were randomly entangled and cross-linked through the sheet surface, forming a porous "doormat". The porous CNT network provided large surface areas, in other words, the anchoring sites for AuNPLs. Fig. 3.1(b) exhibited sufficient number of AuNPLs uniformly deposited on CNT sheet, indicating the synthesis method in this work was efficient for large-scale production of AuNPLs on CNT support. A higher magnification image shown in Fig. 3.1(c) confirmed well-defined

AuNPLs were synthesized on CNT sheet. It was noteworthy that the synthsized AuNPLs could be identified as triangular and hexgonal plates and their size displayed a wide range from sub-micrometer to a few micrometers. Of particular interest was their locations. Not only the AuNPLs residing on top of CNT sheet were observed, but also a portion of AuNPLs buried in CNT bundles was found (arrows pointed), suggesting inside layers of CNT bundles also had immobilization sites for Au clusters at nucleation stage. Fig. 3.1(d) showed the side view image of two overlaped AuNPLs, which evidently justified one of them locating beneath CNT bundles. In addition, the measured thickness of two AuNPLs were 53.6 nm and 57.0 nm, suggesting the layers of obtained AuNPLs were uniform and ultra-thin.

In order to examine the elemental information of synthesized AuNPLs, we analyzed the elements of the CNT sheet-AuNPLs hybrid with energy dispersive X-ray spectroscopy (EDX). Fig. 3.2(a) shows Au elemental line scanning through the selected area including two AuNPLs. The line encountered a large jump when reached to the edge of the first AuNPL and descent sharply when came to the CNT substrate border. Fluctuation of Au element line was observed through AuNPL surface probably due to small Au nanoparticles beneath the AuNPL. Even larger line jump was observed for the second AuNPL possibly because it was thicker than the first plate. Thus, the elemental line scanning identified the selected AuNPLs were gold. Moreover, elemental spectra of the corresponding domain shown in Fig. 3.2(b) presented C, O, Fe and striking intense Au peaks. While the elements of C, O, Fe were ascribed to CNT, it was reasonable to suggest that Au element resulted primarily

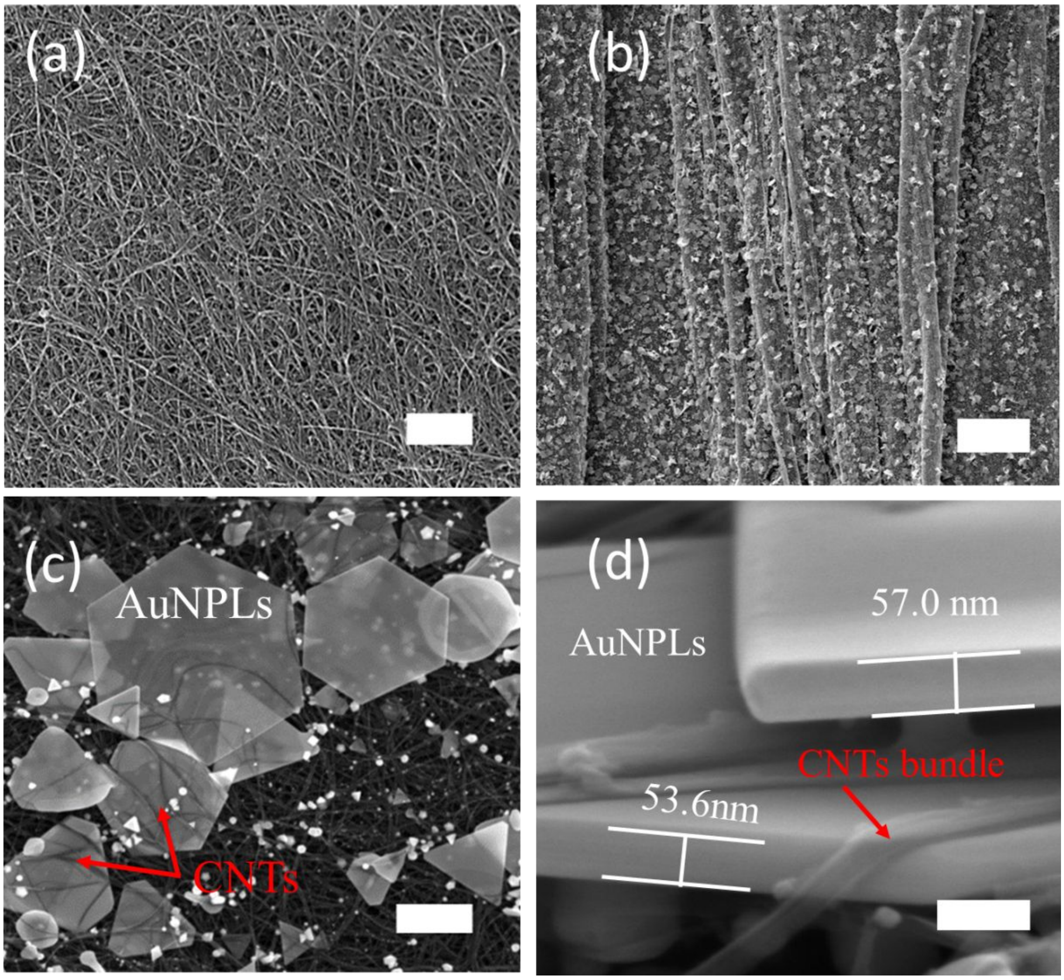

Figure 3.1 Morphology of CNT sheet and CNT sheet-AuNPLs hybrid. (a) SEM image of control CNT sheet. Scale bar:1 μm. (b) representative SEM image of AuNPLs synthesized on CNT sheet. Scale bar: 25μm. (c) high magnification image of AuNPLs deposited on CNT surface. Scale bar:1 μm. (d) side view of two AuNPLs. Scale bar: 100 nm.

from AuNPLs and partially from small Au nanoparticles. Meanwhile we also counted their edge length and thickness from SEM images of 80 randomly observed AuNPLs synthesized with sufficient capping agent KBr and the statistical analysis was presented in Fig. 3.2(c) and (d). The most frequently observed edge length of AuNPLs was in the range of 2.0-2.5μm with a large variety from sub-1μm to more than 3μm while the thickness of AuNPLs was mostly less than 100 nm with the most frequently measured range from 50 nm to 70 nm. The ultrahigh relative ratio of edge length over thickness gave rise to super large surface areas in contrast to sphere-like particles with the same volume, which were highly suitable for SERS applications that would be discussed in the following paragraphs.

The crystalline structure of AuNPLs was investigated with XRD and the corresponding spectra was shown in Fig. 3.3(a). Accordingly, we assigned all diffraction peaks to CNT {002} (26.0°) from carbon nanotubes together with Au {111} (38.1°), Au {200} (44.3°) and Au {311} (77.5°) planes from face-centered cubic (FCC) gold crystal. It was impressive that Au {111} peak displayed very strong intensity compared to weak diffraction peaks of Au {200}, Au {220} and Au {311} planes. The diffraction intensity ratio of Au {200} /Au {111} was 0.34, lower than bulk gold value (0.52 from JCPDS #04-0784), suggesting the synthesized AuNPLs were preferentially {111} oriented. However, the value 0.34 was much larger than that of AuNPLs synthesized on graphene sheets which was 0.06 in our previous report. It likely resulted from two aspects (1) a certain percentage of AuNPLs lied on CNT sheet with random angles instead of paralleling to the substrate as in the case of AuNPLs on

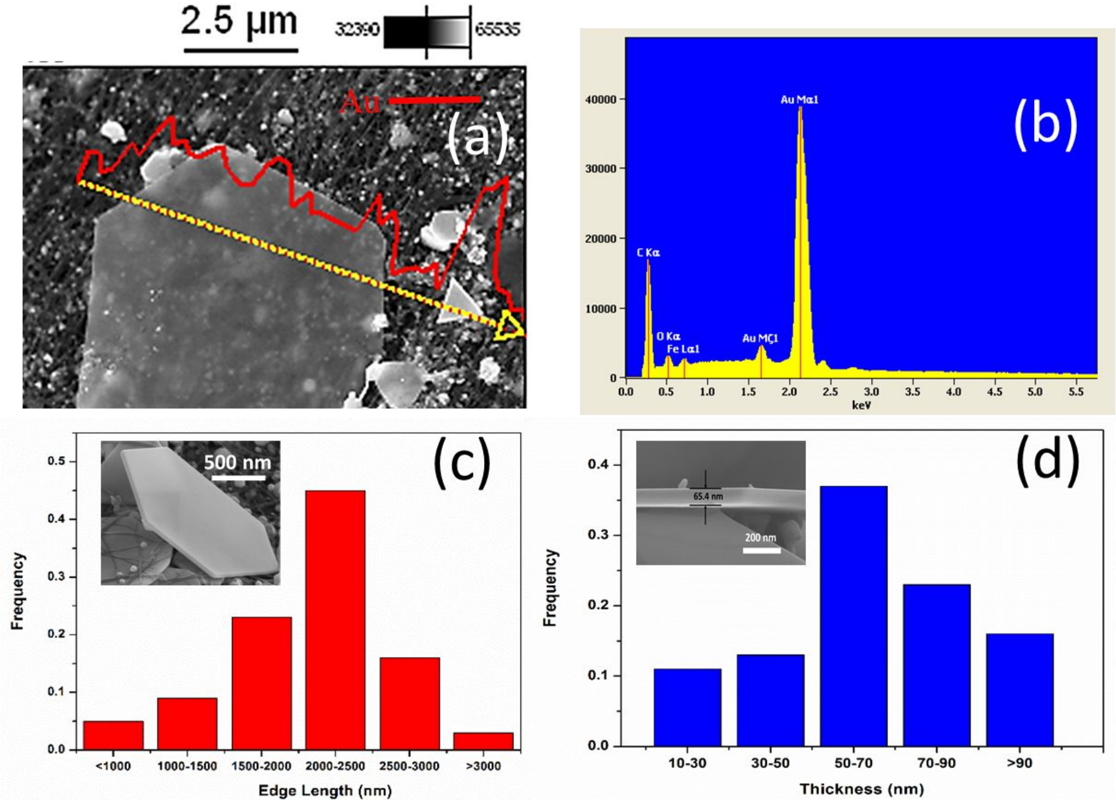

Figure 3.2 Elemental and size analysis of AuNPLs. (a) Au element line scanning on two AuNPLs. (b) EDX spectrum of areas shown in (c) statistical analysis of edge length from 80 AuNPLs and (d) statistical analysis of thickness from 50 AuNPLs.

graphene and (2) a number of Au nanoparticles with random orientations as of the by-products were synthesized associating with AuNPLs, which was consistent with the illustration from SEM images in Figure 3.2.

We further carried out transmission electron microscopy (TEM) experiment for the purpose of studying AuNPLs structures in details. Fig. 3.3(b) shows a typical TEM image of a hexgonal AuNPL on CNT network surface. It is interesting to note surface wrinkles on the Au sheet due to the bending of the flat and thin sheet. The corresponding selected area electron diffraction pattern (SAED) of AuNPL was obtained with incident electron beam normal to the plate surface and the pattern was shown in Fig. 3.3(c). The diffracted spots were well-arranged in hexagonal pattern with a sixfold symmetry, indicative of a typical {111} orientated single crystalline structure, showing a consistency with XRD result. The spots were indexed to {220} and 1/3 {422} Bragg reflections where the presence of forbidden 1/3 {422} diffraction was of particular interest. Many researchers have observed such anomalous phenomena in the plate-like Au[28] and Ag[29] crystals and a number of models have been sketched to explain it, among which stacking faults parallel to (111) plane resulting in the occurrence of 1/3 (422) diffraction was widely accepted.[29] Thus, it is reasonable to speculate that structure of AuNPLs in this report was not perfect which might contain defects as staking faults across {111} planes.

As emphasized in the aforementioned discussions, Br- ions serving as the capping agent played a critical role in promoting the formation of plate-like two dimensional Au sheets. In order to better understand the specific function of Br^- ions

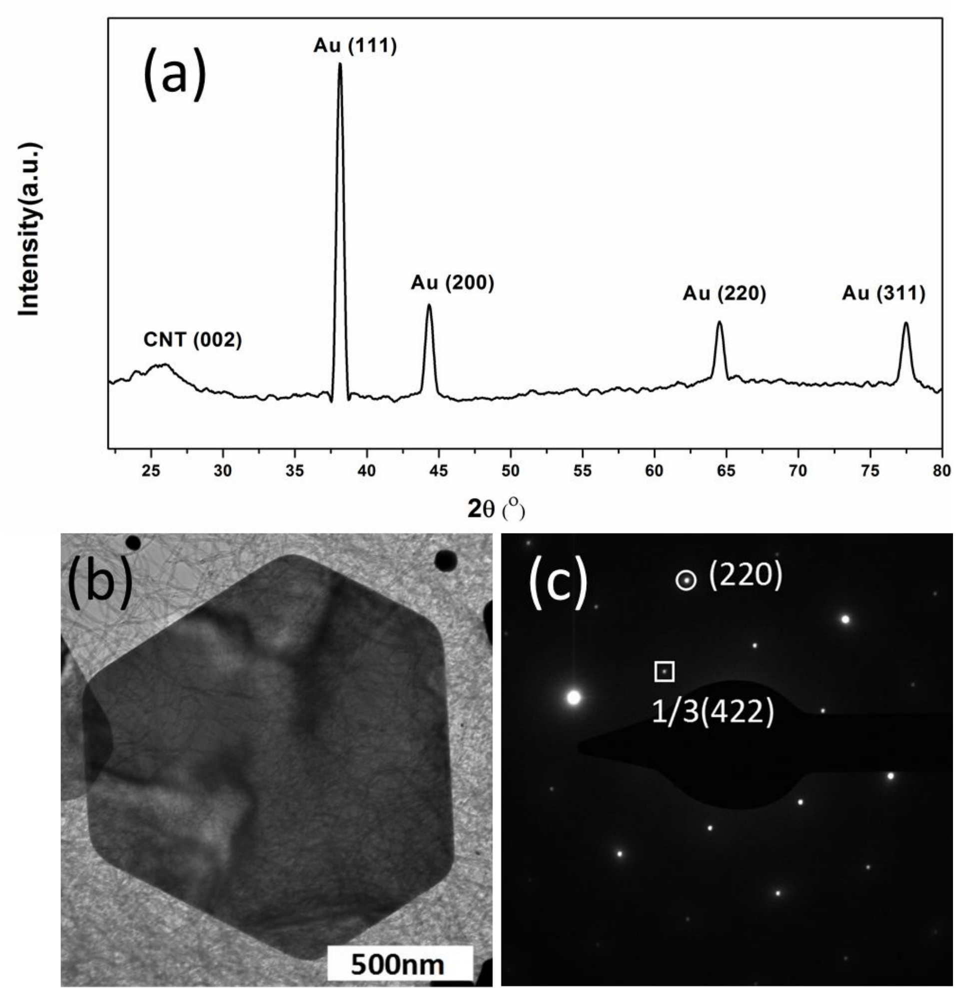

Figure 3.3 Structure characterization of AuNPLs synthesized CNT sheet (a) XRD spectrum of CNT sheet-AuNPLs hybrid. (b) TEM image of a representative AuNPL on CNT network and (c) its corresponding SAED pattern.

in the synthesis of AuNPLs on CNT sheet, a series of experiments were carried out in virtue of varying the concentration of KBr. The obtained SEM images of synthesized CNT sheet-AuNPLs hybrids with 0mg KBr, 15 mg KBr, 40mg KBr and 80 mg 25 mM KBr solution were exhibited in Fig. 3.4 (a)-(d) respectively. In the solution free of KBr, as-produced Au nanocrystals on CNT network were mostly spherical particles. The common morphology of sphere-like Au nanoparticles anchoring on CNT support has been broadly reported by other authors[26,30,31] due to the fact that isotropic growth of Au crystals is thermodynamically favored in the environment lacking of capping agents.32 However, the addition of KBr in the solution, even with low concentration, i.e. 15 mg, led to the presence of AuNPLs notwithstanding, a majority of Au nanoparticles was synthesized as shown in Fig. 3.4(b). Upon a gradual increase of KBr, not only the portion of Au nanoplates over Au nanoparticles but also the size of AuNPLs was eventually enhanced.

This tendency was well identified in Fig. 3.4(c) and (d), suggesting the capping agent used in this report, namely Br- ions was of fundamental importance in inducing the anisotropic growth of AuNPLs on CNT substrate. The phenomena that Br- ions favoring the growth of plate-like Au nanocrystals via hydrothermal reaction was observed previously,[33,34] however, the precise growth mechanism was till elusive. According to the observation in Fig. 3.4, it is reasonable to propose free Br^- ions preferentially absorbed to Au {111} faces, protected Au {111} facets, and subsequently led to a slower growth along <111> direction. Finally, Au nanoplates bounded with multiple {111} planes were produced.

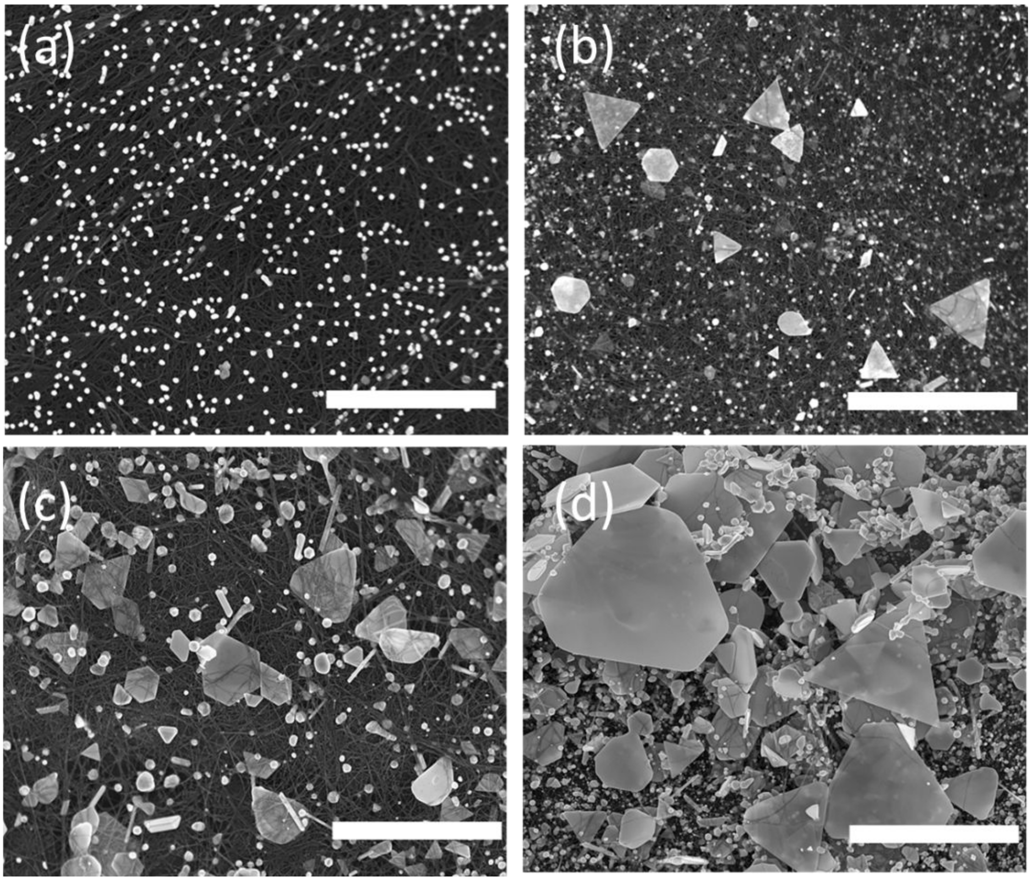

Figure 3.4 SEM images of Au nanocrystals synthesized on CNT sheet with a variety of amount of KBr at 25 mM (a) 0 mg (b) 15 mg (c) 40 mg and (d) 80 mg. Scale bar: 5μm.

Raman scattering responses of the CNT sheet decorated with AuNPLs (sufficient KBr in Fig. 3.4(d)) were recorded and analyzed compared to the pristine CNT sheet and the CNT sheets impregnated with Au nanoparticles (AuNPs) (free of KBr in Fig. 3.4(a)) prior to dispersing any chemical analyte. The corresponding Raman spectra were illustrated in Fig 3.5(a). Two distinct Raman peaks were recorded for all three samples. The peak at approximately 1310 com^{-1} corresponding to D band identified the disorders of CNTs that was usually attributed to amorphous carbon and defects in CNTs. The second peak locating at around 1583 com^{-1} known as G band characterized the crystallinity of graphitic CNTs due to in-plane tangential vibration of carbon-carbon bonds.[31] On the other hand, striking differences in Raman signal intensities were detected in three samples. Compared to bare CNT sheet, both CNT sheet-AuNPs and CNT sheet-AuNPLs displayed more intense Raman signals. Here we employed the relative intensity of G band of pristine CNT sheet as enhancement factor (EF). Accordingly, the EFs of CNT sheet-AuNPs and CNT sheet-AuNPLs were calculated as 2.0 and 2.2, respectively, indicating that Raman scattering enhancement of CNT sheet substrate with AuNPLs is comparable with that with AuNPs.

According to the results in Fig. 3.5(a), the mechanisms of Raman scattering enhancement from both AuNPLs and AuNPs were schematically elaborated in Fig. 3.5(b). Since their EFs are very close, we suggest AuNPLs and AuNPs deposition owned the identical mechanisms for Raman enhancement including both electromagnetic mechanism(EM, yellow arrow) and chemical mechanism(CM, red

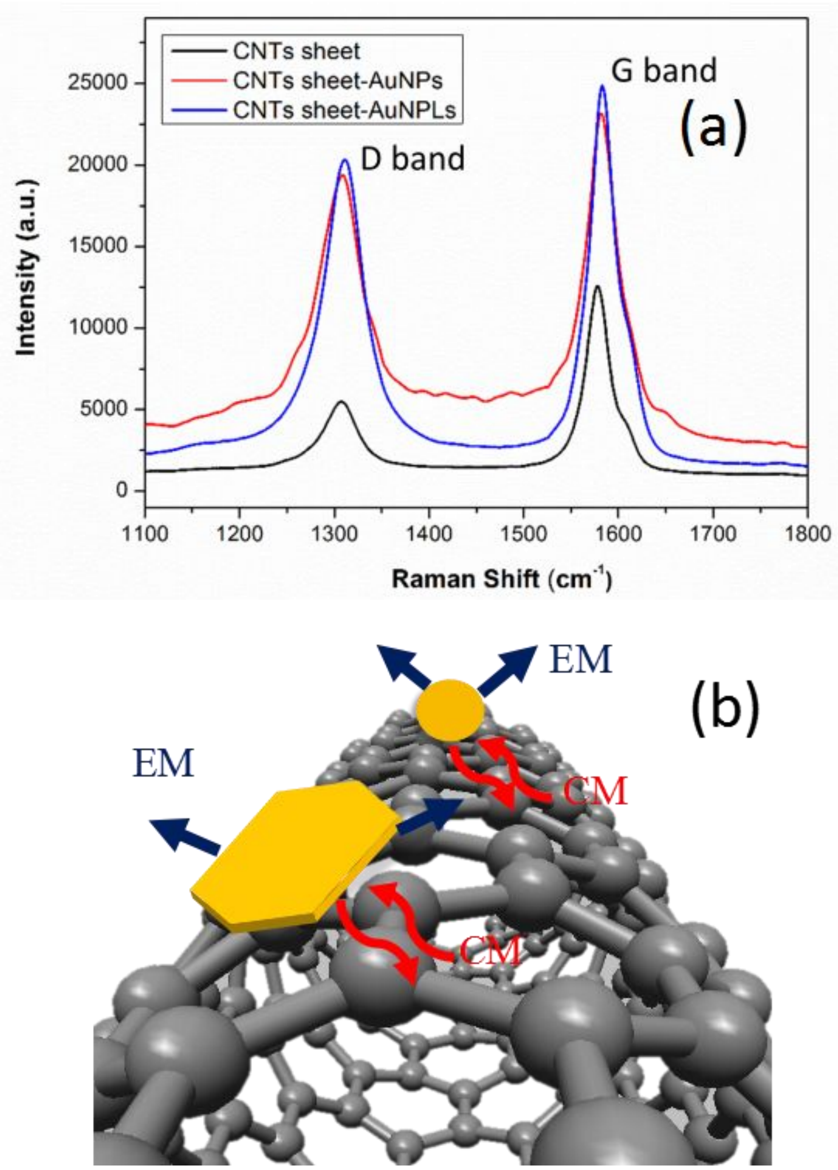

Figure 3.5 Raman responses from Au nanocrystals decoration on CNT sheet. (a) Raman spectra of CNT sheet, CNT sheet-Au nanoparticels (AuNPs) and CNT sheet-AuNPLs and (b) the corresponding mechanisms for Raman enhancement. Yellow arrow represents electromagnetic mechanism and red arrow indicates chemical interaction.

arrow).[4,25,31,35] In particular, it has been experimentally proved that Raman signals of CNT network can be enhanced by many folders due to the decorations of metallic nanostructures and the enhancement originates from EM, i.e. localized electric field enhancement from the localized surface plasmon resonance (LSPR) of metallic nanostructures as well as CM, i.e. charge-transfer complex formed by graphitic layers and metallic nanostructures.[31,35] Compared to the reported EFs somewhere else, EFs obtained in this report, that is to say, 2.0 and 2.2 were normally one order of magnitude lower possibly due to rather less dense Au nanocrystals loading on CNT scaffold, leading to larger inter-particle gaps. In general, the gaps between two neighbor particles smaller than 10 nm are highly beneficial for significant enhancement of Raman signals[35] whereas the inter-particle distances in our report were more than 100 nm measured from Fig. 3.4(a).

The photo in Fig. 3.6(a) illustrate of the excellent flexibility of the CNT sheet. It is interesting to note that the substrate can be not only bent freely but also wrapped onto a mini-cylinder easily, which potentially allows it to meet special position requirements as novel SERS substrate. A diagram in Fig. 3.6(b) schematically presents the route how to probe the analyte on CNT sheet-AuNPLs substrate. To validate the SERS efficiency and sensitivity of CNT sheet-AuNPLs substrate, we prepared a variety of concentrations of Rh6G, a highly fluorescent dye widely used as SERS analyte on the substrate. The measured SERS spectra are shown in Fig. 3.6(c)

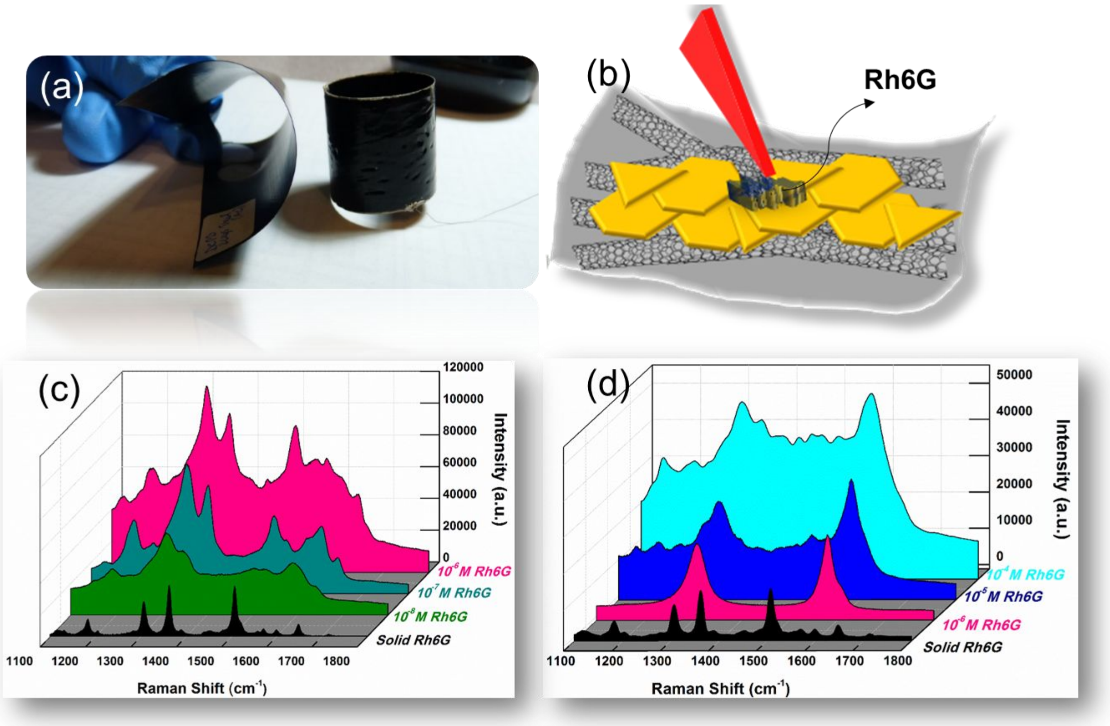

Figure 3.6 Performance of CNT sheet-AuNPLs hybrid utilized as flexible SERS substrate (a) photo of flexible CNT sheet (b) schematic diagram of probing analyte Rh6G on CNT sheet-AuNPLs (c) SERS performance of CNT sheet-AuNPLs substrate for detection of Rh6G from 10^{-6} to 10^{-8} M and (d) SERS performance of CNT sheet-AuNPs substrate for detection of Rh6G 10^{-4} to 10^{-6} M.

where Raman spectrum of solid Rh6G is displayed as the reference. Five characteristic Raman peaks of Rh6G found at approximately 1182, 1306, 1362, 1506, and 1647 cm^{-1} were assigned to stretchingmodes of aromatic benzene rings.[36] All the representative peaks of Rh6G were dramatically enhanced and could be distinctly identified at the concentrations of 10^{-6} M and 10^{-7} M when the hybrid of CNT sheet-AuNPLs was utilized as the substrate. The Raman intensity showed a gradual decrease with lowering the analyte concentration. When the amount of Rh6G reached to 10^{-8} M, the detection sensitivity became poor where the signatures at 1362, 1506 and 1647 com^{-1} could be hardly justified. Thus, we conclude the as-fabricated novel flexible SERS substrate showed high sensitivity which was capable of probing the Rh6G at the concentration as low as 10^{-7} M.

In order to better demonstrate the advantages of CNT sheet-AuNPLs platform, we further tested the SERS performance of CNT sheet coupling with Au nanoparticles(short for AuNPs), that is, synthesized without capping agent and the corresponding spectra are shown in Fig. 3.6(d). In contrast to the excellent performance of CNT sheet-AuNPLs, it showed a much poorer sensitivity. Although five peaks of Rh6G at 10^{-4} M could be detected, the band at 1647 cm^{-1} was scarcely differentiated from the shoulder of CNT G-band. Furthermore, the main peaks at 1362 and 1647 cm^{-1} almost disappeared when the analyte concentration reduced to 10^{-5} M and eventually it lost all the signatures of the analyte at 10^{-6} M where the spectrum was identical to that of bare CNT sheet-AuNPs that was free of the analyte shown in Fig. 3.5(a).

Such large difference in SERS performance of the two substrates is unlikely due to CNT sheet because we observed nearly the same Raman responses with both bare substrates before analyte adsorption shown in Fig. 3.5(a). Thus, it is highly suggestive that low sensitivity of CNT sheet-AuNPs subtrate was attributed to the sparsely distributed Au nanoparticles on the CNT support, as explained above, leading to large interparticle gaps which limited localized E-filed enhancement. Moreover, it has been proposed molecules absorbed on spherical plasmonic particles were randomly orientated in the nanoscale valley of adjacent particles which might impede the SERS sensitivity and uniformity.[11] Hence, sufficiently heavy loads of plasmonic nanoparticles anchoring on CNT network are of necessity to build highly sensitive SERS substrate.[24,25,31,35] Such requirement will not only give rise to challenges for fabrication but also issues in view of cost. As an alternative, AuNPLs with much larger surface areas than that of Au nanoparticles, provided more abundant plasmonic sites when the analyte deposited on their surface. When the assembly of monolayer Au triangular plates was employed as SERS substrate, it was able to detect the analyte crystal violet (CV) at the concentration as low as 10^{-8} M which proved the high SERS sensitivity of Au nanoplates.[27] Besides of large dimensions, sharp edges of AuNPLs could serve as additional “hot spots” to enhance the coupling effect of electromagnetic field, contributing to the extra sensitivity of SERS performance.[37,38] Therefore, it is understandable that CNT sheet-AuNPLs as flexible SERS substrate showed much higher sensitivity than that of CNT sheet-AuNPs platform with regard to the same quality of gold precursor utilized within the two substrates.

3.4 Conclusions

In summary, we reported a simple one-pot method to synthesize large-scale AuNPLs on CNT sheet in the solution where Br^- ions serving as capping agent. We demonstrated Br^- ions would facilitate the anisotropic growth of AuNPLs. The final products still contained a portion of irragular Au nanoparticles other than well-defined AuNPLs, which requires further improvement in future research. However, the synthesized AuNPLs showed single-crystalline FCC structure with the edge up to 3 μm, providing large surface areas of particular benefit for SERS performance. Accordingly, we detected Rh6G with very low concentration (10^{-7} M) by using such flexible CNT sheet-AuNPLs platform via SERS strategy, showing huge advantages in contrast to Au nanoparticles decorated CNT sheet. By means of incorporating AuNPLs with commercially available CNT sheet, such novel flexible SERS substrate owns great potential for scale-up fabrication in future.

3.5 References

1. S. Nie and S. R. Emory, *Science*, 1997, **275**, 1102-1106
2. M. P. Cecchini, V. A. Turek, J. Paget, A. A. Kornyshev and J. B. Edel, *Nat. Mater.*, 2012, **12**, 165–171
3. E. C. L. Ru, E. Blackie, M. Meyer and P. G. Etchegoin, *J. Phys. Chem. C*, 2007, **111**, 13794–13803
4. B. Sharma, R. R. Frontiera, A.-I. Henry, E. Ringe and R. P. Van Duyne, *Mater. Today*, 2012, **15**, 16–25
5. L. Polavarapu and L. M. Liz-Marzán, *Phys. Chem. Chem. Phys.*, 2013, **15**, 5288-5300
6. C. H. Lee, L. Tian and S. Singamaneni, *ACS Appl. Mater. Interfaces*, 2010, **2**, 3429-3435
7. K. D. Osberg, M. Rycenga, G. R. Bourret, K. A. Brown and C. A. Mirkin, *Adv. Mater.*, 2012, **24**, 6065-6070
8. L. Polavarapu, A. L. Porta, S. M. Novikov, M. Coronado-Puchau and L. M. Liz-Marzán, *Small*, 2014, **10**, 3065–3071
9. L.-B. Zhong, J. Yin, Y.-M. Zheng, Q. Liu, X.-X. Cheng and F.-H. Luo, *Anal. Chem.*, 2014, **86**, 6262-6267
10. C.-L. Zhang, K.-P. Lv, H.-P. Cong and S.-H. Yu, *Small*, 2012, **8**, 648-653
11. W. G. Xu, X. Ling, J. Q. Xiao, M. S. Dresselhaus, J. Kong, H. X. Xu, Z. F. Liu and J. Zhang, *Proc. Natl. Acad. Sci. U. S. A.*, 2012, **109**, 9281–9286
12. W. G. Xu, N. N. Mao and J. Zhang, *Small*, 2013, **9**, 1206–1224

13. X. Ling, L. M. Xie, Y. Fang, H. Xu, H. L. Zhang, J. Kong, M. S. Dresselhaus, J. Zhang and Z. F. Liu, *Nano Lett.*, 2010, **10**, 553-561

14. M. S. Purewal, B. H. Hong, A. Ravi, B. Chandra, J. Hone and P. Kim, *Phys. Rev. Lett.*, 2007, **98**, 186808

15. M. F. L. De Volder, S. H. Tawfick, R. H. Baughman and A. J. Hart, *Science*, 2013, **339**, 535–539

16. B. Peng, M. Locascio, P. Zapol, S. Li, S. L. Mielke, G. C. Schatz and H. D. Espinosa, *Nat. Nanotechnol.*, 2008, **3**, 626-631

17. D. Zhang, K. Ryu, X. Liu, E. Polikarpov, J. Ly, M. E. Tompson and C. Zhou, *Nano Lett.*, 2006, **6**, 1880–1886

18. I. Jeon, K. Cui, T. Chiba, A. Anisimov, A. G. Nasibulin, E. I. Kauppinen, S. Maruyama and Y. Matsuo, *J. Am. Chem. Soc.* 2015, **137**, 7982−7985

19. M.-Q. Zhao, C. E. Ren, Z. Ling, M. R. Lukatskaya, C. Zhang, K. L. Van Aken, M. W. Barsoum and Y. Gogotsi, *Adv. Mater.*, 2015, **27**, 339–345

20. N. Behabtu, C. C. Young, D. E. Tsentalovich, O. Kleinerman, X. Wang, A. W. K. Ma, E. A. Bengio, R. F. ter Waarbeek, J. J. de Jong, R. E. Hoogerwerf, S. B. Fairchild, J. B. Ferguson, B. Maruyama, J. Kono, Y. Talmon, Y. Cohen, M. J. Otto and M. Pasquali, *Science*, 2013, **339**, 182

21. A. Lekawa-Raus, J. Patmore, L. Kurzepa, J. Bulmer and K. Koziol, *Adv. Funct. Mater.*, 2014, **24**, 3661-3682

22. W. Xu, Y. Chen, H. Zhan and J. N. Wang, *Nano Lett.*, 2016, **16**, 946-952

23. P. Jarosz, C. Schauerman, J. Alvarenga, B. Moses, T. Mastrangelo, R. Raffaelle, R. Ridgley and B. Landi, *Nanoscale*, 2011, **3**, 4542–4553

24. K. Zhang, J. Ji, X. Fang, L. Yan and B. Liu, *Analyst*, 2015, **140**, 134–139

25. Y. Sun, K. Liu, J. Miao, Z. Wang, B. Tian, L. Zhang, Q. Li, S. Fan and K. Jiang, *Nano Lett.*, 2010, **10**, 1747–1753

26. X. J. Wang, C. Wang, L. Cheng, S. T. Lee and Z. Liu, *J. Am. Chem. Soc.*, 2012, **134**, 7414–7422

27. L. Scarabelli, M. Coronado-Puchau, J. J. Giner-Casares, J. Langer and L. M. Liz-Marzán, *ACS Nano*, 2014, **8**, 5833-5842

28. H. L. Qin, D. Wang, Z. L. Huang, D. M. Wu, Z. C. Zeng, B. Ren, K. Xu and J. Jin, *J. Am. Chem. Soc.*, 2013, **135**, 12544–12547

29. J. Li, D. Ingert, Z. L. Wang and M. P. Pileni, *J. Phys. Chem. B*, 2003, **107**(34), 8717-8720

30. H. C. Choi, M. Shim, S. Bangsaruntip and H. Dai, *J. Am. Chem. Soc.*, 2002, **124**, 9058-9059

31. H. Sharma, D. C. Agarwal, A. K. Shukla, D. K. Avasthi and V. D. Vankar, *J. Raman Spectrosc.*, 2013, **44**, 12–20

32. Y. Xia, X. Xia and H.-C. Peng, *J. Am. Chem. Soc.*, 2015, **137**, 7947–7966

33. D. V. R. Kumar, A. A. Kulkarni and B. L. V. Prasad, *Colloids Surf., A*, 2013, **422**, 181–190

34. W. Xin et. al One-step Synthesis of Gold Nanoplates with Tunable Size and Thickness on Multi-layer Graphene Sheets, Manuscript in preparation

35. H. B. Chu, J. Y. Wang, L. Ding, D. N. Yuan, Y. Zhang, J. Liu and Y. Li, *J. Am. Chem. Soc.*, 2009, **131**, 14310-14316

36. S. Shim, C. M. Stuart and R. A. Mathies, *ChemPhysChem*, 2008, **9**, 697–699

37. T. Y. Jeon, S. G. Park, S. Y. Lee, H. C. Jeon and S. M. Yang, *ACS Appl. Mater. Interfaces*, 2013, **5**, 243-248

38. W. Fan, Y. H. Lee, S. Pedireddy, Q. Zhang, T. Liu and X. Y. Ling, *Nanoscale*, 2014, **6**, 4843–4851

Chapter 4 A Novel Method for Synthesis of Gold Nanowires with Ultrahigh Aspect Ratio Encapsulated in Assemblied Carbon Nanotubes and Their Growth Mechanism

Abstract

Filling foreign materials into hollow cores of carbon nanotube (CNT) has attracted growing interest due to the feasibility of creating novel structures with innovative properties. Here, we introduce a novel method for filling gold nanowires (AuNWs) inside assemblied CNTs. By means of oxygen plasma treatment, we efficiently open CNT structures in a short period of 40 s. Raman spectroscopy and high resolution TEM confirm the defects are created on CNT walls with plasma treatment. AuNWs grow inside CNT at a moderately low temperature (~80-90 ^{o}C). The maximum aspect ratio (length/diameter) of obtained AuNWs is as high as ~500 which is the highest ever reported for AuNWs inside CNTs. Detailed characterizations of ultrathin AuNWs show they have single crystalline face-centered cubic (FCC) structure. Experimental results identify plasma treatment and the surfactant potassium bromide (KBr) are key factors in the formation of AuNWs encapsulated in the CNTs. Accordingly, we propose a growth mechanism elucidating the procedures of synthesizing such interesting heterostructure. Finally it presents graphitic shells protected ultrathin AuNWs are highly stable under electron irradiation. Ultrathin AuNWs with twins are more resistant to electron irradiation compared to those wires free of defects.

4.1 Introduction

Carbon nanotubes (CNTs) are broadly considered as ideal candidates for the construction of platforms for innovative devices and architectures from nano- to micro-scale, owing to their remarkable electrical, mechanical, thermal and optical properties.[1] Integration of desirable foreign objects with CNTs by means of filling them into nanotubes opens up a wide range of research for innovative carbon-based systems.[2-5] Of particular interest is filling up the hollow channel of CNTs with various metals, giving rise to novel hybrid nanostructures which present attractive and interesting applications in the fields of emerging nanotechnologies. For instance, a nano-thermometer has been built by encapsulating gallium inside a CNT, which shows the capability to probe temperatures widely ranging from 50 to 500 ^{o}C.[6] Additionally, multi-wallled CNT serving as a nanoextruder can deform and extrude nanometer-scaled wires encapsulated in the tube core, providing a perfect template for investigating structures and properties of ultrathin nanocrystals under high pressure.[7]

Ultrathin gold nanowires (AuNWs), usually with the diameter less than 10 nm have attracted intensive research attention recently due to their unique properties, ultra-high aspect ratio, excellent mechanical and electronic properties and so forth,[8-10] in contrast to other gold nanocrystals like nanoparticles and nanorods. A number of novel applications have been reported by utilizing their exceptional properties. As an example, a superior wearable pressure sensor with high sensitivity has been constructed based on long ultrathin AuNWs-impregnated tissue paper.[11] On the other hand, carbon nanotubes, especially single-walled CNTs (SWNTs) and few-walled

CNTs normally have diameters narrower than 5 nm, which provide ideal channels to encapsulate ultrathin AuNWs. The investigation of hybrid heterostructures of ultrathin AuNWs inside such narrow CNTs, denoted AuNWs @CNTs is of fundamental importance to understand the crystal growth and deformation of AuNWs as well as the carbon-gold interactions at atomic scale and hence apply the merits of such novel nanocomposite to the true environment.[12] Moreover, the incorporation of ultrathin AuNWs inside the cavity of CNTs may modify the physical properties of both encapsulating tubes and encapsulated wires, potentially bringing in new functional materials from nanoscale (individual CNTs) to marcoscale (CNTs assemblies). Indeed, it has been predicted that a higher melting point was obtained for nanowires inside CNTs compared to that of exposed nanowires indicating the graphitic sheath of CNTs enhances the thermal stability of the encapsulated nanowires.[13]

To date, however, the synthesis of ultrathin AuNWs with high aspect ratio (>100) inside the tubular graphitic core (sub-5 nm) has been rarely revealed due to significant degradation of the capillarity of narrow nanotubes compared to CNTs with a large diameter.[14,15] This indicates the traditional filling method, namely melting-phase capillary filling is unsuitable for growing long AuNWs within sub-5 nm CNTs. Previous report shows the maximum length of AuNWs is only 70 nm inside SWNTs with diameter 1.0-1.4 nm in virtue of molten phase filling, indicative of a aspect ratio no more than 70.[14] Moreover, limitations of the conventional methods imply that it predominately relies on high vacuum and high temperature that is usually 100 K higher than the melting point of the metal precursors, which make the fabrication process rather complicated.[5,16,17] Additionally, it has been well established that opening up the nanotubes structure either through end caps or through side walls is the necessity prior to the filling process, which conventionally employ strong acids to oxidize the nanotubes and create the defective sites (holes and voids, etc.) on CNT skeleton where the foreign materials start to fill in.[18,19] Such wet process for oxidization is substantially time-consuming, difficult to control and environmental unfriendly, hindering the feasibility of scale-up production. Despite the process improvement has been recently made by Lin et. al with the adoption of a pre-aligned and open-ended porous CNTs membrane, the aspect ratio of obtained AuNWs was only 20 due to relatively large diameters of CNTs (~15 nm).[15]

Here, we have developed innovative fabrication strategies for both opening and filling procedures and revealed ultrathin AuNWs with high aspect ratio as large as 500 inside CNTs. By means of atmospheric oxygen plasma, we efficiently create defects on CNT walls within 60 s yet sufficiently allowing AuNWs filled in. Few-walled walled CNT yarn is selected here due to the comparable diameters of CNT to ultrathin AuNWs, i.e. less than 5 nm and the marco-form of assemblied CNTs of particular importance for large-scale applications. Furthermore, a novel filling-in procedure at a moderate low temperature (~85 ^{o}C) relying on large diffusivity of Au on graphitic surfaces is presented in this report, which is distinct from the conventional filling means largely dependent of the capillarity of nanotubes. The encapsulated AuNWs are single-crystalline with face centered cubic (FCC) structure which can be as long as 1.5 μm with ultrathin diameter of 2.4 nm.

4.2 Experimental

4.2.1 Chemicals and Materials

High-tex CNTs yarn (HTY) was acquired from Nanocomp Technologies Inc. (Merrimack, NH), which was fabricated by a continues chemical vapor deposition (CVD) process. Nanotubes grown with iron catalysts in the CVD furnace was subsequently collected onto a drum with a rotating velocity of ~15m/min to impart alignment in the drawing direction. Thus, CNTs assembly used in this work are virtually scale-up production. The width of received HTY varied from 0.8 mm to 1.2 mm whereas the thickness of the yarns ranged from 10 μm to 20 μm. Gold chloride hydrate ($HAuCl_4 \cdot xH_2O$, 99.999%) and potassium bromide (KBr, ACS reagent, >99.0%) was purchased from Sigma-Aldrich, USA.

4.2.2 Opening CNT via plasma treatment

In this work, we utilized an Atomflo™ plasma system from Surfx® Technologies LLC for plasma treatment in order to open up the walls of CNTs.[20] When the system was fed with primary gas (helium, industrial grade, 99.995%) and secondary gas (oxygen, ultrahigh purity, 99.999%), oxygen plasma was generated associated with 150 W applied power. The feeding rate of helium and oxygen were 30 L/min and 0.5 L/min respectively. CNTs yarn was cut into segments with certain length (~15–20 cm) and then taped the ends onto a rigid substrate prior to the plasma treatment. The plasma head was adjusted to a 5.0 mm working distance from the surface of samples with a built XYZ robot from Surfx® Technologies LLC. Plasma device scanning from one end of the sample to the other was accounted as one scan. With the scan rate of 20 mm/s, totally 40 scans were applied to the samples, indicating with treatment time was ~40 seconds. The plasma design was schematic shown in Fig. 4.1(a).

4.2.3 Filling AuNWs into CNTs yarn

To grow AuNWs inside of the cores of CNTs, 8 cm segment of plasma treated CNTs yarn was immersed into a glass vial that contained 18 ml DI water, 45 mg $HAuCl_4$ (28.5 mM) and 0.25 ml KBr (80 mM). The mixture was maintained at 85 ^{o}C for 16 hours which was sufficiently long for complete redox reaction and gold diffusion. Subsequently, CNTs yarn was taken out from the solution and washed with DI water thoroughly. CNTs yarn was finally dried in the vacuum oven at 100 ^{o}C for 4 hours. The filling in procedure design was schematically illustrated in Fig. 4.1(b).

4.2.4 Characterizations

Scanning electron microscopy (SEM) and transmission electron microscopy (TEM) studies were carried out in order to understand the morphologies and structures of control HTY and the plasma treated HTY. SEM analysis was obtained with FEI Nova NanoSEM 230. To prepare samples for scanning electron microscopy (SEM), the CNTs yarn was cut into small pieces with the size matching to SEM holder and then taped to conductive carbon tape on SEM holder. High resolution TEM (HRTEM) images were obtained with FEI Titan S/TEM system with the accelerating voltage at 80 keV and 300 keV. Energy dispersive X-ray (EDX) analysis was obtained with high-angle annular dark-field scanning tunneling electron microscopy (HAADF-STEM/EDX) at 80 kV. TEM samples were prepared by means of scratching

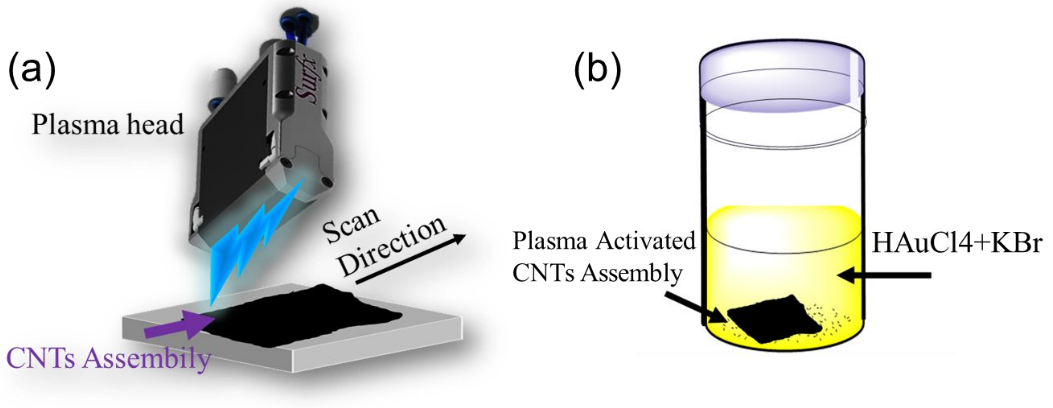

Step 1—Oxygen plasma treatment of CNT yarn

Step 2—Filling in process via wet chemistry

Figure 4.1 Schematic diagram of (a) opening CNT with oxygen plasma and (b) filling AuNWs with wet chemistry treatment.

HTY surfaces with TEM copper grid. CNTs bundles would be peeled off from HTY surfaces and stuck to the grid support. Raman scattering was recorded with a Renishaw In-Via Raman system with the laser length of 785 nm and expose time of 10 s. Five arbitrary spots of the sample were randomly selected and probed with incident laser. The average of five Raman spectra was used to analyze structure variety of CNTs yarn before and after plasma treatment. A Krüss EasyDrop goniometer was employed to obtain the water contact angle (WCA) on HTY. 2 μL water droplet was brought into contact with the yarn surface when making the measurement. The shape of the water droplet was captured by a digital camera and a software program was used to calculate the contact angle.

4.3 Result and Discussion

SEM images of control high tex yarn (HTY) and HTY after 40 scans of plasma treatment are shown in Figure 4.2 (a) through (d). A number of large CNT bundles entangled together and packed densely into knitted mesh with mircoscale pores. A higher magnification image in Fig. 4.2(b) clearly presents the size of a typical CNT bundle (where the arrow points at) is ~100–150 nm, which consisted of approximately 40–50 individual nanotubes. In contrast, CNT mesh displayed a lower packing density after oxygen plasma treatment shown in Fig. 4.2(c). Large CNT bundles were broken down due to the fact that oxygen plasma weakened the van der Waals interactions that held the nanotube bundles together (where the arrow points at in Fig. 4.2(d)).[19] Rather smaller CNT bundles with the diameter ranging from ~10–25 nm and larger pores

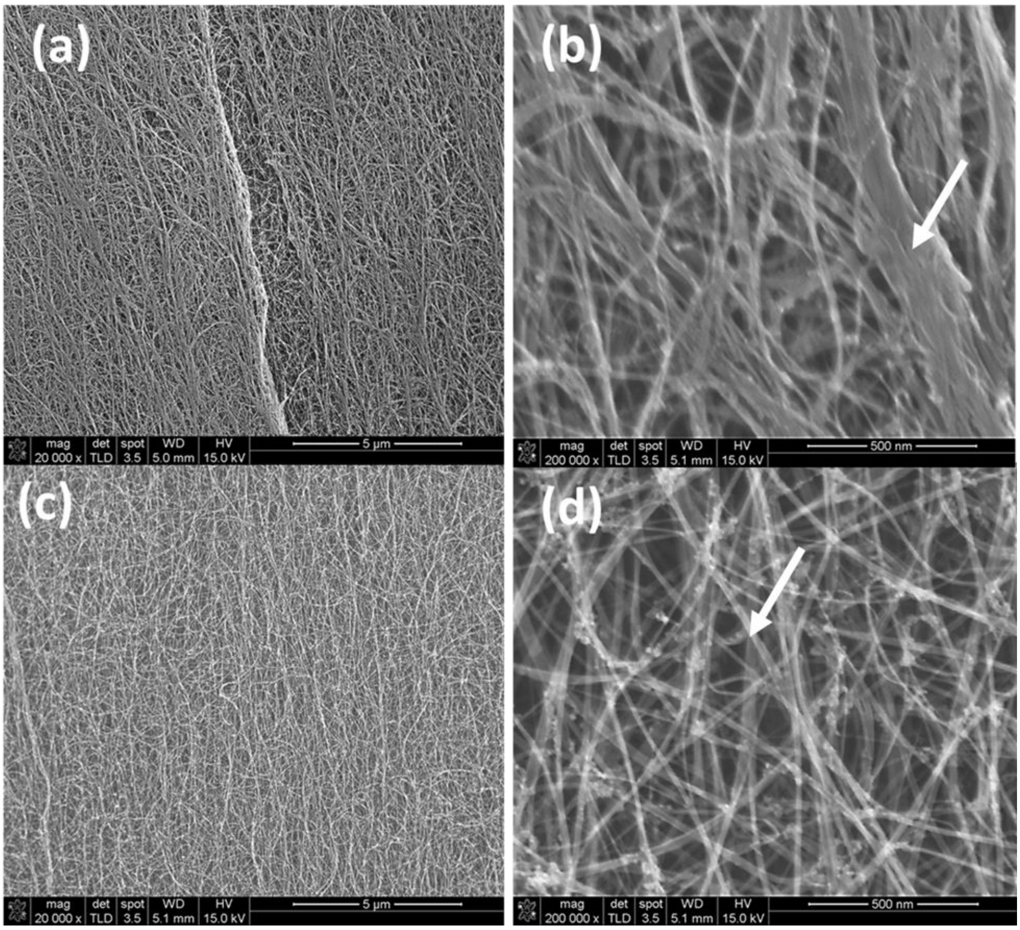

Figure 4.2 Morphologies of CNT yarns before and after plasma treatment (a) and (b) control CNT yarn (c) and (d) plasma treated CNT yarn.

were observed in Fig. 4.2(d) with the magnification 200,000 ×, indicative of an effective way to exfoliate large CNTs bundles. Furthermore, it is worth to note that the overall CNT mesh structure was well preserved without noticeable structure damage at mircoscale. This is distinct from wet-chemistry oxidization of CNTs which usually shortens the nanotube length.[21] Accordingly, the excellent mechanical and electrical properties of CNT yarn might be still maintained after plasma treatment.

In order to investigate detailed structures of control HTY and HTY after plasma treatment, we carried out high resolution TEM experiment. Shown in Fig. 4.3(a) is the low magnification image of control HTY, where CNT bundles were observed consistent with the result from SEM. The black dots were supposed to be iron nanoparticles serving as catalyst during CNT growth. Fig. 4.3(b) presents a high resolution TEM image of a CNT bundle made of 3-4 individual multi-walled CNT (MWNT). The diameters of individual MWNT in the selected bundle were measured from 2.1 nm to 3.4 nm and they usually consisted of 2–5 graphitic walls. Note that large amount of amorphous agglomerates surrounded the CNT bundles (arrow points at in Fig. 4.3(b)) which was a normal consequence of rapid fabrication of CNT assemblies through dry spinning method. Illustrated in Fig. 4.3(b) is a representative HRTEM image of an individual three-walled nanotube with a diameter of approximately 3.9 nm, which was also associated with amorphous carbon on the walls where the arrow points.

After exposed to oxygen plasma for 40 scans, the HTY network became more sparse due to the bundles exfoliation shown in Fig. 4.3(d) compared to the control

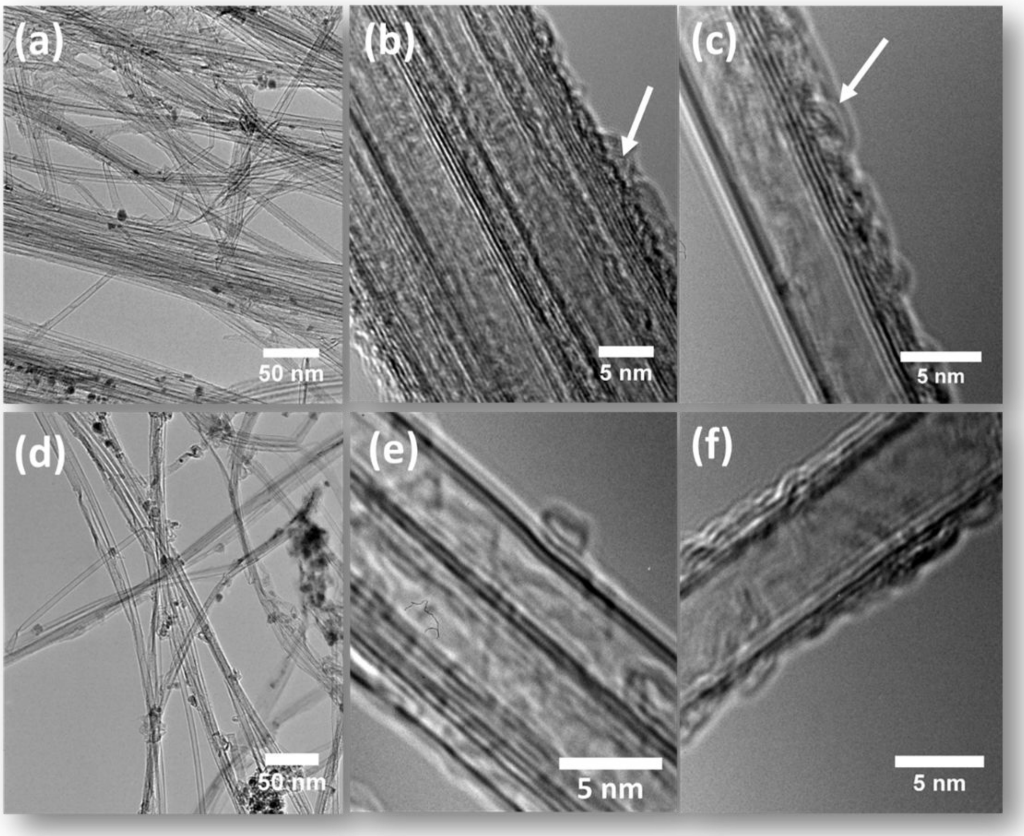

Figure 4.3 High resolution TEM images of CNT yarns (HTY) before (a)-(c) and after (d)-(f) plasma treatment.

HTY. Consistent with SEM observations, the size of CNTs bundles was dramatically reduced. In addition, the amorphous agglomerates seems to be removed or etched by oxygen plasma because CNTs walls in both Fig. 4.3(e) and (f) were better resolved and less amorphous carbon was detected. It also identified no significant alternation of structure integrity such as nanotube shortening or large defects on graphitic layers observed from HRTEM after plasma treatment. However, disorders at atomic scale were created on CNT walls with plasma oxidization shown in Figure 4.4 where the arrows point. In particular, a few carbon atoms were likely knocked out from the walls by the plasma gas, resulting in the voids on graphitic lattice which could potentially provide the space for foreign atoms diffuse in.

Raman spectroscopy is broadly used as a reliable technique to identify crystalline structures and disorders of carbon nanotubes.[21-23] Thus, we further employed Raman measurement of HTY before and after plasma treatment in order to monitor the structure changes. The normalized Raman spectra to G-band intensity are presented in Figure 4.5(a). Two different peaks corresponding to D band at approximately 1308 cm^{-1} and G band at approximately 1580 cm^{-1} are observed for both samples. It is well known that D band identifies the disorders of CNTs that usually originate from the amorphous carbon and structural defects from broken sp^2 bonds, which might lead to vacancies, heptagon-petagon pairs, kinks and so forth.[23] G band characterizes the crystallinity of graphitic CNTs due to in-plane tangential vibration of carbon-carbon bonds.[21] Therefore, relative intensity ratio I_D/I_G can be used to justify the density of

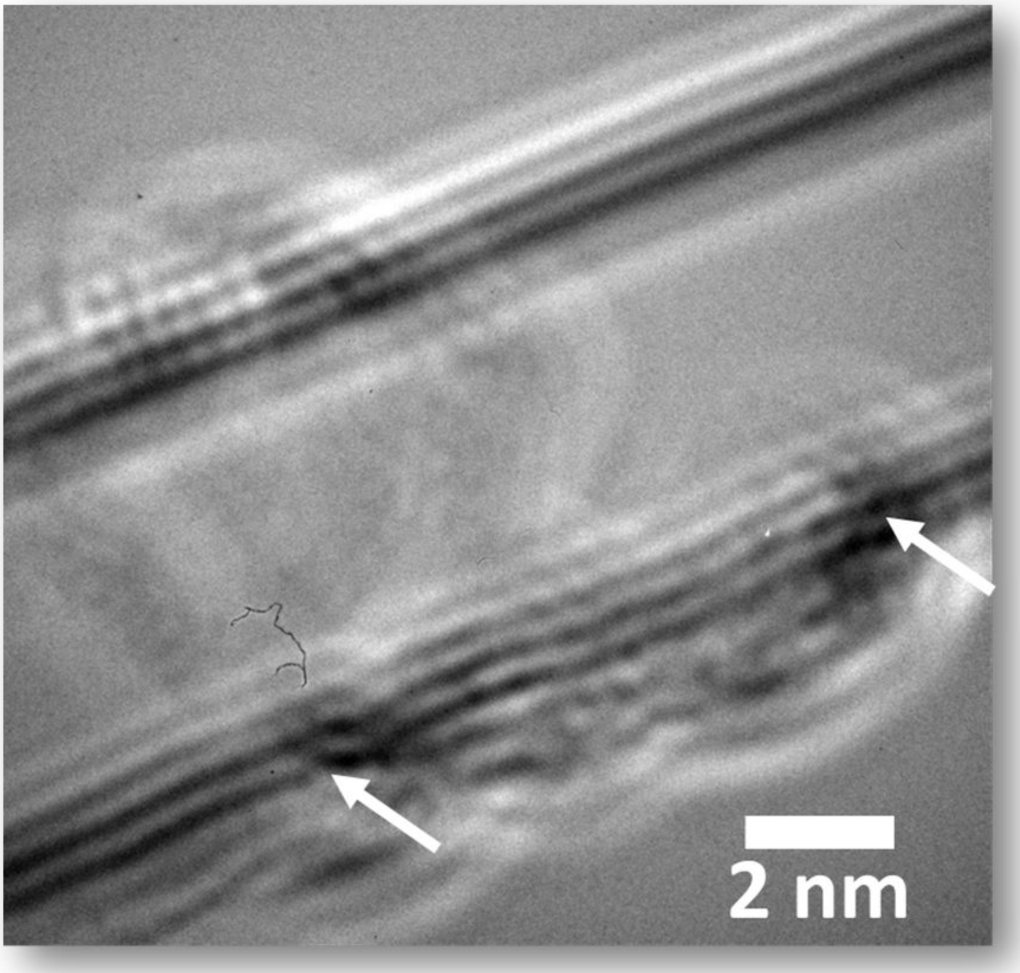

Figure 4.4 High resolution TEM image of a three-walled CNT with defective sites created by plasma treatment.

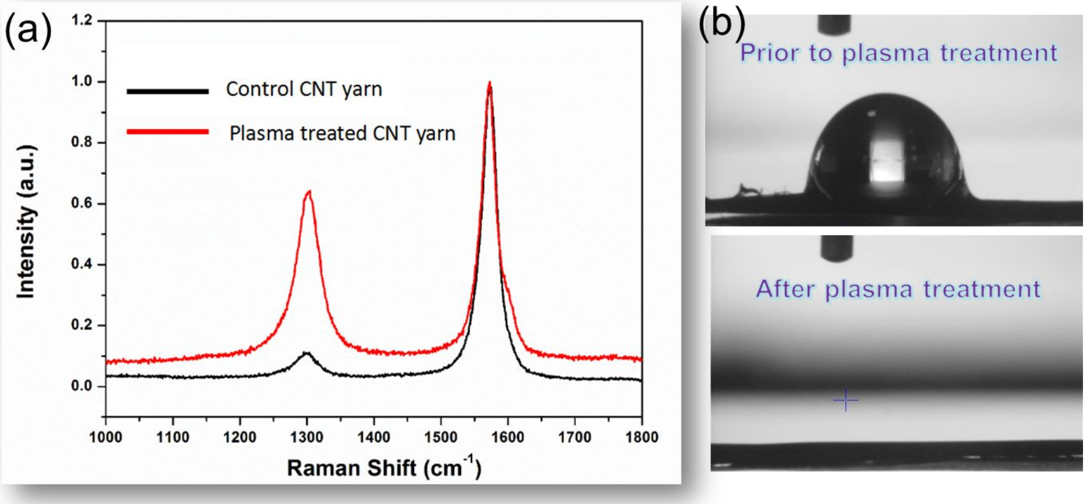

Figure 4.5 (a) Raman spectroscopy of CNT yarns before and after plasma treatment (b) water contact angle test of CNT yarns before and after plasma treatment.

structural defects within the sample. I_D/I_G of control HTY was measured as 0.12 whereas the ratio enhanced significantly to 0.64 after 40 scans of plasma treatment, indicative of a large number of defects were created on HTY surface. Despite we are not able to identify all the types of defects at this moment, the voids from CNTs walls recorded in HRTEM image in Fig. 4.4 is believed to be one type of the defects that contributes to the enhancement of I_D/I_G.

Previous report evidently showed that oxygen plasma treatment led to a convert of carbon atoms to oxidized carbon species such as alcohols carbonyls and carboxylic acids.[20] Such transformation could make carbon nanotube surfaces from hydrophobic to hydrophilic. As a consequence, we recorded the contact angle reduced dramatically from 120^o to less that 5^o when HTY was exposed to plasma with 40 scans presented in Fig. 4.5(b). Note that the oxidized HTY surfaces became superhydrophilic which led to water wet the surfaces so rapidly that the camera was not able to capture any angles more than 5^o. This result confirms that plasma treatment is a simple, fast and efficient method to activate carbon nanotube assemblies.

Shown in Figure 4.6(a) to (d) are the representative TEM images of AuNWs encapsulated in plasma treated CNTs from HTY (AuNWs@HTY). In Fig. 4.6(a), a number of ultrathin AuNWs were observed along with CNTs bundles. It is of particular interest to note that many AuNWs shown here were longer than 300 nm with the diameters normally less than 3 nm. A dense area of AuNWs@HTY was presented in Fig. 4.6(b) where more than 40 % of CNT cores were filled with

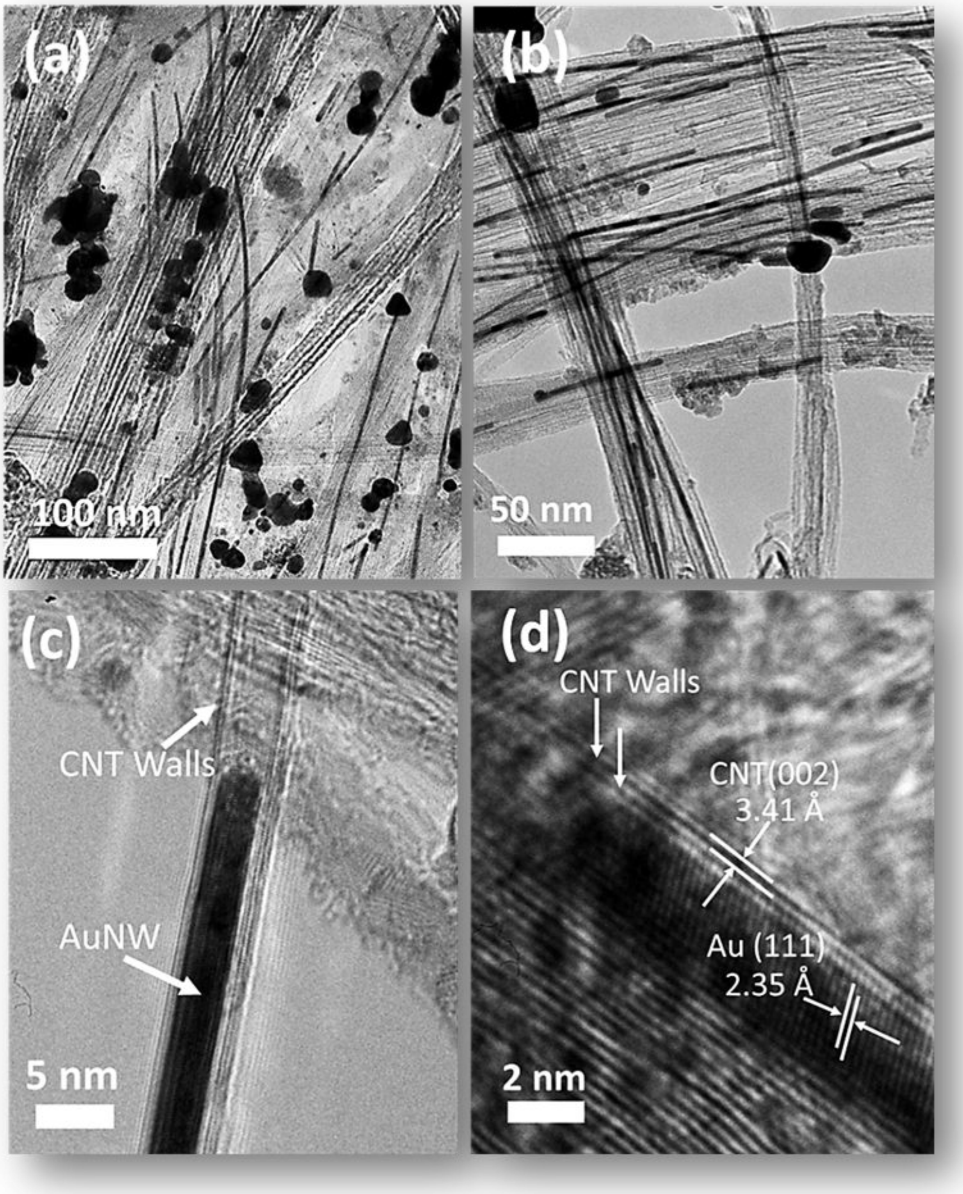

Figure 4.6 Morphologies and structures of AuNWs encapsulated in CNTs (a) low magnification image of AuNWs@HTY (b) a dense area of AuNWs inside CNTs from HTY (c) high magnification image of a selected AuNW filled in CNT and (d) lattice distance of AuNW was measured as 2.35 Å, corresponding to Au {111} plane

AuNWs and it formed a cross-linking network with arbitrary angles associated with the CNTs bundles mesh. It also confirmed a majority of AuNWs had diameters ranging AuNWs distance from 2.0 nm to 3.0 nm due to the uniform diameters of few walled nanotubes that were assembled in to the yarn. Meanwhile, a certain amount of gold nanoparticles anchoring on the CNTs walls were observed. To some reason, the gold nanoparticles residing on CNTs outer shells were not able to grow to gold nanowires.

Higher magnification images in Fig. 4.6(c) illustrate the well-defined structure of a single AuNW encapsulated in the hollow core of CNT. Here graphitic layers of CNT associated with ultrathin AuNW were clearly resolved and the diameter of AuNW was equal to that of inner tube, indicating the nanowire was filled up the tube in the radial direction. In addition, in Fig. 4.6(d) the measured lattice distance of CNTs walls was 3.41Å corresponding to interlayer spacing of G (002).[24] As of AuNW, the measured lattice spacing was 2.35 Å which was perfectly matchable with the distance of Au {111} planes.

In order to determine the elemental information of the hybrid structure, we investigated the elemental mapping of AuNWs@HTY associated with high-angle angular dark field of scanning tunneling electron microscopy (HAADF-STEM). It is interesting to note in Fig. 4.7(a) that the STEM image from dark-field mode showed better contrast of the selected nanowire with CNTs bundle, supporting the one dimensional nanowire with well-defined structure confined within the CNT. The EDX mapping confirmed the nanowire was from gold element while the carbon and oxygen

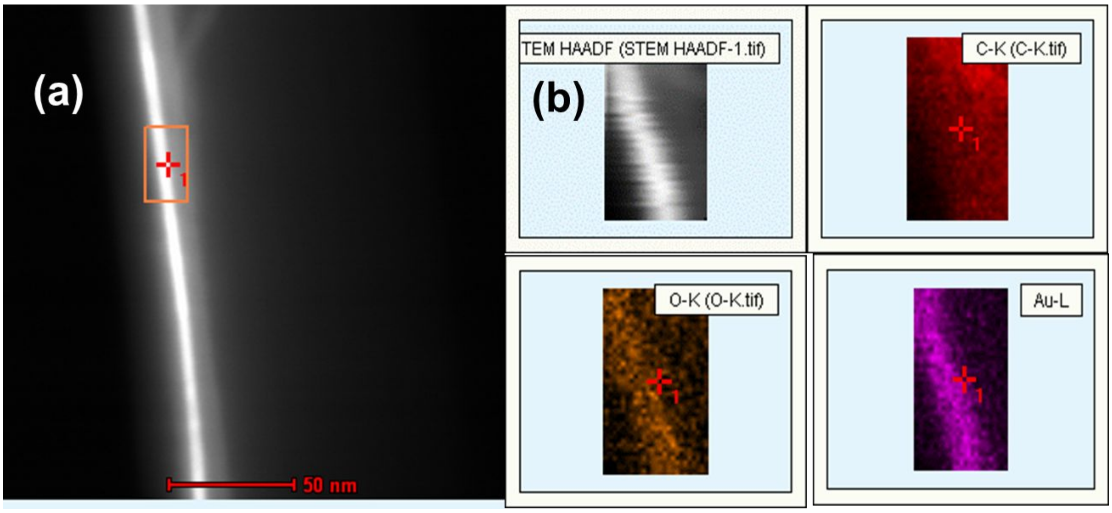

Figure 4.7 EDX analysis of AuNWs@HTY (a) HAADF-STEM image of a selected AuNW inside CNT and (g) its corresponding elemental mapping.

originated from the CNTs bundles as shown in Fig. 4.7(b). No more elements were detected in the selected area suggesting the nanowire was pure gold. Displayed in Fig. 4.8(a) is the AuNW measured with the maximum length as 1400 nm and a diameter approximately 2.8 nm, leading to a largest aspect ratio as 500 in this report. This result is 7-folder higher than the maximum aspect ratio of AuNWs insdie of CNTs previously reported.[14] The statistical distributions of length and diameter of AuNWs are presented in Fig. 4.8(b) and (c). The most frequently observed length of AuNWs was in the range of 300–500 nm while more than 80% of AuNWs had diameters between 2.0 nm and 4.0 nm, resulting in the average aspect ratio as ~150. The diameters of AuNWs inside of CNTs were primarily dependent on the uniform small diameters of individual nanotubes. Such small diameter gave rise to the obtained AuNWs with ultrathin charateristic, similar to the AuNWs synthesized using oleylamine as the capping agent. On the other hand, ultrathin AuNWs was protected by rigid stable graphitic shells in contrast to soft oleylamine and therefore it is reasonable to expect higher stability of AuNWs@HTY than that of conventional synthesized AuNWs. For example, structure of oleylamine capped ultrathin AuNWs degraded rapidly and shredded to nanoparticles and nanorods with the electron irradiation in TEM due to the related thermal heat effect.[25,26]

However, we did not detect any noticeable structure damage of ultrathin AuNWs@HTY with the accelerating voltage at 80 keV. Instead, the structure was highly stable and well resolved at atomic scale as shown in Fig. 4.9(a). The selected AuNW was single crystalline with less than 10-atom-layer thin and the gold atoms

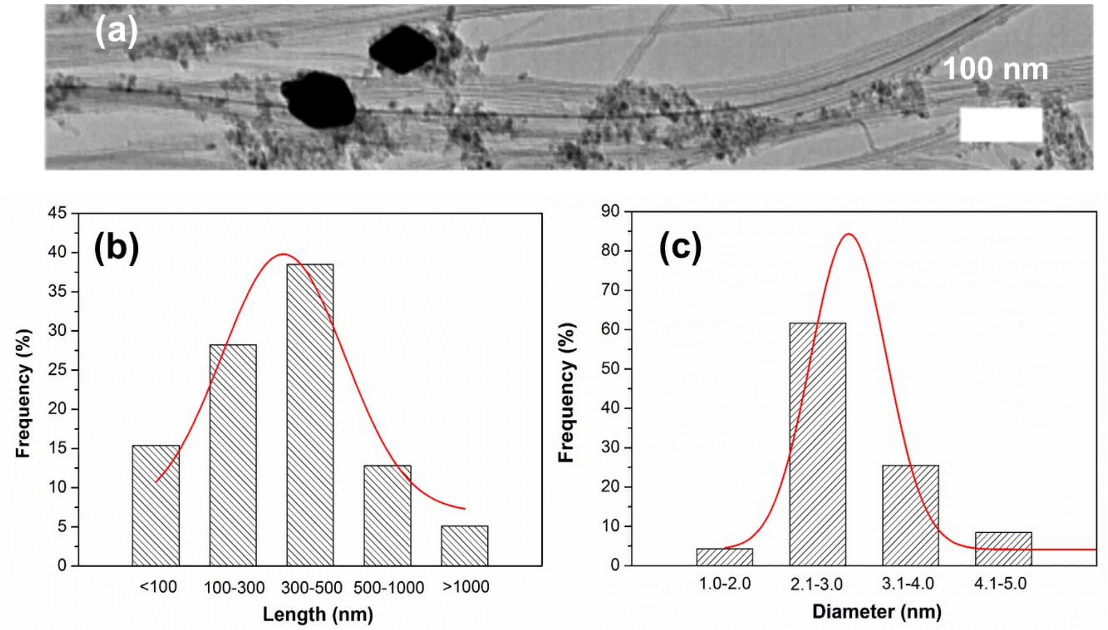

Figure 4.8 (a) TEM image of an ultrathin AuNW with length approximately 1.4 µm and a diameter ~2.8 nm (b) lengths distribution of AuNWs@HTY and (c) diameters distribution of AuNWs@HTY.

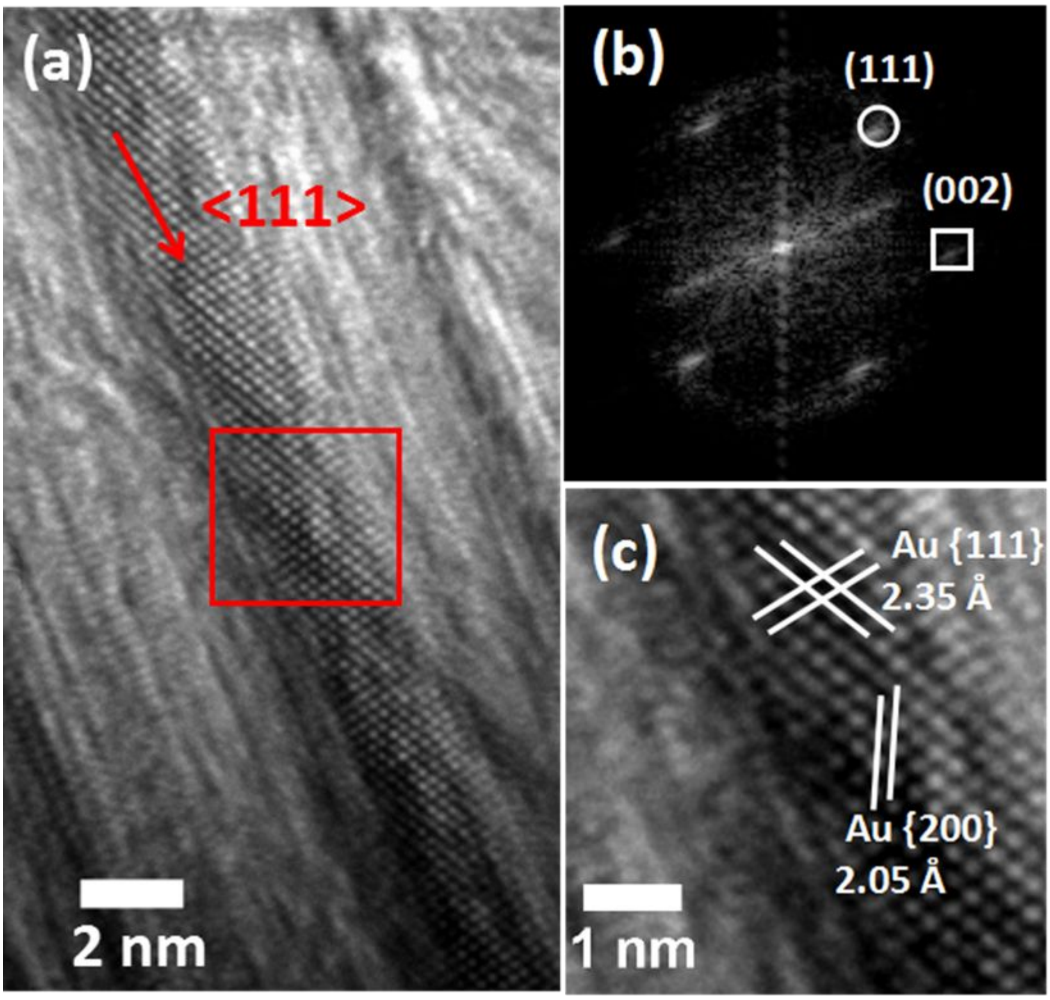

Figure 4.9 Detailed analysis of atomic structures of AuNW inside CNT (a) HRTEM image of an ultrathin AuNW confined in a CNT bundle (b) the corresponding FFT of the area in the red box in (a) and (c) reverse FFT of (b) with measured lattice distances.

were arranged in face-centered cubic (FCC) structure, which was clarified from fast Fourier transformation (FFT) of the chosen area in red box. The FFT spots in Fig. 4.9(b) were index as Au{111} and Au{002}, respectively. The reverse of FFT image was shown in Fig. 9(c) from which the measured lattice distance along their growth direction was 2.35 Å corresponding to the lattice spacing of Au{111} planes, which indicated the growth direction of AuNWs was along <111>. Of particular interest is the defect-free single-crystalline structure of the selected AuNW. No defects like dislocations, stacking faults and twin boundaries were observed in the segment (~28.0 nm) of the AuNW.

As a contrast, stack fault was observed within another AuNW shown in Fig. 4.10. The corresponding FFT of AuNW in the red box can be indexed to the [110] zone axis of crystalline AuNW, in which streaky spots were found along the [111] direction (Fig. 4.10(b)), in contrast to that of defect-free AuNW in Fig. 4.9(b). The streaking spots could originate from the stacking faults on {111} planes which interrupt long-range crystalline sequence of the AuNW.[27] The reverse of FFT confirmed the stacking faults on {111} planes existed in the sample, marked as SF in Fig. 4.10(c). It is reasonable to have the defect as stacking fault in the FCC gold nanowires since gold has a relatively low stacking fault energy (ca. 33 mJ m^{-2}).[28]

Furthermore, we inspected the electron diffraction pattern of a larger selected area where two AuNWs displayed the segments of 55 nm and 70 nm, respectively (Fig. 4.11(a)). The indexed spots were {111} and {002} planes perpendicular to <110> zone axis as shown in Fig. 11(b), which indicated the AuNWs had single

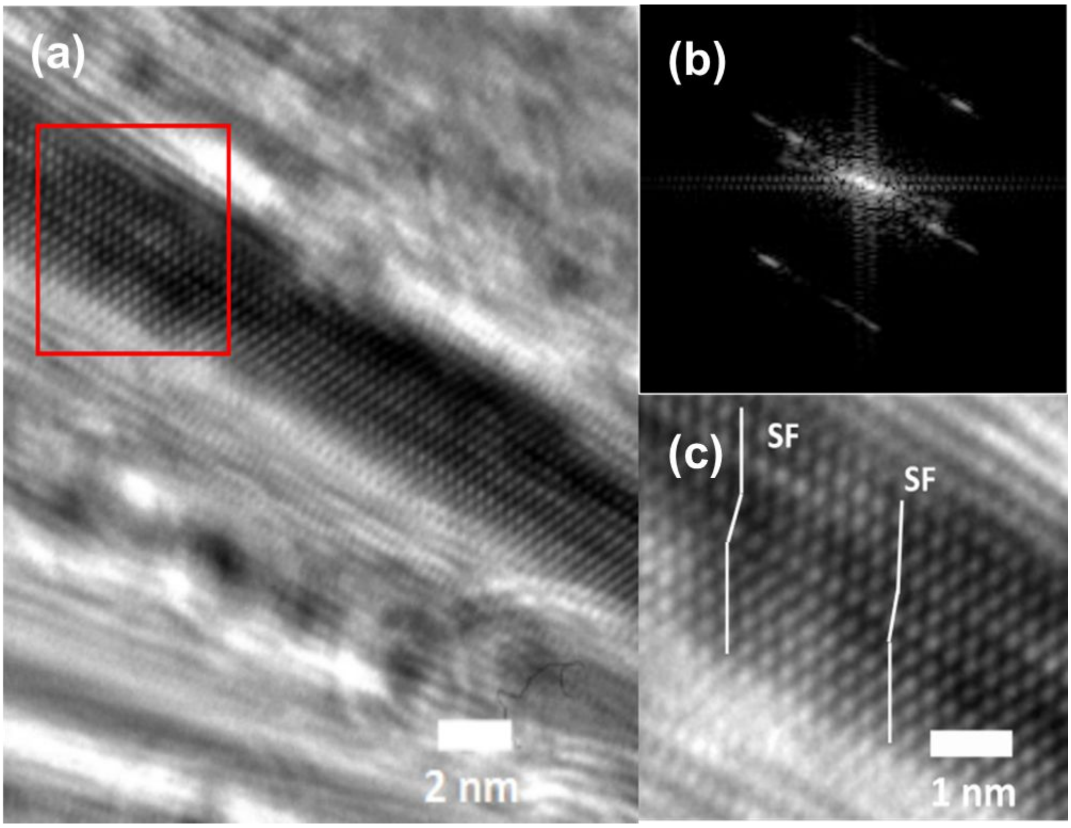

Figure 4.10 Ultrathin AuNW with stacking faults inside CNT (a) its HRTEM image (b) the corresponding FFT of the area in the red box in (a) and (c) reverse FFT of (b) showing stacking faults.

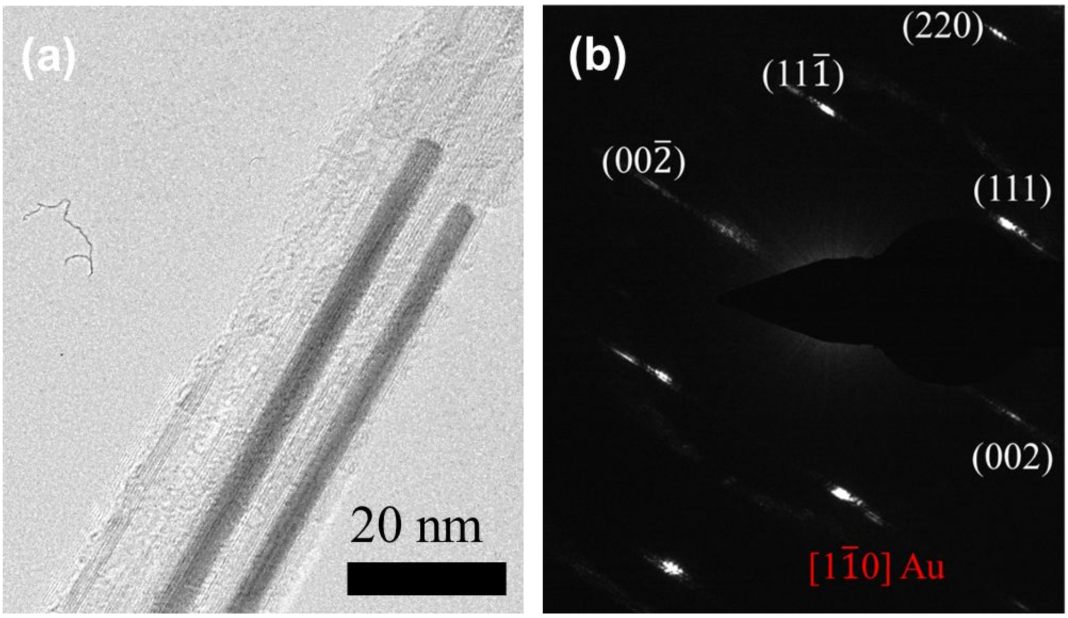

Figure 4.11 (a) TEM image of a selected area with two AuNWs and (b) their diffraction pattern.

crystalline FCC structure with a preferential {111} orientation, consistent with the analysis from HRTEM records and the related FFT results in Figure 4.9 and 4.10. Moreover, streaky spots along <111> were also observed suggesting stacking faults possibly existed in the samples. Since the segments of AuNWs in selected area were long enough (~70 nm), the obtained result from Fig. 4.11, that is single-crystalline FCC structure of AuNWs is more representative. As a matter of fact, we inspected more than 200 AuNWs with HRTEM in this work and identified all of them were single crystalline. A few more representative AuNWs at high magnification are shown in Fig. 4.12 through (a) to (f). Clearly all the AuNWs listed here were single-crystalline. From Fig. 4.12 (a) to (c) were defect-free nanowires whereas stacking faults were frequently detected along with the wires in (d) and (e).

According to the aforementioned discussion, the structure of AuNWs@HTY is schematically shown in Fig. 4.13(b) and (c). For a better comparison, the HRTEM image of a selected ultrathin AuNW was displayed in Fig. 4.13(a). The growth direction of AuNW follows <111> indicating that Au{111} planes arrange periodically along the tube walls with the constant distance 2.35 Å. The schematic diagram of cross-section of AuNW@HTY in Fig. 4.13(c) obviously presents gold atoms forming hexagonal lattice that composes of the typical {111} facets.

To investigate the important factors that dominate the growth of AuNWs into CNTs, we examined the synthesis with controllable experimental conditions. In particular, control HTY instead of plasma treated HTY was used as CNTs template for AuNWs encapsulation with the same gold precursor solution and KBr as the

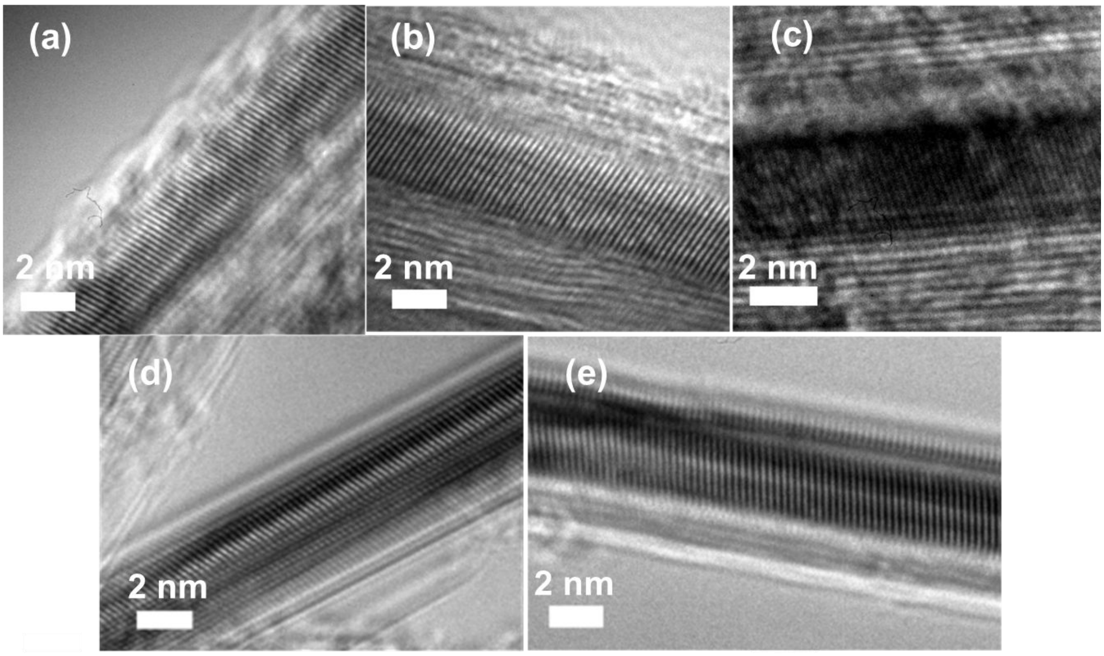

Figure 4.12 HRTEM images of single-crystalline AuNWs from (a) to (f).

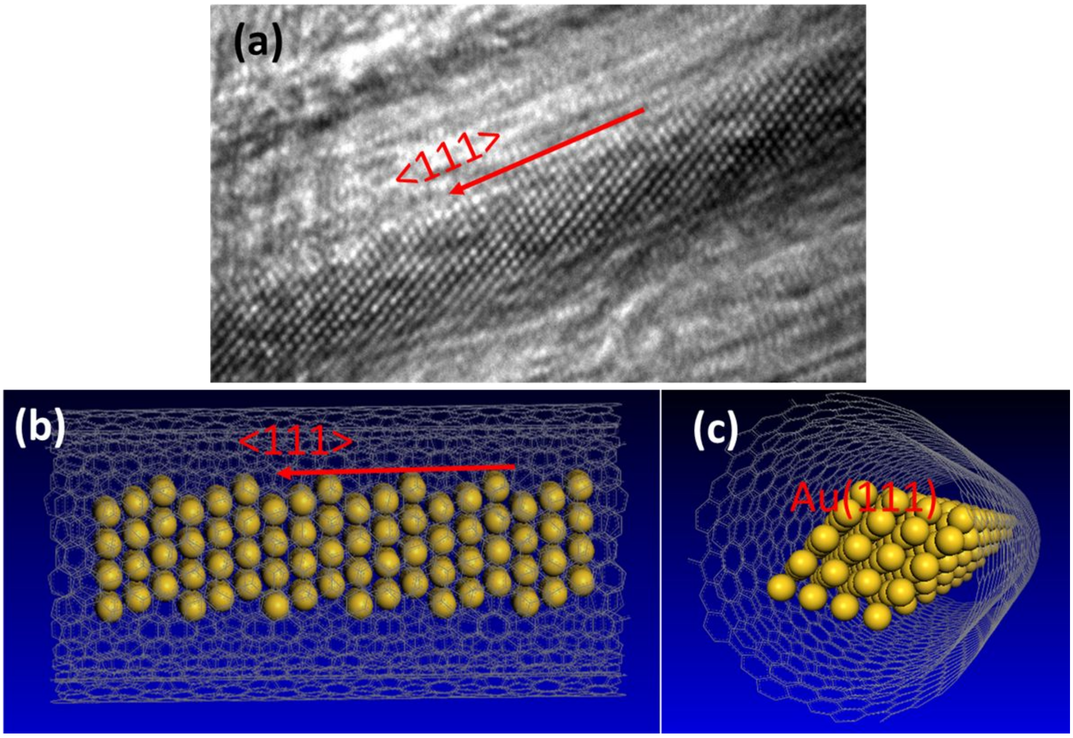

Figure 4.13 (a) HRTEM image of single AuNW inside CNT (b) schematic model of AuNW@CNT according to the heterostructure of (a) and (c) the cross-section area of the model.

surfactant. However, the heterostructure of AuNWs inside CNTs was not observed but as an alternative, plate-like gold nanosheets deposited on the CNTs mesh were synthesized as shown in Fig. 4.14(a). Au nanoplates are supposed to be attributed to the KBr in the solution mixture since bromine ions have been reported to play a key role in promoting anisotropic growth of 2-dimensional gold nanoplates.[29] This result evidently showed that oxygen plasma treatment, even with 40 scans that took less than 60s, effectively introduced structural defects on CNTs shells without which gold atoms could hardly diffuse into the cores. On the other hand, we carried out the experiment that included plasma treated HTY and the same gold precursor yet without KBr in the reaction solution in order to examine the function of Br^-. As a consequence, neither AuNWs inside CNTs nor Au nanoplates on CNTs network were obtained in the sample as shown in Fig. 4.14(b). Nanosized gold particles anchoring on CNTs walls were often observed, which indicated gold crystals nucleated and grew isotropically in the solution free of KBr. We speculate that such isotropic structure of gold nanocrystals was not favorable to diffuse into the graphitic tubes. In other words, KBr, namely, Br^- is of fundamental importance in guiding gold atoms orientate on the preferential planes that are mobile and diffusive within the nanotubes and subsequently form 1-D gold nanowires. To support this speculation, we further inspected more AuNWs@HTY under TEM at high magnification. It is of particular interest to note that gold nanoparticles were occasionally found contact with AuNWs as shown in Fig. 4.15(a). Apparently, Au nanoparticles are immobilized on the outer shells of CNT. A high magnification of TEM image in Fig. 4.15(b) explicitly

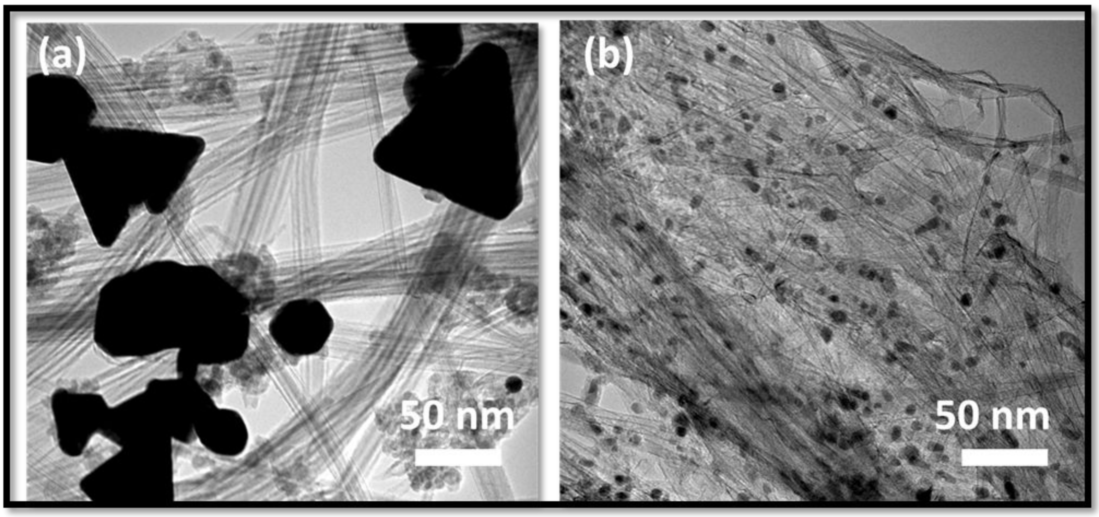

Figure 4.14 Growth factors of AuNWs inside CNT. (a) TEM image of Au nanocrystals obtained with control HTY and (b) TEM image of Au nanocrystals obtained on plasma treated HTY in the solution free of KBr.

identifies the gold nanoparticle fused into the tubes and gradually formed a nanowire. The growth direction was parallel to the alignment direction of CNT walls, as pointed with red arrow which implied the nanowire was encapsulated in the nanotubes and the site where particle and tube connected was the defective place on the graphitc shells for gold atoms entered and diffused.

Since the capability of resolving the atomic level of the junction of particle-wire structure at 80 keV is relatively low, we further utilized 300 keV electron irradiation to investigate the detailed structure evolution of AuNW as shown in Fig. 4.16(a), which strongly supports the gold nanoparticle connected with the wire as an entire configuration in which gold atoms arranged as single-crystalline structure. The detailed structure of connected segment marked as the area in the red box (noted as S1) was shown in Fig. 4.16(b). It is of significant importance to mention that the section owned consistent atoms arrangement, that is, the same crystal orientation, indicative of the Au nanoparticle eventually fusing into AuNW through defective site on graphitic layers. The boundaries of the gold nanocrystal were marked by the white line which clearly demonstrated the fusion steps. Through the last step the gold atoms fully filled up the inner core of the tube (red line indicated as the inner walls of the tube) and the size of the wire became uniform. The measured plane gaps were 2.05 and 2.35 Å, corresponding to dspacing of Au{002} and Au{111} respectively. The FFT of S1 indexed as Au{111} and Au {002} further confirmed the junction was single crystalline and favorably {111} bounded. Exhibited in Fig. 4.16(d) and (e) are the high magnification TEM image of the segment marked in the blue box (noted as

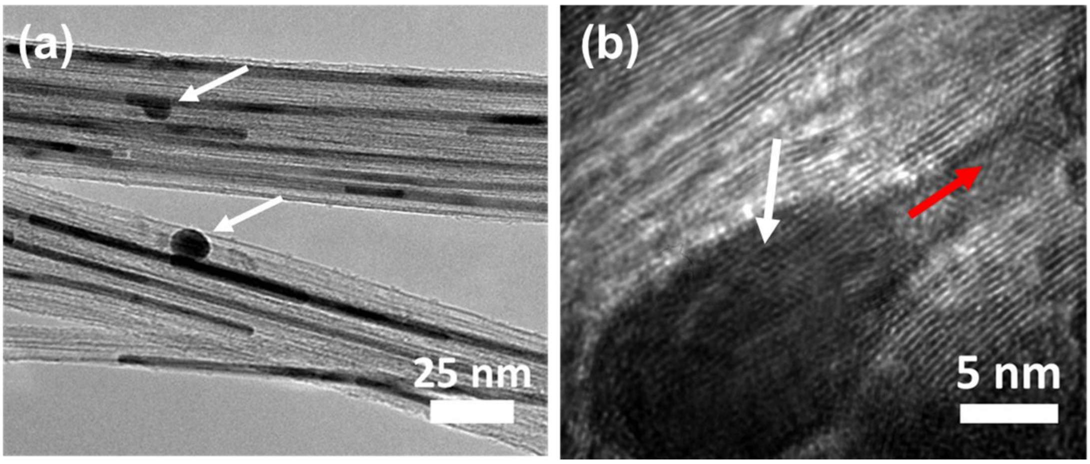

Figure 4.15 Morphologies of gold nanopartices connecting with nanowires. (a) two nanopaortice-nanowire junctions and (b) high magnification image of the junction.

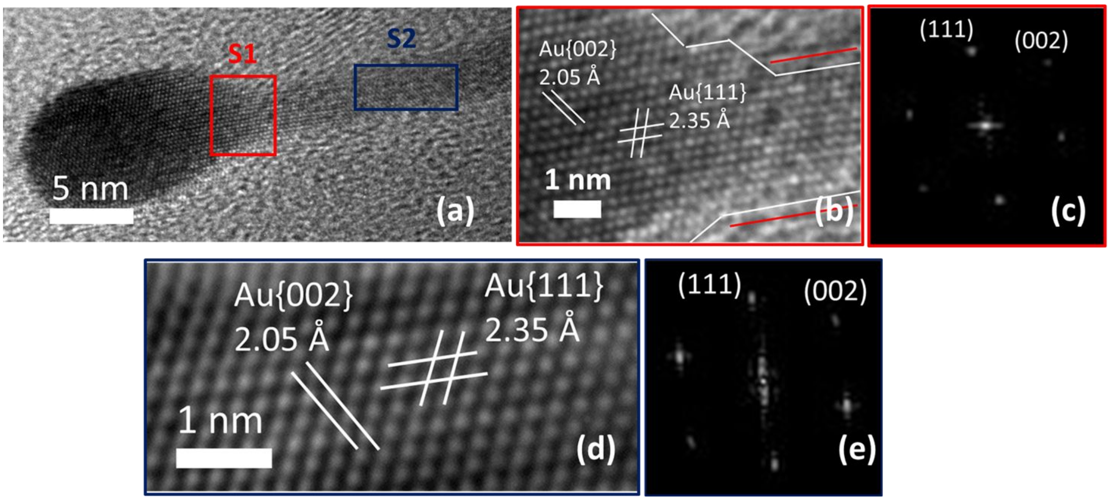

Figure 4.16 Structure of a gold nanoparticle-nanowire junction. (a) HRTEM image of the nanoparticle-nanowire heterostructure (b) a higher magnification image of the junction shown in S1 (red box) (c) the corresponding FFT of S1 (d) a higher magnification image of S2 segment in the blue box of (a) and (e) its corresponding FFT.

S2) in Fig. 4.16(a) and its corresponding FFT. With more than 10 nm gap from the nanoparticle, segment S2 was believed to be fully encapsulated in the tube. Of particular interest was the identical crystalline structure of S2 to S1, in other words, the crystal structure from the particle to S2 preserved consistently and its FFT pattern further supported such consequence since the index was the same as that of S1. Hence, it is reasonable to suggest that AuNWs inside the nanotubes grew from the gold clusters which originally immobilized on the disordered sites of CNTs walls.

Here we suggest it is unlikely that the AuNWs were synthesized by means of liquid phase route, in other words, liquid gold precursor entered the tubes via capillary wetting and then metallic gold was reduced and formed the AuNWs inside the tube. A number of experimental observations support such speculation. First, we examined the samples every one hour yet did not observe any liquid-like materials inside the nanotubes (TEM samples were prepared immediately after HTY was taken out from the solution without any drying). As a matter of fact, water inside CNT is observable with high resolution TEM.[30] Second, if the liquid gold precursor was capable of flowing into the tube, we could expect to obtain AuNWs@HTY in the solution free of KBr, however, the result in Fig. 4.16(b) clearly denied this proposal. Moreover, liquid phase route usually requires post-treatment such as calcination[14] and post reaction at relatively high temperature[31] in order to obtain the desired chemical composition from the filling solution yet we did not employ the high-temperature post-treatment. Finally, the capillarity decreased significantly when the diameter of nanotubes approaches to sub-10 nm which is unlikely to explain the formation of nanowires longer than 1 μm via liquid phase strategy.

According to the observations in Fig. 4.16, we propose a solid diffusion growth mechanism of AuNWs@HTY which is schematically illustrated in Fig. 4.17. Note that the multi-walled CNT in this work was simplified as single-walled CNT in order to make the model more understandable.To begin with, oxygen plasma is used to react with seamless graphitic layer, open up the carbon rings and ultimately create defective sites on the wall. As discussed, the defective sites created via plasma might include functional groups, vacancies, heptagon-petagon pairs, voids, kinks and so forth as illustrated in Fig. 4.17(b-1). The carbon atoms in red locate at the edge of the void emphasize the configuration of the defect. It has been widely reported the defective spots on CNTs shells, such as oxygenated vacancies would be the favorable nucleation sites for gold clusters rather than pure graphene due to the relative low binding energies of gold and clean graphene (ca. 0.66 eV).[32] As a consequence, Au cluster preferentially starts to nucleate from the disordered area and grows to nanoparticle shown in Fig. 4.17(c). Owing to the observation in Fig. 4.16, Au nanoparticle was {111} orientated in which the abundant {111} planes were attributed to Br- ions serving as the capping agent. Free Br- ions from KBr were likely supposed to preferentially bind to Au (111) faces, protect Au (111) facets, and subsequently result in a slower growth along [111] direction when the fresh Au atoms diffuse into the cluster. As a result, plate-like Au sheets could be obtained on the template such as HTY mesh prior to plasma exposure as shown in Fig. 4.14(a), when the growth path was strictly limited to the surfaces of CNT network.

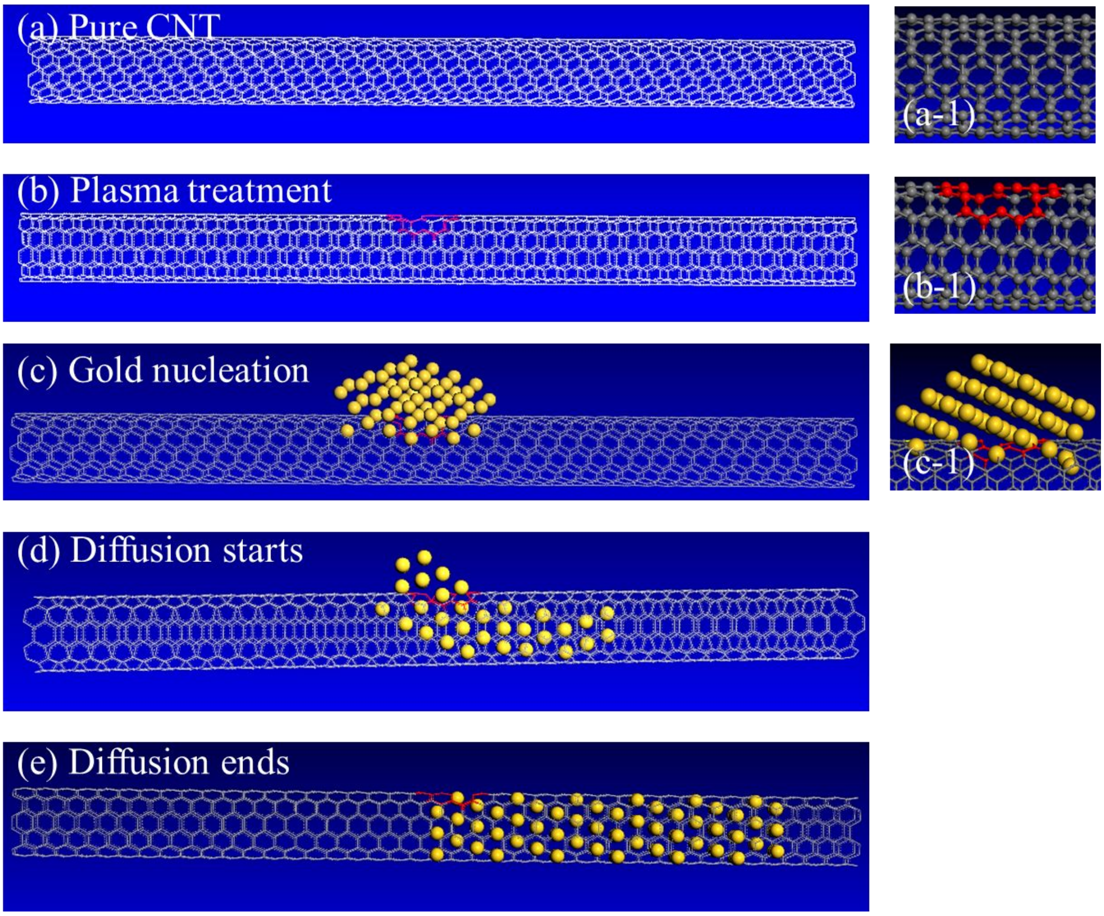

Figure 4.17 Schematic illustration of proposed growth mechanism of AuNWs@HTY.

On the other hand, when the carbon rings are opened, a new route for gold atoms diffusion is immediately built up. It is reported that the diffusivity of gold atoms on graphene surface is rather large even at room temperature due to a low activation energy~0.28 eV.[33] Hence, gold atoms are highly mobile the the clean graphene surface.34 Moreover, due to the stronger π-π overlap of the inner surface (concave) making wetting more difficult, the interaction of the inner shell with gold atoms should be somewhat weaker than at the outer (convex) surface where weaker overlap of the π-orbitals protruding from the convex outer surface of the tubes.[12] The defects within CNTs walls and amorphous carbon on the outer-shell surfaces would additionally enhance the energy barrier for gold atoms to move and grow. As a consequence, gold atoms are supposed to diffuse more easily and rapidly through the inner surfaces rather than outer surfaces as shown in Fig. 4.17(d). New atoms reduced out from the gold precursor stack into the cluster continuously which function as the gold source of the nanowire. Subsequently, The AuNW keeps on growing within the tube and the growth would not stop until the reaction is completely finished or the Au atoms encounter the defects on the inner shell of CNT where the energy barrier is too high to overcome, which are likely two main factors restricting the length of AuNWs inside a nanotube with sufficient length. The ultimate hybrid structure of AuNW@CNT is presented as Fig. 4.17(e). Note that most of the AuNWs@HTY were not associated with Au nanoparticles with the examination of TEM, indicating the growth of AuNWs in this work was overall sufficient.

As depicted in Fig. 4.15(b), Br^- has played a key role in the synthesis of

AuNWs@HTY. Images in Fig. 4.16 further confirmed that the heterostructure of nanoparticle-nanowire was single-crystalline {111} orientated. Therefore, it is rational to suspect that the gold atoms orientated on {111} planes posses a higher possibility to diffuse along the graphitic surfaces than those belong to other planes. That is to say, isotropic Au nanoparticles with randomly orientated facets would be rarely apt to fuse into the hollow cores of the CNTs, which explains the absence of AuNWs in the solution free of KBr. As a matter of fact, all the AuNWs observed in this work were favorably bounded with {111} facets sustaining such kind of aforementioned suspect.

In order to investigate the stability of ultrathin AuNWs@CNT with electron irradiation, we carried out energetic electron bombardment with the accelerating voltage at 300 keV. The screen current was around 7 nA. Shown in Fig. 4.18(a) to (f) is the breaking process of a {111} orientated ultrathin AuNW with electron irradiation. Initially, CNT shells were damaged rapidly with 300 keV voltage and crystalline carbon layers transformed to amorphous carbon as shown in Fig. 4.18(a). On the other hand, single crystalline structures of AuNW was well detected. In Fig. 4.18(b), the wire started to be thinning in the middle part with 30-second irradiation where the white arrows point. The thinning phenomena became more severe along with more time to be exposed to the beam as illustrated from Fig. 4.18(c) to (e). The wire finally broke at the thinnest part at the stage of 325 s, indicating low resistance to the energetic electron attack. The breaking process is similar to a previous report that ultrathin AuNW broke with electron bombardment.[35,36] However, we did not observe any structure rotations and the crystal preserved {111} orientation free of twins from

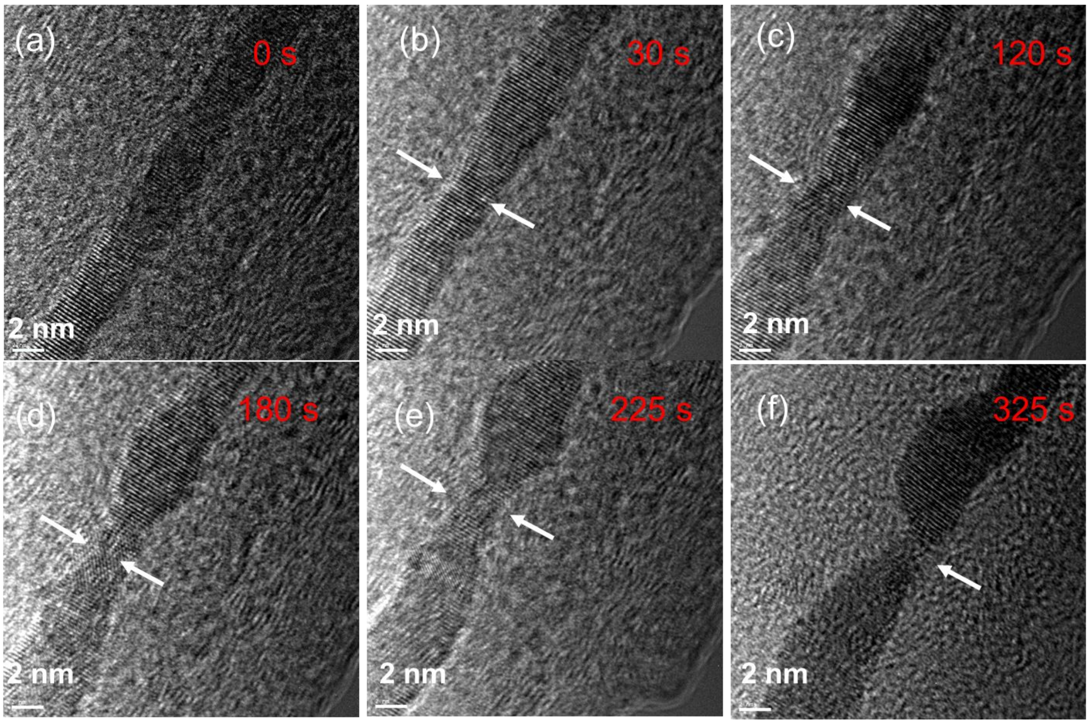

Figure 4.18 Structure failure of an ultrathin AuNW under electron irradiation at 300 keV. (a) to (f) shows the thinning process of the wire along with exposure time.

the beginning till its breakdown.

Shown in Fig. 4.19 is a more interesting phenomena that electron irradiation created angstrom-scaled twins to one wire (denoted W-1) in a short period, i.e. less than 15 s whereas the other wire (denoted W-2) kept defect-free structure (Fig. 4.19(c)). With increasing irradiation time, twins density within W-1 continuously increased so as to accommodate the energy from incident electron beam (from Fig. 4.19 (d-0) to (d-8)). As a consequence, the wire gradually became distorted instead of thinned as shown in Fig. 4.19(d-3). Meanwhile, the structure modification of W-2 was more similar to the one in Fig. 4.18 which nanowire thinning gradually occurred in a certain segment of the wire (Fig. 4.19(d-3)-(d-6)). Moreover, no twins were created in W-2 with the electron beam which was consistent with previous wire mentioned in Fig. 4.18. It is of particular interest to note that defect-free W-2 broke at 345 s whereas W-1 with a large number of twins still survived as shown in Fig. 4.19(d-6). It has been reported that increasing twins density could enhance the ultimate tensile strength of ultrathin AuNWs.[37] Here we show that the twins in ultrathin AuNWs effectively improved the resistance to energetic electron irradiation. W-2 even maintained the structure integrity with more than 1500 s irradiation as presented in Fig. 4.20(b).

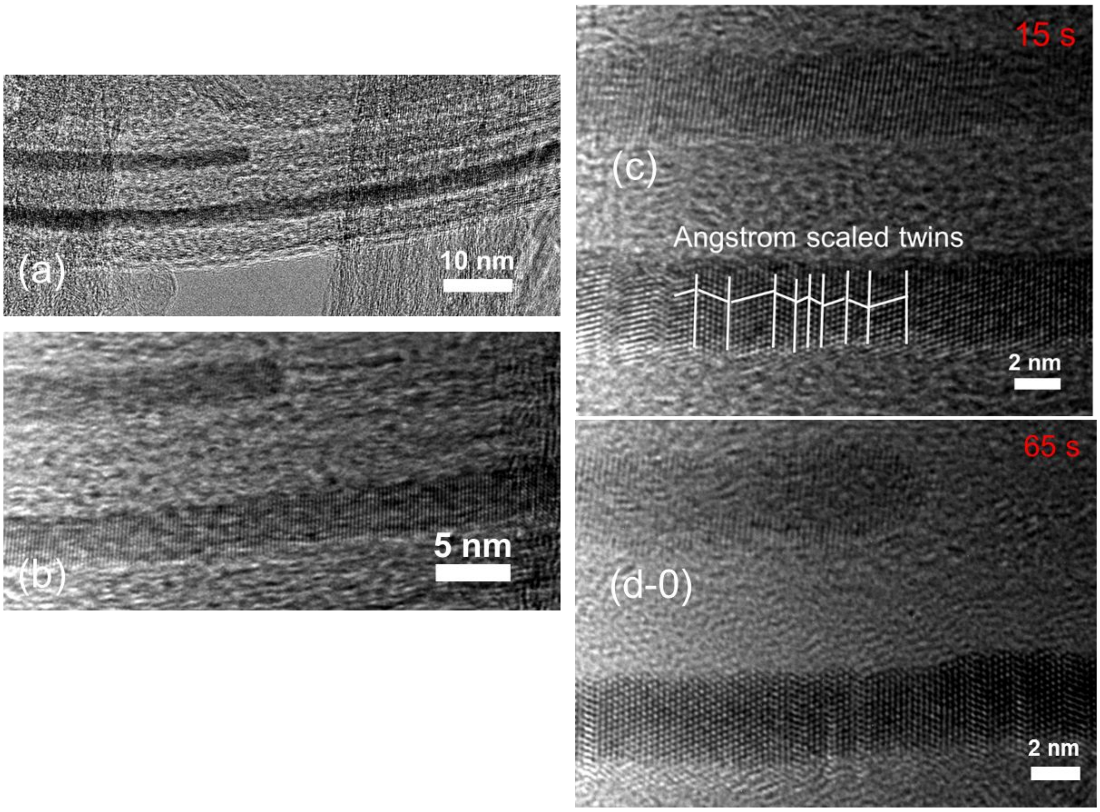

Figure 4.19 Electron irradiation of two ultrathin AuNWs at 300 keV. (a) structure of AuNWs (b) high magnification image to confirm their single crystalline structure (c) electron irradiation resulted in multiple twins to the bottom wire (d-0) further structures transformation along with time.

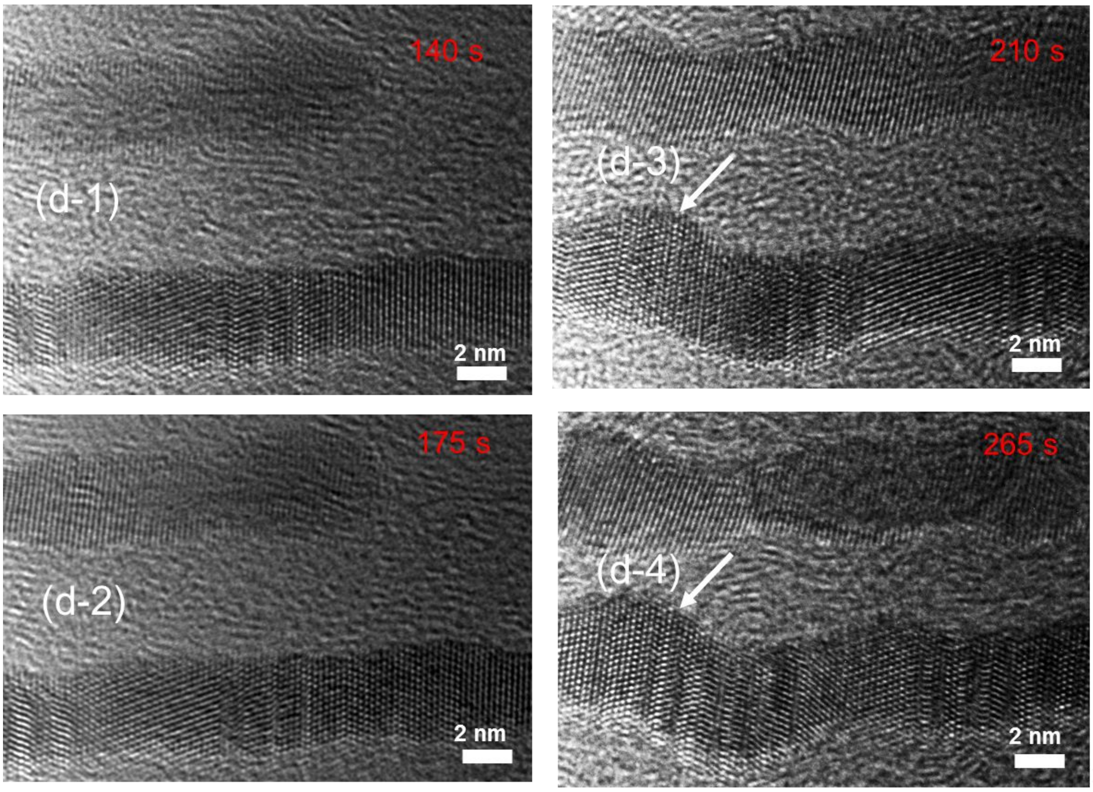

Figure 4.19 (d-0) to (d-4) further structures transformation along with time (140 s to 265 s).

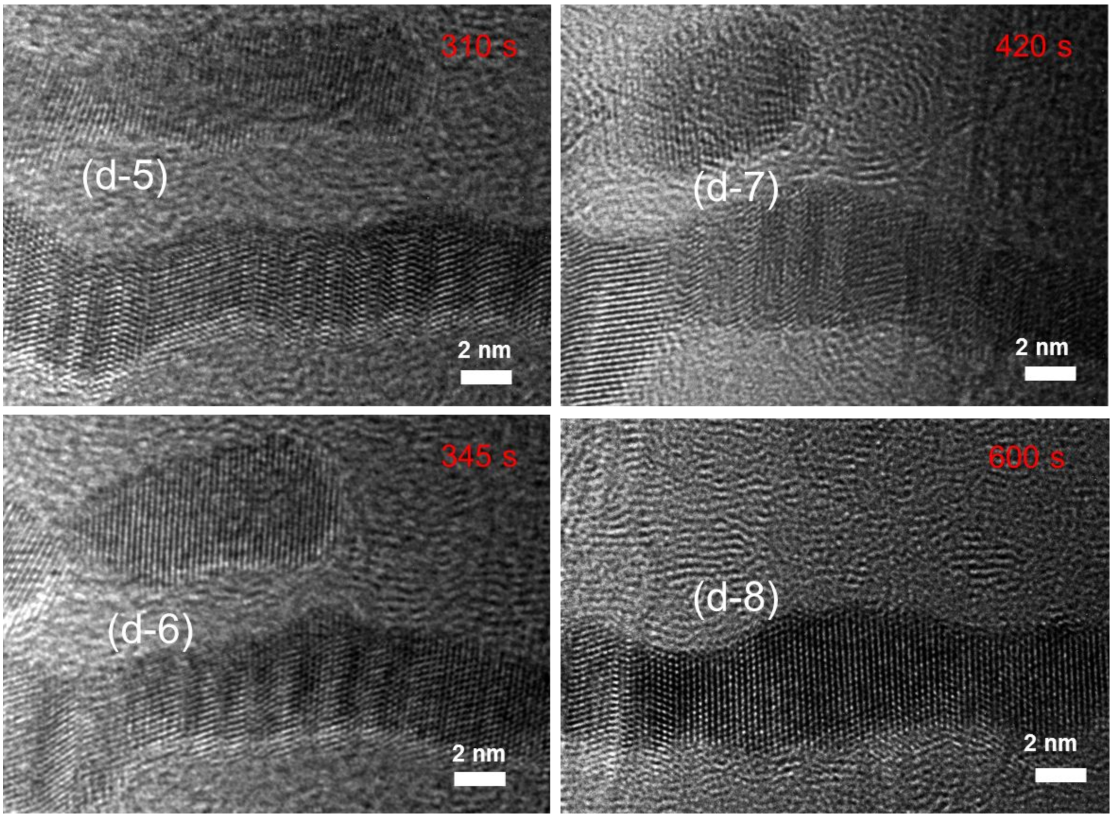

Figure 4.19 (d-5) to (d-8) further structures transformation along with time (310 s to 600 s).

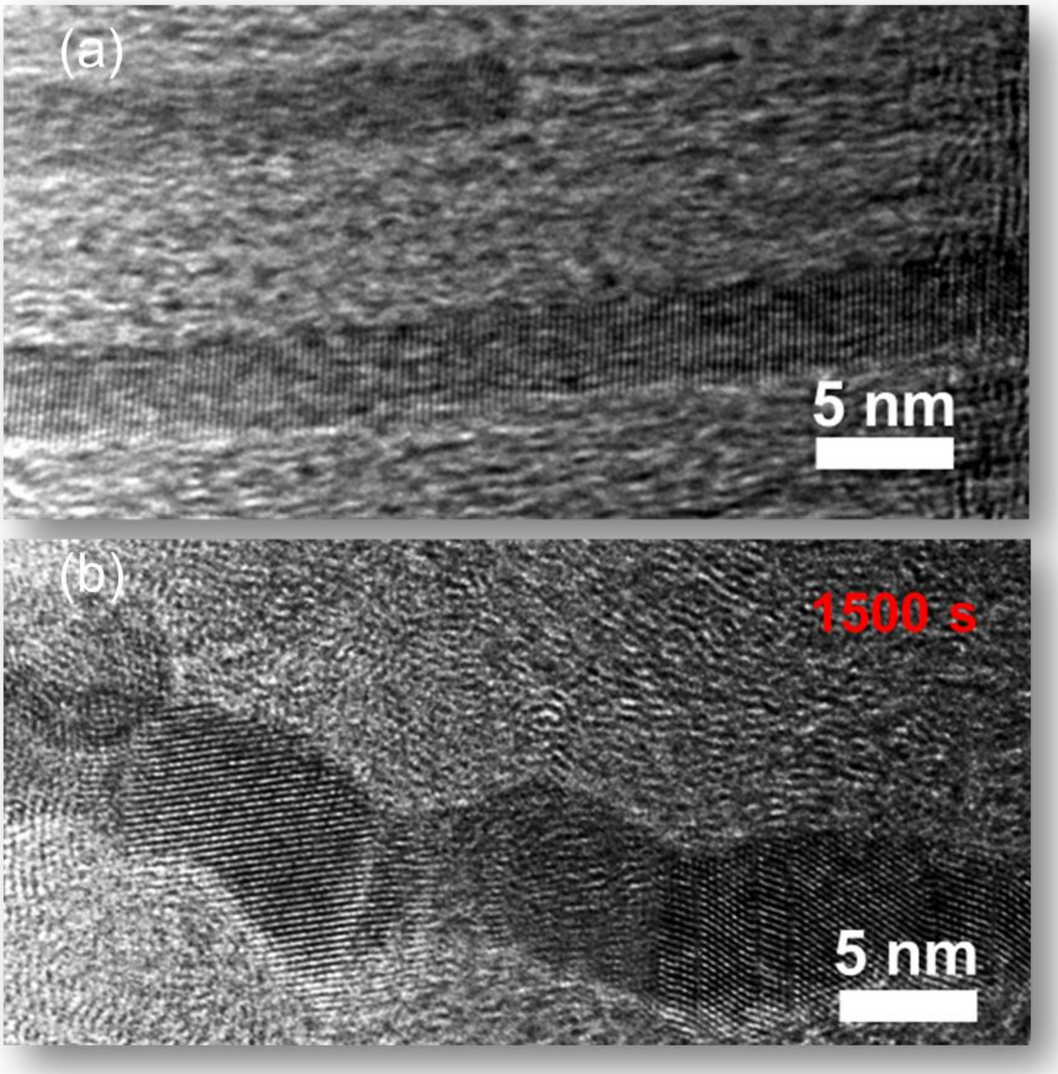

Figure 4.20 Ultrathin AuNWs before (a) and after (b) electron irradiation for 1500 s.

4.4 Conclusions

In this work, we present a novel method for growing ultrathin AuNWs inside CNT including two steps: (1) rapid plasma treatment to open CNT walls and (2) growing AuNWs into CNT cores relying on high mobility of Au atoms in the concave graphene surfaces. The obtained AuNWs had maximum aspect ratio around 500 which is higher than previous reports regarding AuNWs@CNT. The graphitic layer protected ultrathin AuNWs are highly stable under electron irradiation and thus their single crystalline structures with atomic scale stacking faults are well resolved with TEM. This potentially opens up a new route to investigate the fine structures of ultrathin AuNWs at atomic scale. According to the experimental observations, we propose a growth mechanism elucidating plasma treatment and surfactant KBr have played the critical roles in the formation of AuNWs confined inside CNT, which may guide more metal objects grow into CNT at moderate low temperature in future.

4.5 References

1. M. F. L. De Volder, S. H. Tawfick, R. H. Baughman and A. J. Hart, *Science*, 2013, **339**, 535–539

2. R. R. Meyer, J. Sloan, R. E. Dunin-Borkowski, A. I. Kirkland, M. C. Novotny, S. R. Bailey, J. L. Hutchison and M. L. H. Green, *Science*, 2000, **289**, 1324

3. R. Senga, H. P. Komsa, Z. Liu, K. Hirose-Takai, A. V. Krasheninnikov and K. Suenaga, *Nat. Mater.*, 2014, **13**, 1050–1054

4. E. Gaufrès, N. Y. W. Tang, F. Lapointe, J. Cabana, M. A. Nadon, N. Cottenye, F. Raymond, T. Szkopek and R. Martel, *Nat. Photonics*, 2014, **8**, 72–78

5. Q. Liu, R. Zou, Y. Bando, D. Golberg and J. Hu, *Prog. Mater. Sci.,* 2015, **70**, 1−49

6. Y. Gao and Y. Bando, *Nature*, 2002, **415**, 599

7. L. Sun, F. Banhart, A. V. Krasheninnikov, J. A. Rodriguez-Manzo, M. Terrones and P. M. Ajayan, *Science*, 2006, **312**, 1199–1202

8. Y. Chen, Z. Ouyang, M. Gu and W. L. Cheng, *Adv. Mater.*, 2013, **25**, 80–85

9. J. W. Wang, F. Sansoz, J. Y. Huang, Y. Liu, S. H. Sun, Z. Zhang and S. X. Mao, *Nat. Commun.*, 2013, **4**, 1742

10. C. Wang, Y. Hu, C. M. Lieber and S. Sun, *J. Am. Chem. Soc.*, 2008, **130**, 8902–8903

11. S. Gong, W. Schwalb, Y. Wang, Y. Chen, Y. Tang, J. Si, B. Shirinzadeh and W. Cheng, *Nat. Commun.*, 2014, **5**, 3132

12. F. Banhart, *Nanoscale*, 2009, **1**, 201–213

13. S. Arcidiacono, J. H. Walther, D. Poulikakos, D. Passerone and P.

Koumoutsakos, *Phys. Rev. Lett.*, 2005, **94**, 105502

14. A. Govindaraj, B. C. Satishkumar, M. Nath and C. N. R. Rao, *Chem. Mater.*, 2000, **12**, 202–205

15. G. Liao, Y. Pan, Q. Wu, S. Li, Y. Weng, X. Zhang, Z. Yang, J. Guo, M. Chen, M. Tang and O. K. C. Tsui, *Nanoscale*, 2014, **6**, 14872–14876

16. F. Zhang, P. Ren, X. Pan, J. Liu, M. Li and X. Bao, *Chem. Mater.,* 2015, **27**, 1569–1573

17. R. Kitaura, N. Imazu, K. Kobayashi and H. Shinohara, *Nano Lett.*, 2008, **8**, 693–699

18. A. Chu, J. Cook, R. J. R. Heesom, J. L. Hutchison, M. L. H. Green and J. Sloan, *Chem. Mater.*, 1996, **8**, 2751–2754

19. X. Wang, N. Li, L. D. Pfefferle and G. L. Haller, *Microporous Mesoporous Mater.*, 2013, **176**, 139–144

20. H. Yu, D. Cheng, T.S. Williams, J. Severino, I.M. De Rosa, L. Carlson and R.F. Hicks, *Carbon,* 2013, **57**, 11-21

21. V. Datsyuk, M. Kalyva, K. Papagelis, J. Parthenios, D. Tasis, A. Siokou, I. Kallitsis and C. Galiotis, *Carbon*, 2008, **46**, 833–840

22. F. Villalpando-Paez, H. Son, D. Nezich, Y. P. Hsieh, J. Kong, Y. A. Kim, D. Shimamoto, H. Muramatsu, T. Hayashi, M. Endo, M. Terrones and M. S. Dresselhaus, *Nano Lett.*, 2008, **8**, 3879–3886

23. R. A. DiLeo, B. J. Landi and R. P. Raffaelle, *J. Appl. Phys.*, 2007, **101**, 064307–064312

24. C. H. Kiang, M. Endo, P. M. Ajayan, G. Dresselhaus and M. S. Dresselhaus, *Phys. Rev. Lett.*, 1998, **81**, 1869–1872

25. X. Lu, M. S. Yavuz, H.-Y. Tuan, B. A. Korgel and Y. Xia, *J. Am. Chem. Soc.*, 2008, **130**, 8900–8901

26. H. Kura and T. Ogawa, *J. Appl. Phys.*, 2010, **107**, 074310

27. J. Hu, Y. Bando, Z. Liu, J. Zhan, D. Golberg and T. Sekiguchi, *Angew. Chem., Int. Ed.*, 2004, **43**, 63–66

28. A. Halder and N. Ravishankar, *Adv. Mater.*, 2007, **19**, 1854–1858

29. D. V. R. Kumar, A. A. Kulkarni and B. L. V. Prasad, *Colloids Surf., A,* 2013, **422**, 181–190

30. N. Naguib, H. Ye, Y. Gogotsi, A. G. Yazicioglu, C. M. Megaridis and M. Yoshimura, *Nano Lett.*, 2004, **4**, 2237–2243

31. Z. Y. Wang, H. Li, Z. Liu, Z. Shi, J. Lu, K. Suenaga, S. K. Joung, T. Okazaki, Z. N. Gu, J. Zhou, Z. X. Gao, G. P. Li, S. Sanvito, E. Wang and S. Lijima, *J. Am. Chem. Soc.*, 2010, **132**, 13840–13847

32. I. Suarez-Martinez, C. Bittencourt, X. Ke, A. Felten, J. J. Pireaux, J. Ghijsen, W. Drube, G. Van Tendeloo and C. P. Ewels, *Carbon*, 2009, **47**, 1549–1554

33. R. Anton and I. Schneidereit, *Phys. Rev. B.*, 1998, **58**, 13874–13881

34. R. Zan, U. Bangert, Q. Ramasse and K. S. Novoselov, *Nano Lett.*, 2011, **11**, 1087–1092

35. P. Kundu, S. Turner, S. Van Aert, N. Ravishankar and G. Van Tendeloo, *ACS Nano*, 2013, **8**, 599–606

36. L.-M. Lacroix, R. Arenal and G. Viau, *J. Am. Chem. Soc.,* 2014, **136**, 13075−13077

37. J. W. Wang, F. Sansoz, J. Y. Huang, Y. Liu, S. H. Sun, Z. Zhang and S. X. Mao, *Nat. Commun.*, 2013, **4**, 1742

Chapter 5 Conclusions and Future Work

5.1 Conclusions

The goal of this thesis is to develop multi-fuctional carbon nanotube assemblies decorated with gold nanocrystals with various dimensions through novel synthesis routes. It first reviewed structures of CNT/graphene and CNT assemblies as well as dimension tunable Au nanocrystals with a few representative examples of CNT/graphene-Au nanocrystals. Meanwhile, current challenges in the development of multi-functional CNT assemblies with Au nanocrystals was presented. It then illustrated novel synthesis methods for 1-D gold nanowires (AuNWs) inside CNTs and 2-D gold nanoplates (AuNPLs) on both graphene and CNT assemblies substrates. It revealed $KAuBr_4$ serving as the gold precursor played a key role in growing AuNPLs on graphene sheets. Characterization showed that the synthesized AuNPLs with well-defined shapes are single-crystalline FCC structure with highly preferential {111} orientation. The geometry and size of AuNPLs were tunable from which a three-step growth mechanism was proposed. It confirmed Br^- ions could favor the anisotropic growth of AuNPLs on graphene surface.

Based on the novel synthesis of AuNPLs on graphene sheets, a simple route for in-situ synthesis of 2-D AuNPLs on CNT sheets was introduced. A new flexible surface-enhanced Raman scattering (SERS) substrate was constructed based on CNT sheets-AuNPLs hybrid. Accordingly, Rh6G at a very low concentration (10^{-7} M) was identified by using such flexible CNT sheet-AuNPLs platform via SERS strategy, showing huge advantages in contrast to Au nanoparticles decorated CNT sheet. By means of incorporating AuNPLs with commercially available CNT sheet, such novel flexible SERS substrate owns great potential for scale-up fabrication in future.

It further introduced a novel method for filling gold nanowires (AuNWs) inside assemblied CNTs. With oxygen plasma treatment, CNT walls were rapidly opened in 40 seconds. Raman spectroscopy and high resolution TEM confirmed the defects were created on CNT walls. Gold atoms diffused into CNT cores at a moderately low temperature (~80-90 ^{o}C) and graudally formed ultrathin AuNWs. AuNWs showed a maximum aspect ratio (length/diameter) up to 500 higher than previous reports regarding AuNWs inside CNTs. Detailed characterizations identified their single crystalline face-centered cubic (FCC) structure. Experimental results clarified plasma treatment and the surfactant potassium bromide (KBr) played key roles in the formation of AuNWs. Accordingly, a growth mechanism was propored to elucidate the growth procedures of the interesting heterostructure. Finally, ultrathin AuNWs protected by graphitic shells were highly stable under electron irradiation. Ultrathin AuNWs with twins were more resistant to electron irradiation compared to those wires free of defects.

5.2 Future Work

Despite a comprehensive analysis of crystalline structures of AuNPLs was explored in Chapter 2 and Chapter 3 in this thesis, a few questions still remain. For instance, the origin of the forbidden diffraction spots in the gold plates, i.e. 1/3{422} are not completely clear.[1] Although a number of reports suggest the atomically flat surfaces,[2] stacking faults[3] and twins[4] may possibly contribute to the presence of

1/3{422} spots, there is no conclusive evidence to support the speculations. Furthermore, it has been reported the growth of 2-D nanoplates were driven by screw-dislocations yet the atomic structures of screw-dislocation on nanoplates haven't been well investigated.[5,6] Hence the remained obstacles require a further study of nanoplate structures at sub-nanometer scale, which have to utilize more subtle microscope techniques in future.

AuNW encapsulated in CNT cores (AuNW@CNT) exhibits an attractive core-shell heterostructure. Based on CNT assemblies, this work opens up a novel route to fabricate such core-shell hybrid at macroscale. Recently a wide range of core-shell hybrids have been exploited for multiple applications, such as solar cells,[7] supercapacitors,[8] batteries[9] and so forth. It is hence reasonable to believe core-shell of AuNWs@CNT, especially its marco-form, i.e. AuNWs@CNT assemblies could display multi-functional performance. Therefore, one of the major work in future aims to integrate them with true engineering environment and solve urgent problems in human life. On other hand, besides of only growing gold inside CNT, it is expected to introduce more foreign materials into CNT assemblies and thus broaden the usages of the novel composite materials. With a comprehensive understanding of the growth mechanism of AuNW@CNT, it is very likely to confine other metal nanowires inside CNT cores via the same route.

Despite gold doping can effectively enhance the electrical conductivity of CNT yarns/sheets, many limitations currently exist. For instance, metal plating is one of the difficulties in the doping process because it hardly contributes to conductivity enhancement yet increases the weight dramatically to the CNT assemblies.[10] Therefore, it is expected to solve the plating issue after a thorough understanding of the interactions between carbon and gold, which can further the enhancement of electrical conductivity. In addition, another future goal is to make highly conductive CNT yarn as real products, in other words, conductive cables and wires. It is of fundamental importance to investigate the necessities for CNT yarns serving as conductive wires. For instance, it is suggestive to employ a low-density nanoresin dicyclopentadiene (DCPD) to coat the yarns as the insulating layer because preliminary results show that DCPD-coated CNT yarns have the comparable conductivity with bare CNT yarns. Another critical property of conductive wires is fatigue. Thus, design of experiments for fatigue test of the yarns need to be taken into consideration in future.

5.3 References

1. I. Pastoriza-Santos and L. M. Liz-Marzan, *J. Mater. Chem.*, 2008, **18**, 1724–1737
2. R. Jin, Y. W. Cao, C. A. Mirkin, K. L. Kelly, G. C. Schatz and J. G. Zheng, *Science*, 2001, **294**, 1901–1903
3. V. Germain, J. Li, D. Ingert, Z. L. Wang and M. P. Pileni, *J. Phys. Chem. B*, 2003, **107**, 8717–8720
4. C. Lofton and W. Sigmund, *Adv. Funct. Mater.*, 2005, **15**, 1197–1208
5. S. A. Morin, A. Forticaux, M. J. Bierman and S. Jin, *Nano Lett.*, 2011, **11**, 4449–4455
6. A. Forticaux, L. Dang, H. Liang and S. Jin, *Nano Lett.*, 2015, **15**, 3403–3409
7. Z. Pan, H. Zhang, K. Cheng, Y. Hou, J. Hua and X. Zhong, *ACS Nano*, 2012, **6**, 3982–3991
8. Q. T. Qu, Y. S. Zhu, X. W. Gao and Y. P. Wu, *Adv. Energy Mater.*, 2012, **2**, 950–955
9. W. Zhou, X. Xiao, M. Cai and L. Yang, Nano Lett., 2014, 14, 5250–5256
10. P. Jarosz, C. Schauerman, J. Alvarenga, B. Moses, T. Mastrangelo, R. Raffaelle, R. Ridgley and B. Landi, Nanoscale, 2011, 3, 4542-4553